ΠΑΝΕΠΙΣΤΗΜΙΟ ΚΡΗΤΗΣ

ΤΜΗΜΑ ΧΗΜΕΙΑΣ

ΜΕΤΑΠΤΥΧΙΑΚΟ ΠΡΟΓΡΑΜΜΑ ΕΦΗΡΜΟΣΜΕΝΗΣ

ΜΟΡΙΑΚΗΣ ΦΑΣΜΑΤΟΣΚΟΠΙΑΣ

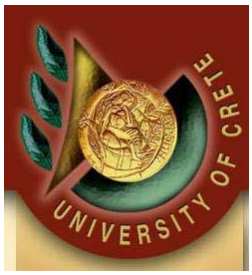

Πολυμερικά Υλικά που Αποκρίνονται στο pH: Επίδραση του Βαθμού Ιοντισμού και Σύνθεση Νανοκρυστάλλων Πλατίνας.

Δάφνη Παλιούρα

Ι.Τ.Ε. – ΙΝΣΤΙΤΟΥΤΟ ΗΛΕΚΤΡΟΝΙΚΗΣ ΔΟΜΗΣ ΚΑΙ ΛΕΪΖΕΡ

ΗΡΑΚΛΕΙΟ, ΔΕΚΕΜΒΡΙΟΣ 2005

UNIVERSITY OF CRETE

CHEMISTRY DEPARTMENT

POSTGRADUATE PROGRAM ON APPLIED MOLECULAR SPECTROSCOPY

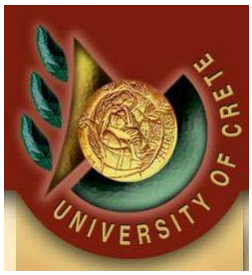

pH-Sensitive Polymeric Materials: Solution Behavior as a function of the Degree of Ionization and Synthesis of Platinum Nanocrystals.

Dafni Palioura

FOUNDATION FOR RESEARCH AND TECHNOLOGY-HELLAS

INSTITUTE OF ELECTRONIC STRUCTURE AND LASER

HERAKLION, DECEMBER 2005

Περίληψη

Σκοπός της εργασίας αυτής είναι η διερεύνηση των ιδιοτήτων αποκρίσιμων στο pH πολυμερικών υλικών μέσα σε υδατικά διαλύματα. Μελετήθηκε, επίσης, ο σχηματισμός κολλοειδών μεταλλικών νανοσωματιδίων μέσα σε τέτοιες πολυμερικές μήτρες και πιο συγκεκριμένα εξετάστηκε η συμπεριφορά του πολυμερούς κατά τη μεταλλίωση καθώς και τα χαρακτηριστικά των μεταλλικών νανοσωματιδίων.

Τα διυδρόφιλα δισυσταδικά συμπολυμερή του μεθακρυλικού εστέρα της εξα(αιθυλενογλυκόλης) με τον 2-(διαιθυλαμινο)αιθυλο μεθακρυλικό εστέρα (DEAEMA) μεταβάλλουν την κατάστασή τους σε υδατικά μέσα ως συνάρτηση της μεταβολής του pH του διαλύματος. Έτσι, σε χαμηλό pH το συμπολυμερές βρίσκεται στο διάλυμα με τη μορφή μεμονωμένων αλυσίδων λόγω της υδροφιλικότητας των πρωτονιομένων μονάδων DEAEMA, ενώ αύξηση του pH του διαλύματος σε τιμές μεγαλύτερες του 7 οδηγεί στην αποπρωτονίωση της συστάδας του PDEAEMA, η οποία γίνεται υδρόφοβη, με συνέπεια τον σχηματισμό μικυλλίων. Οι τεχνικές της δυναμικής σκέδασης του φωτός και της φασματοσκοπία ^{1}H NMR χρησιμοποιήθηκαν για τη μελέτη της μικυλλίωσης ως συνάρτηση του βαθμού πρωτονίωσης (α) της συστάδας του PDEAEMA σε υδατικά διαλύματα των συμπολυμερών. Βρέθηκε ότι για $0.2 < \alpha < 1$ το πολυμερές βρίσκεται στο διάλυμα με τη μορφή ελεύθερων αλυσίδων, ενώ μικύλλια σχηματίζονται μόνο για $\alpha < 0.2$. Η σταδιακή αποπρωτονίωση των μονάδων DEAEMA παρατηρήθηκε επίσης στα φάσματα ^{1}H NMR των συμπολυμερών ως μια σταδιακή μετατόπιση των κορυφών του DEAEMA σε υψηλότερα πεδία λόγω της καλύτερης προστασίας των πυρήνων από το ελεύθερο ζεύγος ηλεκτρονίων του αποπρωτονιωμένου αζώτου. Τέλος, ο σχηματισμός των μικυλλίων οδηγεί στην εξαφάνιση των κορυφών αυτών αφού η συστάδα DEAEMA σχηματίζει τον πυρήνα των μικυλλίων.

Στον πυρήνα των παραπάνω μικυλλίων είναι δυνατόν να διαλυθούν μεταλλικές ουσίες μέσω σχηματισμού συμπλόκων. Ο πυρήνας των μικυλλίων μπορεί να θεωρηθεί ως ένας νανοαντιδραστήρας όπου μπορούν να αναπτυχθούν μεταλλικά νανοσωματίδια ύστερα από αναγωγή του μετάλλου. Η συμπεριφορά του πολυμερούς μετά την εισαγωγή και την αναγωγή του μετάλλου μελετήθηκε με δυναμική σκέδαση του φωτός και φασματοσκοπία ^{1}H NMR. Μετά την προσθήκη H_2PtCl_6 ή K_2PtCl_6 παρατηρήθηκε μικυλλίωση των PHEGMA-*b*-PDEAEMA δισυσταδικών συμπολυμερών σε τιμές του pH μικρότερες του 7 λόγω των ηλεκτροστατικών

αλληλεπιδράσεων μεταξύ των δισθενών $PtCl_6^{2-}$ ανιόντων και των θετικά φορτισμένων αμινοομάδων. Σε υψηλό pH δεν παρατηρήθηκε κάποια μικυλλίωση λόγω της παρουσίας του μετάλλου. Η διαδικασία της μεταλλίωσης μελετήθηκε επίσης με φασματοσκοπία UV/Vis ενώ η ηλεκτρονική μικροσκοπία διέλευσης χρησιμοποιήθηκε για να μελετήσουμε τα μεταλλιωμένα μικύλλια και τα χαρακτηριστικά των νανοσωματιδίων που σχηματίστικαν μετά την αναγωγή του μετάλλου. Τέλος, η κρυσταλλική δομή των νανοσωματιδίων πλατίνας επιβεβαιώθηκε με περίθλαση ακτίνων-Χ, απ' όπου έγινε και μία εκτίμηση του μεγέθους τους γύρω στα 3.5 nm.

Μια άλλη κατηγορία έξυπνων υλικών τα οποία έχουν προσελκύσει ιδιαίτερο ενδιαφέρον τα τελευταία χρόνια είναι τα αποκρίσιμα μικροπηκτώματα. Στην παρούσα εργασία μελετήθηκαν μικροπηκτώματα τα οποία παρασκευάστηκαν με σύνθεση γαλακτώματος συμπολυμερισμού του αποκρίσιμου στο pH (διαιθυλαμινο)αιθυλικού μεθακρυλικού εστέρα χρησιμοποιώντας ως διασταυρωτή PPO. Τα μικροπηκτώματα αυτά σε χαμηλό pH διογκώνονται λόγω της υδροφιλικότητας των πρωτονιωμένων αμινοομάδων, ενώ αυξάνοντας το pH του διαλύματος σχηματίζονται υδρόφοβα σωματίδια τα οποία περιέχουν τις υδρόφοβες μονάδες DEAEMA. Στην παρούσα εργασία μελετήθηκε η συμπεριφορά των μικροπηκτωμάτων αυτών μέσα σε υδατικά διαλύματα ως συνάρτηση του pH του διαλύματος με δυναμική σκέδαση φωτός. Για τιμές του pH μεγαλύτερες του 7 η ακτίνα των υδρόφοβων σωματιδίων βρέθηκε ότι είναι 111 nm, ενώ μειώνοντας το pH του διαλύματος κάτω από 7 η υδροδυναμική ακτίνα αυξάνεται στα 180 nm περίπου.

Νανοσωματίδια πλατίνας σχηματίστηκαν μέσα σε αυτά τα μικροπηκτώματα ύστερα από προσθήκη H_2PtCl_6 και αναγωγή του μετάλλου με $NaBH_4$. Όμοια με την μεταλλίωση των δισυσταδικών συμπολυμερών, η συμπεριφορά των μικροπηκτωμάτων μετά την προσθήκη του μετάλλου καθώς και μετά την αναγωγή του μελετήθηκε με δυναμική σκέδαση φωτός, ενώ χρησιμοποιήθηκε επίσης η φασματοσκοπία UV/Vis για να μελετηθούν οι αλληλεπιδράσεις πολυμερούς-μετάλλου. Τα μεταλλιωμένα μικροπηκτώματα καθώς και τα χαρακτηριστικά των μεταλλικών νανοσωματιδίων μελετήθηκαν με TEM, ενώ η κρυσταλλική δομή των νανοσωματιδίων επιβεβαιώθηκε με περίθλαση ακτίνων-Χ, απ' όπου υπολογίστηκε και το μέγεθός τους γύρω στα 4.5 nm.

Λέξεις κλειδιά : αμινοομάδες, μικύλλια, pH, βαθμός πρωτονίωσης, H_2PtCl_6, K_2PtCl_6, ηλεκτροστατικές αλληλεπιδράσεις, $NaBH_4$, αναγωγή, νανοσωματίδια πλατίνας, αποκρίσιμα μικροπηκτώματα.

Abstract

The aim of the present study is to investigate the solution properties of pH-responsive polymeric materials in water. The formation of colloidal metal nanoparticles within such polymeric matrices is also studied and in particular the polymer behavior upon metallation and the metal nanoparticle characteristics are examined.

Double-hydrophilic block copolymers of poly(hexa(ethylene glycol) methacrylate) (PHEGMA) and poly(2-diethylamino)ethyl methacrylate) (PDEAEMA) alter their characteristics in aqueous media as a function of the solution pH. At low pH the copolymer is in its unimer state due to the hydrophilicity of the protonated DEAEMA units, while an increase of the solution pH above 7 results in the deprotonation of the amine groups, which become hydrophobic and lead to the formation of micelles. Dynamic light scattering and ^{1}H NMR spectroscopy were used to study the micellization process in aqueous solutions of the above copolymers as a function of the degree of protonation (α) of the DEAEMA units. It was found that for $0.2 \leq \alpha \leq 1$ the polymer is in its unimer state while micelles are formed only for $\alpha < 0.2$. The gradual deprotonation of the DEAEMA units was also observed in the ^{1}H NMR spectra of the copolymers as a progressive shift of the DEAEMA peaks to higher fields due to the more effective shielding of the protons from the electron pair of the deprotonated nitrogen. Finally, the formation of micelles leads to the disappearance of the peaks due to the DEAEMA block which becomes non-hydrated and forms the core of the micelles.

The core of these micelles is able to dissolve metal compounds due to coordination with the amine units. Such a micellar core can be considered as a nanoreactor, where nucleation and growth of metal nanoparticles upon metal reduction with $NaBH_4$ are restricted to mesoscale level. The polymer behavior after metal incorporation and reduction was studied by dynamic light scattering and ^{1}H NMR spectroscopy. Upon addition of H_2PtCl_6 or K_2PtCl_6 metal-induced micellization of the PHEGMA-*b*-PDEAEMA diblock copolymers at pH values below 7 was found due to the electrostatic interactions between the $PtCl_6^{2-}$ divalent anions and the positively charged amine groups. At high pH metal-induced micellization was not

observed. The metallation process was also followed by UV/Vis spectroscopy while TEM was used to study the metallated micelles and the characteristics of the nanoparticles formed after metal reduction. Finally, the crystalline structure of the platinum nanoparticles was confirmed by X- Ray diffraction which also allowed to estimate the size of the nanoparticles around 3.5 nm.

Another class of smart materials which have also attracted great attention in recent years is that of stimuli- responsive microgel particles. In the present work acid-swellable microgels synthesized by emulsion copolymerization of the pH-sensitive 2-(diethylamino)ethyl methacrylate monomer with a bifunctional PPO-based cross-linker have been studied. These microgels exhibit reversible swelling properties in water by adjusting the solution pH. Thus, at low pH the microgel particles are swollen due to the hydrophilicity of the protonated amine units, while an increase of the solution pH leads to the formation of hydrophobic latex particles comprising hydrophobic DEAEMA units. The aqueous solution behaviour of the microgel particles was investigated as a function of solution pH by dynamic light scattering. At pH above 7 a radius of 111 nm was obtained for the latex particles while upon decreasing the solution pH below 7 the hydrodynamic size of the microgels increases to ~180 nm.

Platinum nanoparticles were formed within these nano-objects upon addition of H_2PtCl_6 followed by metal reduction with $NaBH_4$. Similar to the metallation of the diblock copolymers, the microgel properties upon incorporation of the metal precursor (H_2PtCl_6) and the subsequent metal reduction was studied by dynamic light scattering, while UV/Vis spectroscopy was used to investigate the polymer-metal interactions. The metallated microgel particles and the metal nanoparticle characteristics were studied by TEM. X- Ray diffraction was also used to verify the crystalline structure of the nanoparticles from which the size of the nanoparticles was estimated to be 4.5 nm.

Keywords: amine groups, micelles, pH, degree of protonation, H_2PtCl_6, K_2PtCl_6, metal-induced micellization, $NaBH_4$, reduction, platinum nanoparticles, responsive microgel particles, latex particles.

Contents

Chapter 1

1.1 Introduction

1.1.1 Responsive materials

Responsive materials are of fundamental importance in many scientific areas due to their great variety of applications in drug delivery [1], biotechnology [2], sensors [3] etc. Responsive or 'smart' polymers are polymers which are able to undergo spectacular changes in their physicochemical properties in response to applied stimuli. 'Smart' polymers are investigated due to both their external, e.g. temperature [4-7], UV [7] or visible light and magnetic field, or internal response, such as pH [8-12] or ionic strength [7, 13].

A characteristic property of 'smart' polymers is their self-assembly [14], a process in which molecules or parts of them form spontaneously ordered aggregates, with no human intervention involved. Biological systems as well as a variety of inorganic physical systems exhibit self assembling. For example, cells contain a great range of complex structures such as lipid membranes, protein aggregates, folded proteins and molecular machines that are formed by self assembly. Also, self assembly provides routes to a range of materials with regular structures, like molecular crystals, liquid crystals and phase-separated polymers. For these reasons, scientists from numerous disciplines, chemistry, physics, biology, and engineering, have begun to investigate the self-assembly process in hope of learning to design and control the behavior of self assembling systems. Much of this work is motivated by recent advances in micro- and nanoscale science and the development of advanced analytical tools.

1.1.2 Micellization

Self-assembly offers one of the most general strategies for generating ordered nanostructures, such as micelles [15]. Micelles are formed in dilute solution in solvents that are selective for one of the blocks of the copolymer. The micellar structure consists of a dense core and a protective corona. The core is formed by the insoluble blocks, while the solvent-soluble blocks form the corona, a shell that extend in solution and confers stabilization to the micelle structure.

In recent years, great attention has been focused in the area of aqueous block copolymer micellar systems [4, 9, 11, 16, 17] due to their great potential as environmental friendly and biocompatible substitutes to micelles formed in organic media. The former micelles are formed by block copolymers comprising one hydrophilic, water-soluble part and a second hydrophobic part that dislikes water. By changing the molecular characteristics (size or architecture of the two parts) various shapes have been observed in water, which range from spherical micelles [8, 10, 11] to vesicles [18, 19], tubules [19] and complex superaggregates [19]. The use of micellar systems in a number of applications such as targeted drug delivery and catalysis has been discussed [1, 20].

Two main types of block copolymers are used for micelle formation in aqueous media: amphiphilic [10] and double-hydrophilic [21] block copolymers.

Amphiphilic block copolymers typically compose of a permanently hydrophobic, water insoluble block that associates in aqueous solution and a hydrophilic block that prevents the aggregates from precipitation. Typical examples of amphiphilic diblock copolymers are polystyrene-*b*-poly(ethylene oxide) (PS-*b*-PEO) [22], polystyrene-*b*-poly(methacrylic acid) (PS-*b*-PMAA) [23], as well as amino-methacrylate based block copolymers [24, 25].

However, the direct dissolution of amphiphilic block copolymers in water has been proved problematic and usually requires the temporary use of an organic cosolvent, such as methanol, dimethylformamide, or tetrahydrofuran, for the preparation of stable and well-defined micelles. The organic solvent plays the role of plasticizer for the hydrophobic core, and increases the unimer/micelle exchange rate which results in the formation of equilibrium micelles. Next, the organic solvent is removed by dialysis. The micelles formed in such copolymer systems are kinetically

frozen, especially if the glass-transition temperature of the core-forming blocks is above ambient temperature [10, 11].

One way to avoid the use of cosolvents in micelle formation is to employ the so-called double hydrophilic block copolymers. These copolymers comprise two different hydrophilic blocks, one of which undergoes physical or chemical transformations in aqueous solution and becomes hydrophobic, while the other remains soluble in water. Thus, micelles are formed in these systems by a simple change in the solution conditions, i.e. pH, temperature and salt concentration [4, 8, 10, 11, 16, 21, 26]. The main advantage of these copolymers is that micellization is a fully-reversible process (**Figure 1.1**). A few examples of double-hydrophilic block copolymers that can form micelles in aqueous media are poly(2-vinyl-pyridine)-*b*-poly(ethylene oxide) (P2VP-*b*-PEO) [16], poly(ethylene oxide)-*b*-poly(2-dimethylamino)ethyl methacrylate (PEO-*b*-PDMAEMA), poly(ethylene oxide)-*b*-poly(2-diethylamino)ethyl methacrylate) (PEO-*b*-PDEAEMA) and PDMAEMA-*b*-PDEAEMA diblock copolymers [4, 5, 9].

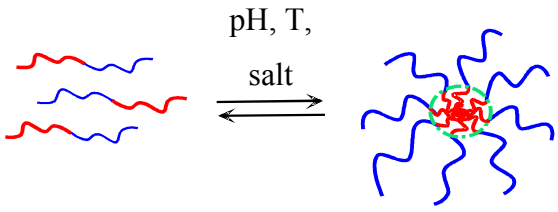

Figure 1.1 Schematic representation of the fully-reversible micellization process.

1.1.3 pH-induced micellization

Increasing attention is paid nowadays to the micellization induced by changing the pH of the aqueous solution of a double-hydrophilic diblock copolymer. Such copolymers comprise a pH-sensitive block which undergoes a transition from hydrophilic to hydrophobic as the solution pH is changed, and forms the micelle core, while the second block is hydrophilic and forms the corona of the micelle. For instance, P2VP-*b*-PEO diblock copolymers form unimers at low pH values and micelles at pH values higher than 5.0 as PVP is protonated and soluble in aqueous solutions at low pH while it becomes deprotonated and insoluble at pH values higher

than 5 [16]. Recently, the self-complexation of PEO-*b*-PMAA was studied [27]. In water of acidic pH, complexes of PMAA and PEO are formed. These complexes are broken by neutralization of PMAA or by addition of alcohols, which disrupt the hydrogen bonds and modify the hydrophobicity of the complexes. As hydrophobic stabilization accounts, in part, for the complexation, an increase in solution temperature tends to enhance the stability of the complexes. The synthesis of PEO-*b*-PDEAEMA has been reported by Vamvakaki et al [4]. ^{1}H NMR spectroscopy studies were carried out at pH 2 and 9 which indicated molecular dissolution at low pH (in DCl/D_2O), when the PDEAEMA block was fully protonated and behaved as a cationic polyelectrolyte. However, at pH 9 (in NaOD/D_2O) the DEAEMA residues were deprotonated and became hydrophobic. Complete disappearance of the DEA-assigned NMR signals indicated formation of fully dehydrated micelle cores. Such pH-sensitive diblock copolymers can be used as pH sensors as a result of their switching from nonassociated chains into micelles [10]. They could also serve as model delivery systems, in which the solute is encapsulated in the micelle cores under certain pH values and is released as the micelles break apart when reaching the target pH.

pH-induced micellization has also been reported for block copolymers comprising two ionizable blocks. Butun et al. reported the first example of a PDEAEMA-based water-soluble diblock copolymer that was capable of forming both conventional micelles and reverse micelles in aqueous solution [28]. This diblock copolymer was based on two tertiary amine methacrylates, DEAEMA and 2-(*N*-morpholino)ethyl methacrylate (MEMA) [29] . The PDEAEMA block is pH-responsive while the MEMA block is salt-sensitive; appropriate selection of the solution pH and the electrolyte concentration allowed the formation of DEAEMA-core micelles and MEMA-core micelles respectively at 20 °C [30]. Recently Bütün et al. [31] reported the synthesis of PDMAEMA-*b*-PDEAEMA diblock copolymers. These copolymers could be molecularly dissolved without any co-solvents in acidic water, while PDEAEMA-based micelle cores were reversibly formed on careful adjustment of the solution pH. Under these conditions the hydrophilic PDMAEMA block formed the micelle corona and the micelles were only stable over a relatively narrow pH range (pH 7.5-9).

The associating behaviour of a more complex system a PDMAEMA-*b*-PMAA ampholytic diblock copolymer has been also studied in water as a function of solution pH [17]. Depending of the pH of the aqueous solution, the DMAEMA units can be positively charged and the MAA units neutral (low pH), the MAA units can be negatively charged and the DMAEMA units neutral (high pH), while for a certain pH range the two blocks can be both charged, thus leading to a polyampholytic copolymer. At the isoelectric point, there are as many positive charges as negative charges. It was found that at pH below the isoelectric point, micelles consisting of a noncharged PMAA block surrounded by a positively charged PDMAEMA corona are formed. As the pH is increased, part of the MAA units become ionized and form polyelectrolyte complexes with the positively charged PDMAEMA. These insoluble complexes form part of the cores of the micelles and cause a decrease of their size. Close to the isoelectric point, electrostatic interaction of the constituent blocks and the lack of net charges on one of them results in the insolubility of the copolymer.

1.1.4 Degree of protonation of weak acids/bases.

Besides the pH, the degree of protonation, α, of the polymer units is another parameter that can be used in order to describe the effect of acid or base addition in weak polyelectrolyte solutions. We define α as the ratio C_H/C_m, where C_H is the effective concentration of added acid and C_m is the polymer concentration in terms of monomeric units. When defined in this way, α approximates the degree of protonation of the polymer, assuming that all of the H^+ from the added acid protonate the polymer.

The relation between α and pH is not linear, but sigmoidal:

For weak acid: $$\alpha = \frac{1}{10^{pK_\alpha - pH} + 1}$$

For weak base: $$\alpha = \frac{1}{10^{pH - pK_\alpha} + 1}$$

A small change in the pH will, therefore, have a great effect on the degree of protonation, for pH values close to the effective pK_a of the weak polyelectrolyte. In fact, in the buffering region, α can change significantly while the pH remains fairly constant, and thus the pH does not fully depict what is happening to the polymer as acid or base is added.

In addition the term α is more useful than is the solution pH in order to describe more accurately the physics underlying the micellization process in pH sensitive diblock copolymers. The parameter that presicely determines the micelle formation is not the pH, which is related to the solvent surrounding the polymer chains but rather the actual degree of protonation of the polymer chains [8]. Thus, unlike most studies in the literature the degree of protonation will be used as a parameter in the present study to investigate structure formation in aqueous solutions of PHEGMA-*b*-PDEAEMA diblock copolymers.

1.1.5 Microgel particles

Microgels are cross-linked latex particles of submicrometer dimensions that can become highly swollen under certain conditions (**Figure 1.2**). Both thermo-responsive and pH-responsive microgels have been reported in the literature.

One type of microgel particles that has attracted particular academic interest due to their thermosensitivity are those based on poly(N-isopropylacrylamide) (PNIPAM) [32, 33]. Above the lower critical solution temperature of PNIPAM, (LCST 32º C) these lightly cross-linked PNIPAM particles exist in their nonsolvated latex-like form, while for temperatures below the LCST the particles become hydrophilic, and thus water-swollen microgels comprising chains held together by permanent cross-links are obtained. Recently, similar temperature-sensitive poly(N-vinylcaprolactam) (PVCL)-based microgel particles have also been prepared [34]. PVCL is a polymer closely resembling PNIPAM and shows an LCST in water around 32º C. Thus, the PVCL-based microgels exhibit a similar behavior to that described above for the PNIPAM particles.

Recently, pH-responsive microgels based on either acidic or basic monomer units have attracted great attention for use in biomedical and biotechnological applications such as delivery vehicles for protein-loaded vaccines [35].

The synthesis of acid-swellable microgel particles based on poly(2-diethylamino)ethyl methacrylate) (DEAEMA) (which are the microgel particles used in the present work) or poly(2-(diisopropylamino)ethyl methacrylate) (DPAEMA) was reported [36]. Reversible swelling occurred at low pH due to the protonation of the tertiary amine groups of the DEAEMA or DPAEMA residues. The critical pH for this latex-to-microgel transition was found around pH 6.5-7.0, which is in good agreement to the known pK_a of 7.0-7.3 for linear PDEAEMA homopolymer. PDPAEMA-based microgels had a lower critical swelling pH of around pH 5.0-5.5, which correlates with the lower pK_a of PDPAEMA homopolymer.

Monodispersed, cationic microgels were also synthesised by surfactant-free emulsion copolymerisation using 2-vinylpyridine (P2VP) and styrene [37]. Low levels of divinylbenzene (DVB) were used as a cross-linking agent. For styrene contents below 40 % by weight, the particles were spherical with diameters of approximately 200 nm. The particle diameter decreased with increasing styrene content and the morphology changed from spherical to irregular. The pH-dependent swelling of the microgel particles was studied, as a function of styrene content. Particle diameters increased below pH 4.6 due to protonation of the P2VP residues. For higher styrene levels, the critical transition pH was shifted to lower values and the extent to swelling was reduced.

Recently Kuckling et al. reported the synthesis of 'nanogels' that comprise both thermoresponsive PNIPAM cores and pH-sensitive P2VP-based coronas [38]. A sharp decrease of the average hydrodynamic diameter of the gels was observed by either increasing the temperature above 32º C or the pH above 5 where the PNIPAM cores or the P2VP coronas become respectively hydrophobic. It was also demonstrated that it is possible to obtain a response to one of the stimuli without the interference of the second stimulus.

In another study, Saunders et al. reported the swelling properties of PMMA-*b*-PMAA microgel particles dispersed in water as a function of pH and alkanol concentration [39]. These particles are sensitive to pH changes exhibiting a maximum swelling at pH ~ 8, when PMAA is ionized, while they deswell upon addition of an alcohol (methanol or 2-propanol) or poly(ethylene glycol) (PEG).

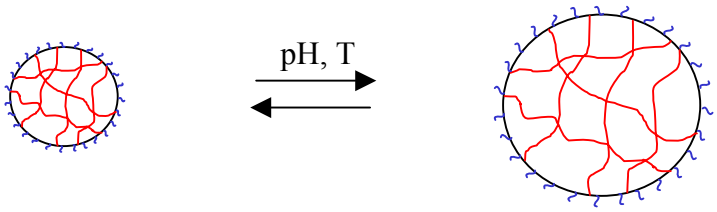

Figure 1.2 Schematic representation of the swelling- deswelling process.

1.1.6 Metal nanoparticles

Metal nanoparticles have unique properties and thus can find many applications as catalysts, semiconductors and magnetic fluids [40, 41, 42-44]. The physical and chemical properties of such nanosized metals may significantly differ from those of the corresponding bulk material [45-53] and are primarily determined by their size, structure and shape.

A large variety of metal nanoparticles, such as Au, Pt, Pd, Co etc. have been prepared in organic media using block copolymer micelles based on P2VP or P4VP [40, 46, 50, 52, 53]. In aqueous media, interaction of P2VP-*b*-PEO [47], PS-*b*-PEO [49], PEO-*b*-PEI [48, 54] diblock copolymers with metal compounds has been reported.

Nanoparticles of noble metals (Au, Pt) have mainly attracted interest for use in catalysis since they have a characteristic high surface-to-volume ratio, and consequently large fractions of the metal atoms that are exposed at surfaces are accessible to the reactant molecules. Polymer stabilized metal nanoparticles have been tested as catalysts in various reactions, such as hydrogenation, oxidation and C-C coupling reactions. Metal nanoparticles compete very well with the activity of the commercial catalysts while at the same time they exhibit a higher stability and selectivity conferred by the presence of the polymeric stabilizer and the surface of the particles respectively [40, 42, 43, 45, 52, 55].

The production of particles that are uniform in size and shape is still a challenging task, although several synthetic methods to prepare such systems have been developed. In order to control the size and shape of the particles, the synthesis is based on the appropriate control of the parameters that influence nucleation and

growth. The use of ligands (stabilizing agents) such as surfactants and polymers is very common in the specific control of growth and in the prevention of agglomeration of the particles once they have been synthesized [53].

However, the disadvantages of the traditional routes to nanoparticles are obvious: the large interface area costs a lot of energy and requires large amounts of stabilizer or embedded surface units. The simple nucleation and growth route demands very low concentrations of the formed colloids, i.e., the mass output is low. Concentrating the products usually leads to the failure of stabilization and the formation of larger aggregates. For these reasons, some modern techniques make use of synthesis in mesoscopically confined geometries, such as in vesicles, zeolites, micelles, organic or inorganic gels [45, 46, 56].

Nanoparticle formation in block copolymer systems can be considered a further advancement of these techniques. However, inorganic materials can be incorporated into polymers only through specific interactions like dipolar interactions, hydrogen bonding, complex formation, or covalent bonding. Control over the size and shape of the metal colloids in such polymeric materials can be achieved by growing the desired colloids within microdomains of suitable size and shape.

Several methods for the preparation of metal nanoparticles in a polymeric nanoenvironment have been suggested. One of them involves metal colloid preparation in the cores of amphiphilic block copolymer micelles formed in selective solvents. In such systems, the nonpolar blocks form the corona, which provides solubilization and stabilization, while the polar block forms the core, which is able to dissolve metal compounds due to coordination. Such a micellar core can be considered as nanoreactor, where nucleation and growth of metal particles upon metal reduction are restricted to mesoscale level [45, 46, 40, 50].

It seemed appropriate to apply a similar method to aqueous systems because water is a fascinating solvent from the viewpoint of environmental considerations. Furthermore, amphiphilic block copolymer micelles in water can be considerd as potential carriers for drug-delivery. However, amphiphilic block copolymers in water produce micelles with a nonpolar core which cannot coordinate metal precursors. Hence metal particles only form in the corona of micelles, and the hybrids produced are only weakly stabilized. A promising way to develop nanostructures in otherwise

nonstructured aqueous solutions, is to use double-hydrophilic block copolymers as the stabilizing system. The one block, in such a system, is able to coordinate with the metal compound forming the micelle core while the other block provides good solubility in water [47, 48, 49, 54]. The metal compounds (e.g., H_2PtCl_6, $HAuCl_4$) can either be introduced in a micellar solution, where they are incorporated within the micelle core via coordination with the functional groups (**Figure 1.3a**), or can be added to a unimer solution at low pH, where they lead to a metal-induced micellization process (**Figure 1.3b**) [57, 58].

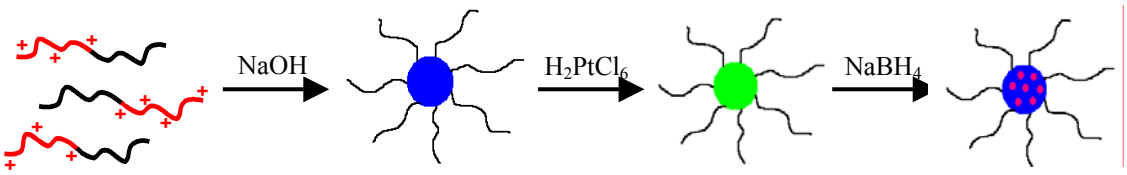

(a)

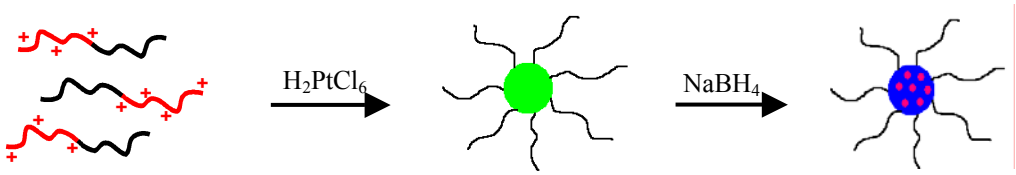

(b)

Figure 1.3 Schematic representation of the metallation process, followed by metal reduction (a) metal incorporation within the micelle core, (b) metal induced micellization.

Recently, responsive microgel particles were used as stabilizers for metal nanoparticles. Microgels can be tailored in order to bear pendant functional groups able to interact with metal ions or complexes, which are subsequently reduced inside the microgel to yield metal nanoparticles (**Figure 1.4**). In this way, an early interaction between the stabilizing polymer and the reduced metal atom precursors is established, which is important in order to gain control of the size and size distribution of the resulting metal nanoparticles [56, 59, 60]. Synthesis of colloidal

metal nanoparticles in polymer microgel matrices is more effective than that in polymer micelles since the former retain colloidal stability over a broad range of conditions.

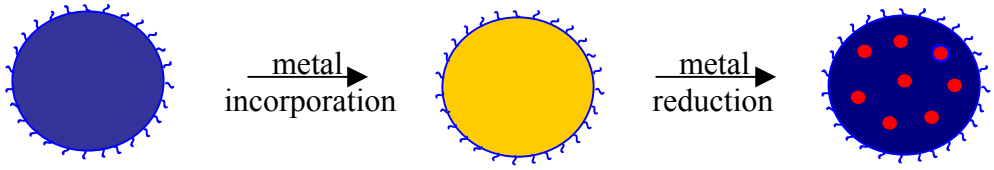

Figure 1.4 Schematic representation of metal incorporation and metal nanoparticle formation within microgel particles.

1.1.7 Current work

In the present study, we examined the solution properties of pH-responsive polymer materials in water. Two different systems both of which contained pH-sensitive (2-diethylamino)ethyl methacrylate) units were investigated: PDEAEMA-based double hydrophilic diblock copolymers and PDEAEMA-based microgel particles.

The diblock copolymers comprise a neutral, hydrophilic poly(hexa(ethylene glycol) methacrylate) (PHEGMA) block and an ionizable pH-tunable poly(2-diethylamino)ethyl methacrylate) (PDEAEMA) block (**Figure 1.5**). PHEGMA is soluble over the whole pH range while PDEAEMA is soluble only at low pH.

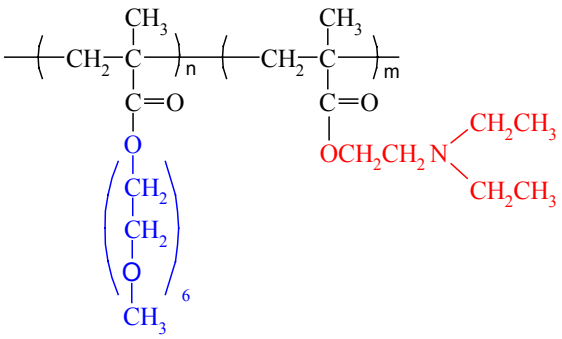

soluble in water (PHEGMA) **soluble in acid (PDEAEMA)**

Figure 1.5 Chemical structure of the pH-sensitive diblock copolymers.

At low pH the copolymer is in its unimer state due to the hydrophilicity of the protonated DEAEMA units, while an increase of the solution pH above 7 results in the deprotonation of the amine groups, which become hydrophobic and lead to the formation of micelles. PDEAEMA forms the micelle cores while the hydrophilic PHEGMA in the micelle corona stabilizes the structures in solution. In this study, we examined the effect of the degree of protonation (α) of the PDEAEMA block on the solution properties of the diblock copolymers in water by dynamic light scattering and ^{1}H NMR spectroscopy.

The second system investigated was that of microgel particles, consisting of chemically crosslinked PDEAEMA chains stabilized by short PEO chains of 2,000 molecular weight (**Figure 1.6**).

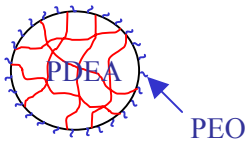

Figure 1.6 Microgel particles**.**

These microgels exhibit reversible swelling properties in water by adjusting the solution pH. Thus at low pH the microgel particles are swollen due to the hydrophilicity of the protonated amine units, while an increase of the solution pH leads to the deprotonation of the DEAEMA units and the formation of hydrophobic latex particles. The aqueous solution behavior of the microgel particles was investigated as a function of solution pH by dynamic light scattering.

In the second part of this work we examined the formation of colloidal metal nanoparticles within the above polymeric matrices. The polymer behavior upon metallation and the metal nanoparticle characteristics were investigated.

For the diblock copolymers, platinum nanoparticles were grown within the cores of the micelles by incorporation of metal compounds (H_2PtCl_6, K_2PtCl_6) followed by metal reduction. The polymer behavior upon metal incorporation and metal reduction, while varying the solution pH, were studied by DLS and ^{1}H NMR

experiments.The metallation process was also followed by UV/Vis spectroscopy, while the metallated micelles and the metal nanoparticle characteristics were studied by TEM. The crystalline structure of the metal nanoparticle was confirmed by X- Ray diffraction.

Metal nanoparticles were also formed within the microgel particles upon addition of H_2PtCl_6 followed by metal reduction with $NaBH_4$. The microgel swelling properties were studied by dynamic light scattering while UV/Vis spectroscopy was used to investigate the polymer-metal interactions. The metallation process as well as the metal nanoparticle characteristics were studied by TEM. XRD studies confirmed the crystalline structure of the metal nanoparticles and also allowed to estimate the size of the nanoparticles.

1.2 References

[1] A. Harada, K. Kataoka *Macromolecules*, 1995, **28**, 5294-5299.

[2] D. L. Elbert, C. B. Herbert, and J. A. Hubbell *Langmuir*, 1999, **15,** 5355-5362.

[3] Q. Cai, K. Zeng, C. Ruan, T. A. Decai, C. A. Grimes *Anal. Chem*, 2004, **76(17)**, 4038-4043.

[4] M. Vamvakaki, N. C. Billingham, S. P. Armes *Macromolecules*, 1999, **32**, 2088-2090.

[5] V. Bütün, C. E. Bennett, M. Vamvakaki, A. B. Lowe, N. C. Billingham, and S. P. Armes *J. Mater. Chem.*, 1997, **7**, 1693-1695.

[6] L. Brunsveld, H. Zhang, M. Glasbeek, J. A. J. M. Vekemans, and E. W. Meijer *J. Am. Chem. Soc.*, 2000, **122**, 6175-6182.

[7] K. Szczubialka, M. Nowakowska *Polymer*, 2003, **44**, 5269-5274.

[8] A. S. Lee, A. P. Gast, V. Bütün, S. P. Armes *Macromolecules*, 1999, **32**, 4302-4310.

[9] M. Vamvakaki, G.-F. Unali, V. Bütün, S. Boucher, K. L. Robinson, N. C. Billingham, S. P. Armes *Macromolecules*, 2001, **34**, 6839-6841.

[10] J.–F. Gohy, S. Antoun, R. Jérôme *Macromolecules*, 2001, **34**, 7435-7440.

[11] T. J. Martin, K. Prochazka, P. Munk, S. E. Webber *Macromolecules*, 1996, **29**, 6071-6073.

[12] G. D. Poe, W. L. Jarrett, C. W. Scales, and C. L. McCormick *Macromolecules*, 2004, **37**, 2603-2612.

[13] S. K. Pearsall, M. M. Green, and H. Morawetz *Macromolecules*, 2004.

[14] (a) J. M. Ed. Lehn *Comprehensive Supramolecular Chemistry*, Pergamon Press: New York, 1996, (b) A. J. Bard *Integrated Chemical Systems*, Wiley, New York, 1995, (c) J. M. Lehn *Polym. Int.*, 2002, **51**, 825-839.

[15] S. E Webber *J. Phys. Chem. B*, 1998, **102**, 2618-2626.

[16] J.–F. Gohy, S. K. Varshney, R. Jérôme *Macromolecules*, 2001, **34**, 3361-3366.

[17] J.–F. Gohy, S. Creutz, M. Garsia, B. Mahltig, M. Stamm, R. Jérôme *Macromolecules*, 2000, **33**, 6378-6387.

[18] J. Ding, G. Liu *Macromolecules*, 1997, **30**, 655-657.

[19] K. Yu, A. Eisenberg *Macromolecules*, 1998, **31**, 3509-3518.

[20] M. E. Cowan, R. D. Hester, C. L. Mc Cormic *J. Appl. Polym. Sci.*, 2001, **82**, 1211-1221.

[21] M. Arotcaréna, B. Heise, S. Ishaya, A. Laschewsky *J. Am. Chem.*, 2002, **124**, 3787-3793.

[22] J.–F. Gohy, B. G. G. Lohmeijer, S. K. Varshney, and U. S. Schubert *Macromolecules*, 2002, **35**, 7427-7435.

[23] L. Zhang, K. Khougaz, M. Moffitt, A. Eisenberg, In Amphiphilic Block Copolymers, B. Lindam Edts, *Elsevier: Amsterdam*, 2000, p87-114.

[24] M. Vamvakaki, N.C. Billingham, and S.P. Armes *Polymer*, 1998, **39**, 2331-2337.

[25] F. L. Baines, N. C. Billingham and S. P. Armes *Macromolecules*, 1996, **29,** 3416-3420.

[26] S.–i. Yusa, Y. Shimada, Y. Mitsukami, T. Yamamoto, Y. Morishima *Macromolecules*, 2003, **36**, 4208-4215.

[27] S. Holappa, L. Kantonen, F. M. Winnik, and H. Tenhu *Macromolecules*, 2004, **37**, 7008-7018.

[28] V. Bütün, N.C. Billingham, S. P. Armes *J. Am. Chem. Soc*, 1998, **120**, 11818.

[29] I. B. Dicker, G. M. Cohen, W. B. Farnham, W. R. Hertler, E. D. Langanis, D. Y. Sogah *Macromolecules*, 1990, **23**, 4034

[30] S. Liu, N. C. Billingham, S. P. Armes *Angewandte Chem. Int. Ed.* 2001, **40**, 2328.

[31] V. Bütün, S. P. Armes, N. C. Billingham *Polymer*, 2001, **42**, 5993.

[32] Y. Deng, R. H. Pelton *Macromolecules*, 1995, **28**, 4617.

[33] C. D. Jones, L. A. Lyon *Macromolecules*, 2000, **33**, 8301-8306.

[34] A. Laukkanen, S. Hietala, S. L. Maunu, and H. Tenhu *Macromolecules*, 2000, **33**, 8703-8708.

[35] N. Murphy, M. Xu, S. Schuck, J. Kunisawa, N. Shastri, J. M. J. Frechet *Proc. Natl. Acad. Sci.* 2003, **100**, 4995.

[36] J. I. Amalvy, E. J. Wanless, Y. Li, V. Michailidou, S. P. Armes, Y. Duccini *Langmuir*, 2004, **20**, 8992-8999.

[37] A. Loxley, B. Vincent *Colloid Polym. Sci.* 1997, **275**, 1108-1114.

[38] D. Kuckling, C. D. Vo, S. E. Wohlrab *Langmuir*, 2002, **18**, 4263-4269.

[39] B. R. Saunders, H. M. Crowther, B. Vincent *Macromolecules*, 1997, **30**, 482.

[40] L. M. Bronstein, P. M. Valetsky, and M. Antonietti *Polymer Science*, 1997, **39**, 1249-1256.

[41] A. Roucoux, J. Schulz, and H. Patin *Chem. Rev.,* 2002, **102**, 3757- 3778.

[42] S. Förster, M. Antonietti *Adv. Mater.*, 1998, **10**, 193-217.

[43] O. Platonova, L. Bronstein, S. P. Solodovnikov, I. M. Yanovskaya, E. S. Obolonkova, P. M. Valetsky, E. Wenz, M. Antonietti *Colloid Polym Sci*, 1997, **275**, 426-431.

[44] L. LaConte, N. Nitin, and G. Bao *Nano Today*, May 2005, ISSN:1369 7021.

[45] M. V. Seregina, L. M. Bronstein, O. A. Platonova, D. M. Chernyshov, P. M. Valetsky, J. Hartmann, E. Wenz, and M. Antonietti *Chem. Mater.*, 1997, **9**, 923-931.

[46] S. Mössmer, J. P. Spatz, M. Möller, T. Aberle, J. Schmidt, and W. Burchard, *Macromolecules*, 2000, **33**, 4791-4798.

[47] L. M. Bronstein, S. N. Sidorov, P. M. Valetsky, J. Hartmann, H. Cölfen, and M. Antonietti *Langmuir*, 1999, **15**, 6256-6262.

[48] L. M. Bronstein, S. N. Sidorov, A. Y. Gourkova, D. M. Chernyshov, J. Hartmann, M. Breulmann, H. Cölfen, M. Antonietti *Inorg. Chim. Acta*, 1998, **280**, 348-354.

[49] L. M. Bronstein, D. M. Chernyshov, G. J. Timofeeva, L. V. Dubrovina, P. M. Valetsky, E. S. Obolonkova, A. R. Khokhlov *Langmuir*, 2000, **16**, 3626-3632.

[50] H. Zhao, E. P. Douglas, B. S. Harrison, and K. S. Schanze *Langmuir*, 2001, **17**, 8428-8433.

[51] D. M. Chernyshov, L. M. Bronstein, H. Börner, B. Berton, and M. Antonietti *Chem. Mater.*, 2000, **12**, 114-121.

[52] S. Pathak, M. T. Greci, R. C. Kwong, K. Mercado, G. K. S. Prakash, G. A. Olah, and M. E. Thompson *Chem. Mater*., 2000, **12**, 1985-1989.

[53] M. Antonietti, E. Wenz, L. M. Bronstein, and M. V. Seregina *Adv. Mater.*, 1995, **7**, 1000-1005.

[54] S. N. Sidorov, L. M. Bronstein, P. M. Valetsky, J. Hartmann, H. Cölfen, H. Schnablegger, and M. Antonietti *J. Colloid Int. Sci.*, 1999, **212**, 197-211.

[55] E. Sulman, Yu. Bodrova, V. Matveeva, N. Semagina, L. Cerveny, V. Kurtc, L. Bronstein, O. Platonova, P. Valetsky *Applied Catalysis A*, 1999, **176**, 75- 81.

[56] A. Biffis and E. Sperotto *Langmuir*, 2003, **19**, 9548-9550.

[57] M. Vamvakaki, L. Papoutsakis, V. Katsamanis, T. Afchoudia, P. G. Fragouli, H. Iatrou, N. Hadjichristidis, S. P. Armes, S. Sidorov, D. Zhirov, V. Zhirov, M. Kostylev, L. Bronstein and S. H. Anastasiadis *Faraday Discuss.*, 2005, **128,** 9747-9755.

[58] L. Bronstein, M. Vamvakaki, M. Kostylev, V. Katsamanis, B. Stein and S. H. Anastasiadis *Langmuir*, 2005, **21**, 9747-9755.

[59] A. Biffis, N. Orlandi, and B. Corain *Adv. Mater.*, 2003, **15**, 1551- 1555.

[60] L. M. Bronstein, O. A. Platonova, A. N. Yakunin, I. M. Yanovskaya, and P. M. Valetsky *Langmuir*, 1998, **14**, 252-259.

Chapter 2

2.1 Materials

2.1.1 Copolymer synthesis

In this work we have used poly(hexa(ethylene glycol) methacrylate)-*b*-poly(2-diethylamino)ethyl methacrylate) (PHEGMA-*b*-PDEAEMA) diblock copolymers [1]. Group transfer polymerization was used to synthesize these copolymers (see **Figure 2.1)**. Gel permeation chromatography (GPC) was used to characterize the copolymers in terms of their molecular weights (M_n's) and molecular weight distributions (M_w/M_n) while block copolymer compositions were determined by proton nuclear magnetic resonance spectroscopy (^{1}H NMR). **Table 1** summarizes the copolymers prepared and their GPC and ^{1}H NMR characterization data.

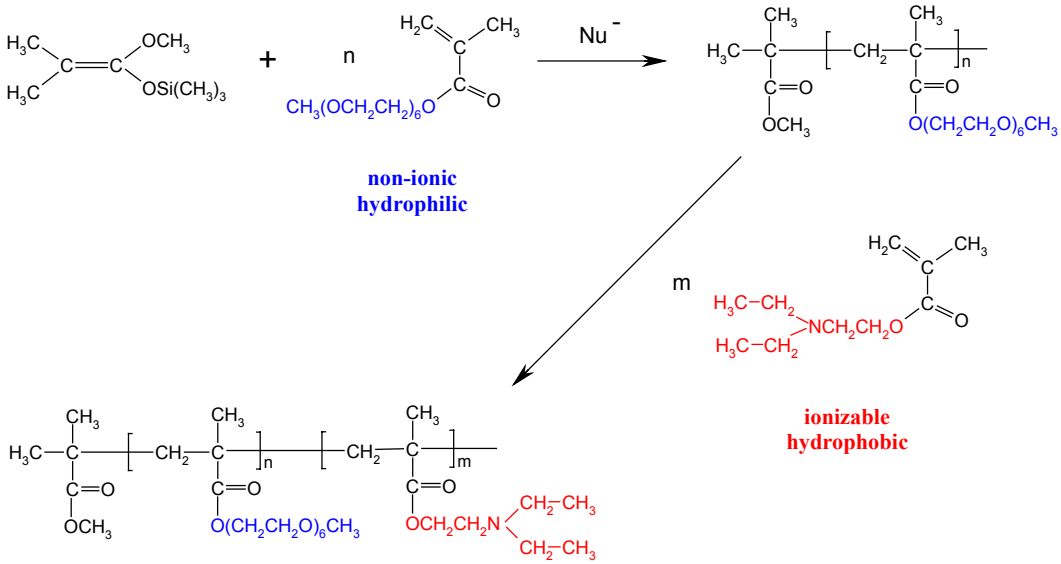

Figure 2.1 Synthesis of the diblock copolymers by group transfer polymerization.

Table 1. Molecular Characteristics of the Diblock Copolymers

Copolymers[α]	DEAEMA	HEGMA	(^{1}H NMR)	M_n	M_w/M_n
H30	-	30	-	6 120	1.13
H30-*b*-D30	30	30	51-49	9 280	1.14
H50-*b*-D20	20	50	70-30	10 000	1.14
H50-*b*-D30	30	50	58-42	11 400	1.16
H50-*b*-D34	34	50	61-39	11 700	1.15
H50-*b*-D40	40	50	56-44	12 300	1.13
H50-*b*-D50	50	50	49-51	13 500	1.14

[α] H and D are additional abbreviations for HEGMA and DEAEMA respectively. The numbers denote degrees of polymerization.

2.1.2 Microgel synthesis

Microgel synthesis was carried out in a one litre round-bottomed flask, fitted with a nitrogen gas inlet, water condenser and an overhead mechanical stirrer [2]. The required amount of water (typically 85 g) and a mixture of DEA and poly(propylene glykol)methacrylate (PPGDA) cross-linker (typically 10.5g) were added to the flask and the solution was stirred for 30 min under a nitrogen flow at 70 ºC. The polymerization commenced on addition of a previously degassed aqueous solution (typically 5.0g) of the APS initiator (1.0 wt% based on monomer). The required amount of the reactive macromonomer stabilizer (typically 10.0 wt% based on monomer) was added to the aqueous solution prior to the addition of the monomer and cross-linker. The latex particles were sterically stabilized by employing monomethoxy-capped poly(ethylene glycol) methacrylate (PEGMA) as a macromonomer. Ultrafiltration was used to eliminate excess stabilizer, as well as traces of monomer and initiator, in order to purify the PDEAEMA latex particles. **Figure 2.2** illustrates the synthetic route for cross-linked, sterically-stabilized poly(DEAEMA) latex particles.

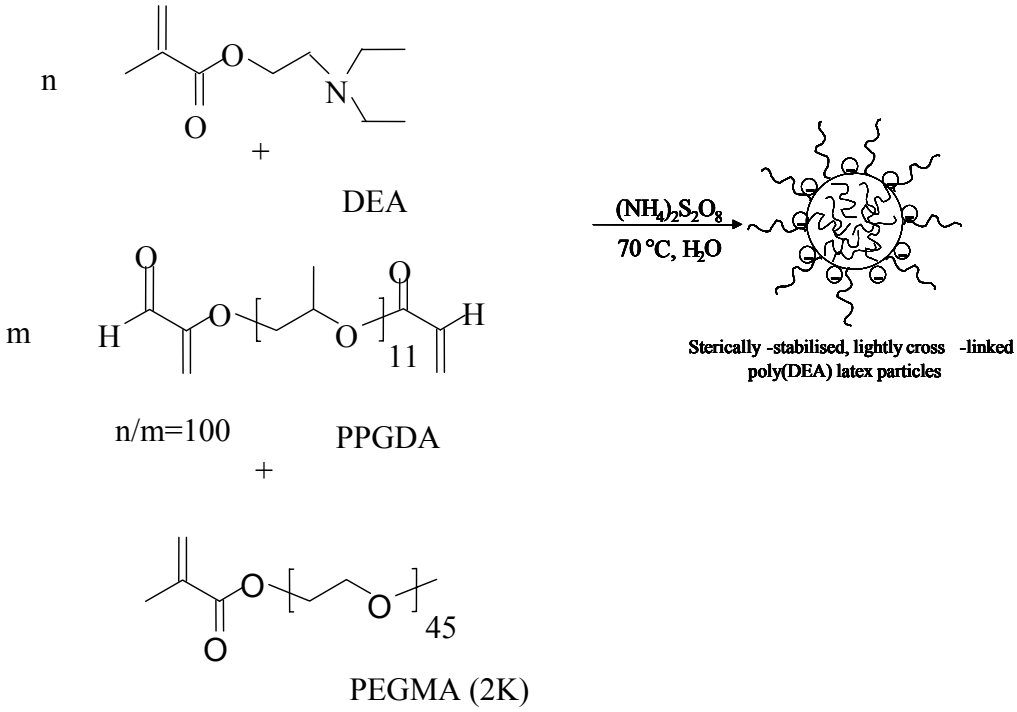

Figure 2.2 Synthetic route for lightly cross-linked, sterically-stabilized poly(DEAEMA) latex particles.

2.2 Experimental techniques

2.2.1 Dynamic light scattering

The interaction of light with matter can be used to obtain important information about the structure and dynamics of matter. Light scattering experiments are based on such light-matter interactions.

Furthermore, when light impinges on matter it is either scattered or absorbed, thus providing information about the electronic, vibrational and rotational degrees of freedom of the molecules. From this interaction, photons can either impact or gain energy and they thereby suffer frequency shifts. Thus the frequency spectrum of the light will exhibit resonances at the frequencies corresponding to these transitions.

When light impinges on matter, the electric field of the light induces an oscillating polarization of the electrons in the molecules. The molecules then serve as a secondary source and scatter light. The frequency shifts, the angular distribution, the polarization and the intensity of the scattered light are determined by the size, shape

and the molecular interaction in the scattering material. Thus from the light scattering characteristics of a given system it should be possible, with the aid of the theory of time dependent statistical mechanics and electromagnetism, to obtain information about the structure and molecular dynamics of the scattering medium [3, 4].

Light scattering can occur with a shift in the frequency of the incoming light (inelastic light scattering), or not (elastic light scattering). The elastic scattering is called Rayleigh scattering and deals with the characteristics of the light scattered from the translational and rotational degrees of freedom. On the other hand, vibrational degrees of freedom give Raman scattering. The development of laser techniques enabled the measurement of very small frequency shifts in the light scattered from matter, because of their high intensity that measures even weak scattering from molecules.

The basic theory of Rayleigh scattering was developed more than half a century ago by Rayleigh, Mie, Smoluchowski, Einstein, and Debye. Light scattering was first studied experimentally by Tyndall and then theoretically by Rayleigh. These studies concerned scattering from assemblies of noninteracting particles sufficiently small compared to the wavelength of the light to be regarded as point dipole oscillations. Rayleigh explained the blue color of the sky and the red sunset as due to the preferential scattering of the blue light by the molecules in the atmosphere. Later, Rayleigh derived the full formula of scattered light from spheres of arbitrary size.

Although Rayleigh developed a theory of light scattering from gases with some success, it was found that the intensity of scattering by condensed phases was more than one order of magnitude lower than that predicted by his formula. This effect was correctly attributed to the destructive interference between the wavelets scattered from different molecules. Smoluchowski and Einstein elegantly circumvented this difficulty by considering the light to be a continuous medium in which thermal fluctuations give rise to local inhomogeneities and thereby to the intensity and concentration fluctuations. These authors developed the fluctuation theory of light scattering. According to this theory, the intensity of the scattered light can be calculated from the mean square fluctuations in density and concentration that in turn can be determined from macroscopic data such as the isothermal compressibility and the concentration dependence of the osmotic pressure. The

intensity of the light is thus obtained without considering the detailed molecular structure of the medium. This approach to light scattering has played a very important role in the theory of light scattering.

Dynamic light scattering examines the relaxation time of the fluctuations providing information in reciprocal space for the spatial Fourier length $2\pi/q$, where q is the scattering vector. This length is related to a characteristic time, which is the time that the particle needs to travel the distance $2\pi/q$.

In a light-scattering experiment, light from a laser passes through a polarizer to define the polarization of the incident beam and then impinges on the scattering medium. The scattered light then passes through an analyzer which selects a given polarization and finally enters the detector. The position of the detector defines the scattering angle θ. In addition, the intersection of the incident beam and the beam intercepted by the detector defines a scattering region of volume V. This is illustrated in **figure 2.3**. The quantity measured in a light-scattering experiment is the time-correlation function of the scattered intensity I(t). Based on the continuous movement of the molecules their position changes and the scattered intensity fluctuates. The fluctuations of I(t) are characterized by the diffusion coefficient, D.

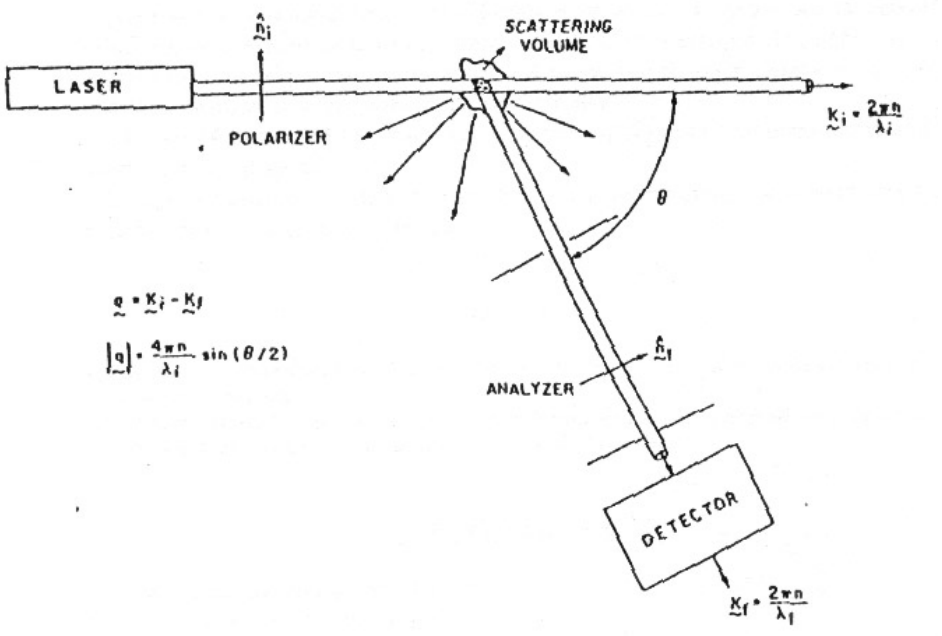

Figure 2.3 Typical experimental setup for a light scattering experiment.

Electromagnetic theory

The theory of light scattering can be developed on the basis of quantum field theory. The major results of this theory differ little from the classical theory of light scattering. So we do not dwell on the electrodynamical theory.

Consider a nonmagnetic, nonconducting, nonabsorbing medium with average dielectric constant ε_o and refractive index n = $\sqrt{\varepsilon_o}$. Let the incident electric field be a plane wave of the form:

$$\mathrm{E}_i(\vec{r},t) = \hat{n}_i E_o \exp i(\vec{k}_i\vec{r} - \omega_i t) \tag{2.1}$$

where n_i is a unit vector in the direction of incident electric field; E_o is the field amplitude; k_i is the propagation vector and ω_i is the angular frequency.

This plane wave is incident upon a medium that has a local dielectric constant:

$$\vec{\vec{\varepsilon}}(\vec{r},t) = \varepsilon_o \vec{\vec{I}} + \delta\vec{\vec{\varepsilon}}(\vec{r},t) \tag{2.2}$$

where $\delta\varepsilon$(r,t) is the dielectric constant fluctuation tensor at position r and time t and I is the second-rank unit tensor.

It can be shown that the component of the scattered electric field at a large distance R from the scattering volume with polarization n_f, propagation vector k_f, and frequency ω_f is:

$$E_s(R,t) = \frac{E_o}{4\pi R\varepsilon_o}\exp(ik_f R)\int_V d^3r \exp[i(\vec{q}\cdot\vec{r} - \omega_i t)][\vec{n}_f \cdot [\vec{k}_f \times (\vec{k}_f \times (\delta\vec{\vec{\varepsilon}}(\vec{r},t)\cdot\vec{n}_i))]] \tag{2.3}$$

where the subscript V indicates that the integral is over the scattering volume. The vector q is defined in terms of the scattering geometry as $\vec{q} = \vec{k}_i - \vec{k}_f$ where k_i and k_f point, in the directions of propagation of the incident wave and of the wave that reaches the detector respectively. This is illustrated in **figure 2.4**. The angle between k_i and k_f is called the scattering angle.

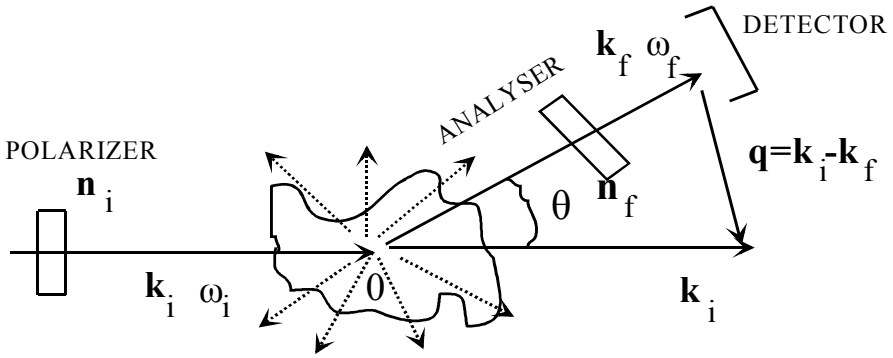

Figure 2.4 Light of polarization n_i and wave vector k_i is scattered in all directions. Only scattered light of wave vector k_f and polarization n_f arrives at the detector. The scattering vector $\vec{q} = \vec{k}_i - \vec{k}_f$ is defined by the geometry.

The magnitude of k_i and k_f are respectively $2\pi n/\lambda_i$ and $2\pi n/\lambda_f$ where λ_i and λ_f are the wavelengths of the incident and scattered radiation and n is the refractive index of the scattering medium. It is usually the case that the wavelength of the incident light changes very little in the scattering process so that $|k_i| \cong |k_f|$ and the scattering vector is:

$$q^2 = |k_i - k_f|^2 = k_i^2 + k_f^2 - 2k_i \cdot k_f = 2k_i^2 - 2k_i^2 \cos\theta = 4k_i^2 \sin^2\left(\frac{\theta}{2}\right) \Rightarrow$$
$$q = 2k_i \sin\left(\frac{\theta}{2}\right) = \left(\frac{4\pi n}{\lambda_i}\right)\sin\left(\frac{\theta}{2}\right) \tag{2.4}$$

This condition specifies the wave vector component of the dielectric constant fluctuations that will give rise to scattering at an angle θ.

Spatial Fourier transform of the dielectric fluctuations $\delta\vec{\varepsilon}(\vec{q},t) = \int_V d^3r \exp[i(\vec{q}\cdot\vec{r})]\delta\vec{\varepsilon}(r,t)$ and **equation 2.3** gives:

$$E_s(R,t) = \frac{-k_f^2 E_o}{4\pi R\varepsilon_o}\exp[i(k_f R - \omega_i t)]\delta\varepsilon_{if}(q,t) \tag{2.5}$$

where

$$\delta\varepsilon_{if}(\vec{q},t) \equiv \vec{n}_f \cdot \delta\vec{\varepsilon}(\vec{q},t) \cdot \vec{n}_i \tag{2.6}$$

is the component of the dielectric constant fluctuation tensor along the initial and final polarization directions. The time-correlation function of electric field is:

$$< E_s^*(R,0)E_s(R,t) >= \frac{k_f^4 \mid E_o \mid^2}{16\pi^2 R^2 \varepsilon_o^2} \left\langle \delta\varepsilon_{if}(\vec{q},0)\delta\varepsilon_{if}(\vec{q},t) \right\rangle \exp(-i\omega_i t) \qquad (2.7)$$

and the spectral density of scattered light is:

$$\mathrm{I}(\vec{q},\omega_\mathrm{f},\mathrm{R}) = \left[\frac{|\mathrm{E_o}|^2 \mathrm{k_f^4}}{16\pi^2 \mathrm{R}^2 \varepsilon_\mathrm{o}^2} \right] \frac{1}{2\pi} \int_{-\infty}^{\infty} \mathrm{dt} < \delta\varepsilon_{if}(\vec{q},0)\delta\varepsilon_{if}(\vec{q},\mathrm{t}) > \exp[\ \mathrm{i}(\omega_\mathrm{f} - \omega_\mathrm{i})\mathrm{t}] \qquad (2.8)$$

Equation 2.8 indicates the inverse λ^4 and R^2 dependence of the characteristics of any spherical wave. The λ^4 dependence is related to the observation that the blue light is scattered more than red light. It also indicates that radio waves would not be scattered as much as visible light. As a consequence of the larger scattering intensities, it is much easier to perform scattering experiments with visible light than with longer wavelength infrared or radio waves. It should be also noted that **equation 2.8** is an expression for the light spectral density in terms of dielectric constant fluctuations. In a medium that dielectric constant does not fluctuate the light is scattered only in the q=0 direction.

The above theoretical expression is purely phenomenological. Any attempt to write this formula in molecular terms will necessarily involve some degree of approximation, nevertheless, it will contribute significantly in our intuitive understanding of light scattering and will be useful for practical applications.

Photon correlation spectroscopy (PCS)

In a photon correlation spectroscopy experiment the measured quantity is the normalized autocorrelation function of the scattered intensity *G(q,t)*, in polarized ($G_{VV}(q,t)$) or depolarized ($G_{VH}(q,t)$), geometry:

$$G(q,t) = \frac{< I(q,t)\, I(q,0) >}{< I(q,0) >^2} \qquad (2.9)$$

Polarized geometry gives us information about the fluctuations of the concentration or the density of the material, while the depolarized one gives us information regarding the fluctuations of the orientation of the molecules. Only the polarized geometry has been used in this thesis. The quantity related with the dynamic response of the system is the autocorrelation function of the scattered field, g(q,t). The two autocorrelation functions are related via Siegert's relation:

$$G(q,t) = 1 + f^{*}(\alpha g(q,t))^{2} = 1 + f^{*} \mid C(q,t) \mid^{2} \qquad (2.10)$$

Where f^{*} is a spatial coherence factor that depends on the experimental setup, the scattered volume and the number of coherence areas viewed. The factor α is the scattered intensity percent in dynamics that can be measured with PCS. The advantages of photon correlation spectroscopy are the large range of intervals (10^{-6}-10^{3}s) and the different relaxation times that can be measured at the same time.

Experimental setup

The experimental setup is shown in **Figure 2.5**. Scattering angles between 150^{o}-11^{o} ($q=2.28\text{x}10^{-2}$-$2.26\text{x}10^{-3}$ nm^{-1}) can be measured. The laser is ND-YAG with a monochromatic beam at 532 nm (Adlas DPY 315II). The maximum power is ~100 mW, but 80 mW was used to ensure power stability, and the diameter of the beam was 0.32 mm (TEM_{00}). The incident beam passes through optics (two mirrors M1, M2 and a polarizer P1) and a lens (F1) before it impinges the sample. The intensity and position of the beam are continuously recorded on a four Photo Diode system (PD). The sample is contained in an optical glass cell of a diameter of 10 mm, and is placed in a bath that contains toluene in order to equate the refractive indexes (glass and toluene) and avoid refraction comes from the glass surface. The scattered beam pass through an optical system of a lens and two holes H1, H2 before it impinges the amplifier. The lens is 2f/2f and is placed in a distance equal to 2f from the scattering volume and the second hole H2 respectively. The amplifier is a photomultiplier (THORN EMI).

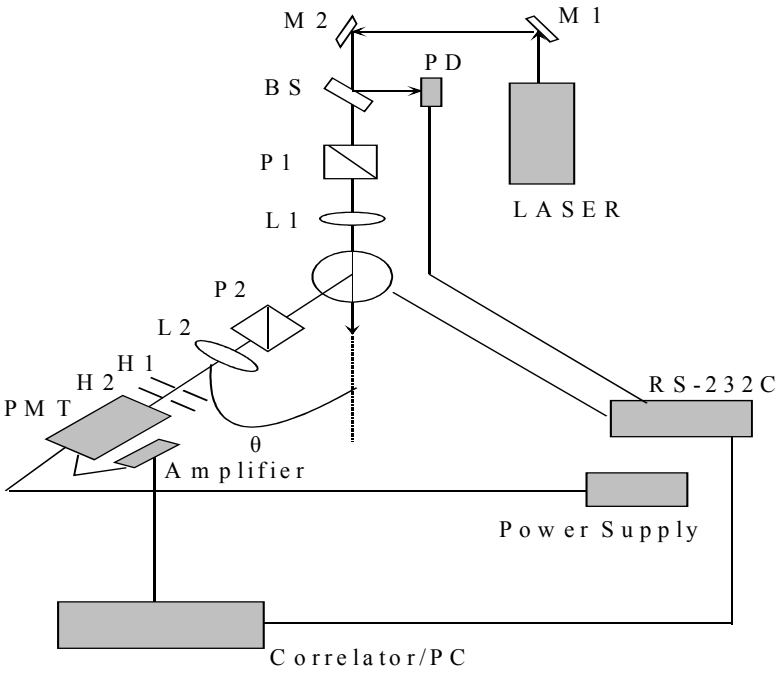

Figure 2.5 Experimental setup used for photon correlation spectroscopy.

The two holes H1 and H2 (0.3mm diameter) define the scattering volume. The polarization of the beam is defined by the two polarizers P1 and P2. The incoming beam is always polarized perpendicular to the scattering plane while P2 can be rotated so that both polarized (V) and depolarized (H) components are accessible. The bath temperature which is also the sample temperature, is controlled by the circulation of a thermostatic liquid (mixture of water and glycol) by means of a thermostat. Temperatures between 10^{o} C – 50^{o} C can be measured. A Bus Controller RS-232C device controls the goniometer. A computer, embedded with an electronic correlation card, controls the whole setup. The software used is ALV-5000/E photon correlator. Details regarding the photon correlator are given in the next paragraph.

Correlator

The correlator is the most important device of the photon correlation spectroscopy setup. It comprises an electronic card that calculates the correlation function [5] of an electronic signal as following:

a) First, it counts the photoelectronic pulses n(t), during a storage time t_s (sample time), during the real time t of the experiment
b) Second, it lags the samples for integer multiplies of the sample time $\tau=kt_s$ (lag time)
c) Next, it multiplies the real and time results with the lag time
d) Finally, it sums the products

From the above $n(q,t+\tau)n(q,t)$ is calculated over the duration of the whole measurement, for different values of τ while the photon correlation function is also calculated:

$$G(\tau) =< n(t+\tau)n(t) >= \lim_{T\to\infty} \frac{1}{T} \int_{-T}^{T} n(t+\tau)n(t)dt \qquad (2.11)$$

Which can be approximated by:

$$G(\tau) = \sum_{i=0}^{N-1} n_i n_{i+k} \qquad (2.12)$$

Normalization of the above equation gives:

$$G_{norm}(q,t) = \frac{< n(q,t)n(q,0) >}{< n(q,0) >^2} \qquad (2.13)$$

The photon correlator, used in this study, is an ALV-5000 Multi Tau Digital Correlator with 280 channels which can make $2x10^9$ multiplies/sums per second.

Correlation function analysis

The correlation function of a 0.1 wt% PHEGMA-*b*-PDEAEMA diblock copolymer solution dissolved in water at pH 6 is shown **Figure 2.6 (a)**. The above mentioned experimental setup was used for this measurement. The correlation

function of **Figure 2.6 (a)** is described with a single exponential decay and can be fitted with a function of the form C*(q,t)* = α exp(-t/τ) which gives the intensity (~α) and the relaxation time (τ).

In most cases the correlation function is not as simple as described above and it gives more than one relaxation processes, as shown in **Figure 2.6 (b)**. In this case, in order to analyze the correlation function we use the inverse Laplace transformation, with the aid of the program CONTIN, which takes that C*(q,t)* is an exponential overlapping:

$$C(q,t) = \int_{-\infty}^{\infty} L(\ln\tau)\exp(-t/\tau)d(\ln\tau) \qquad (2.14)$$

This equation describes the relaxation time distribution L[ln(τ)] (**Figure 2.6 (a)** inset)

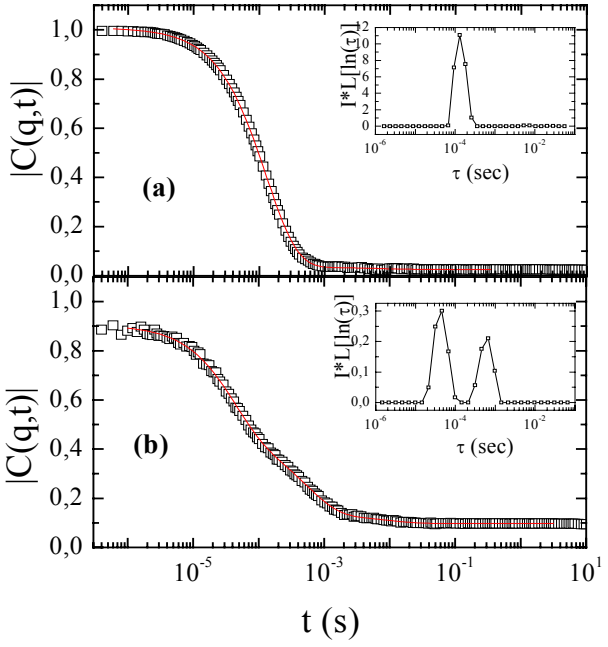

Figure 2.6 Correlation function of a 0.1 wt% PHEGMA-*b*-PDEAEMA copolymer solution at 90º scattering angle and (a) pH 6 and (b) pH 10. The inset shows the relaxation time distributions multiplied by the normalized intensity. Red lines on the correlation functions are the CONTIN fits to the correlation function.

CONTIN gives us more than one solutions for the relaxation time distribution. The chosen solution is that giving the minimum number of peaks and that with the best fit for C*(q,t)*. After choosing the best solution of CONTIN, each process was fitted with a Gaussian function with the aid of Origin 7.0 graph and analysis software as shown in **Figure 2.7**. The parameters of the fit are shown in the inset where x_c is the relaxation time and A is the area of each process at the specific angle. The area of each peak multiplied by the normalized scattered intensity calculates the intensity of each process from the equation:

$$I(\theta) = \frac{\bar{I}(\theta)}{I_{tol}(\theta)} \cdot \frac{A}{f^*} \tag{2.15}$$

where f^* is the spatial coherence factor that had been mentioned above, $\bar{I}(\theta)$ is the mean intensity at θ angle, $I_{\tau o \lambda}(\theta)$ is the toluene intensity at θ angle and A is the area of the process.

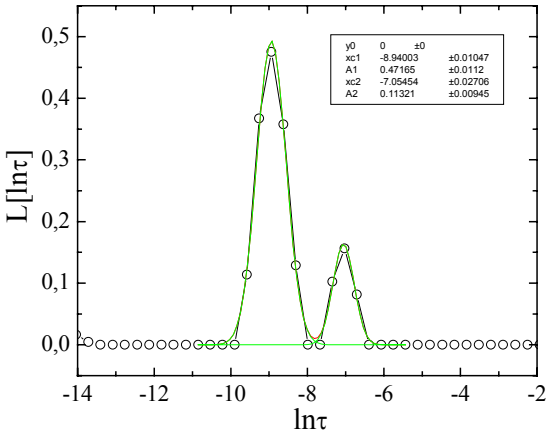

Figure 2.7 A characteristic inverse Laplace (–o–) and it's Gaussian fit (—). The inset shows the Gaussian fit results.

Calculated results for a characteristic sample, are shown in **Figure 2.8**. The intensity of the first process (□) is constant, while the second one (○) is depended to

the square of the wavelength (q^2). Such q^2-dependent processes can be fitted by Guinier's equation:

$$I(q) = I_o \cdot e^{-\frac{R_g^2 q^2}{3}} \tag{2.16}$$

where, Rg is the radius of gyration. The output of the Guinier fit is I_o (scattered intensity at q=0) and the radius of gyration R_g.

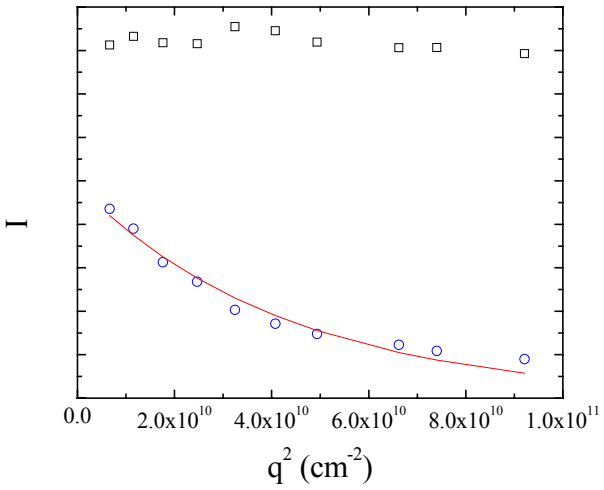

Figure 2.8 Scattered intensity of the fast (□) and the slow (○) process. The red line is the Guinier fit.

The rate for each angle is calculated from the equation:

$$\Gamma = \frac{1}{\tau} \tag{2.17}$$

where τ is calculated from the Gaussian fit of the inverse Laplace as mentioned above. A characteristic graph of Γ versus q^2 is shown in **Figure 2.9**.

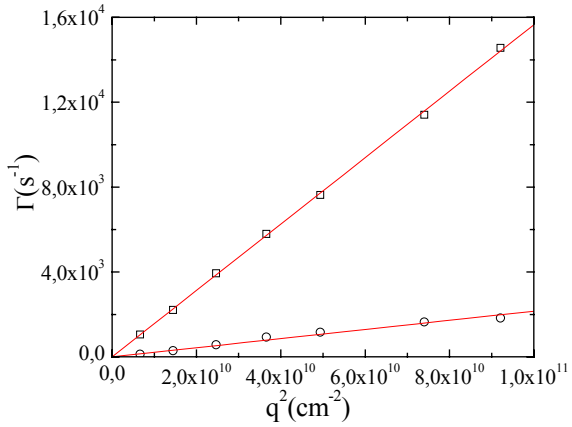

Figure 2.9 Rate of the fast (□) and the slow (○) process. The red lines are linear fits of the two rates.

The rate Γ is related to q^2 via the equation:

$$\Gamma = D \cdot q^2 \tag{2.18}$$

where D is the diffusion coefficient and is calculated from the slope of Γ vs q^2. The diffusion coefficient and the hydrodynamic radius R_h are related by the Stokes Einstein equation:

$$R_h = \frac{KT}{6\pi\eta D} \tag{2.19}$$

where η is the viscosity of the solvent, K is the Boltzmann constant and T is the temperature of the sample.

Another method to analyze the correlation function is the Kolhhrausch-Wiliams-Watts (KWW) function fit, which is described for one relaxation process as:

$$C(q,t) = \alpha \exp[-(t/\tau)^{\beta}] \tag{2.20}$$

and for two relaxation processes as:

$$C(q,t) = \alpha_1 \exp[-(t/\tau_1)^{\beta_1}] + \alpha_2 \exp[-(t/\tau_2)^{\beta_2}] \tag{2.21}$$

where β is the exponentiality parameter. For β=1 the relaxation is exponential and the relaxation time of the process is τ, while for β <1 or β >1 the relaxation time is calculated from the equation:

$$\tau(q) = \frac{\tau_{KWW}}{\beta}\Gamma(\frac{1}{\beta}) \qquad (2.22)$$

where Γ(x) is the Γ-function. From equations (2.22), (2.17), (2.18) and (2.19) the hydrodynamic radius R_h can be calculated.

A typical KWW fit is shown in **Figure 2.10**.

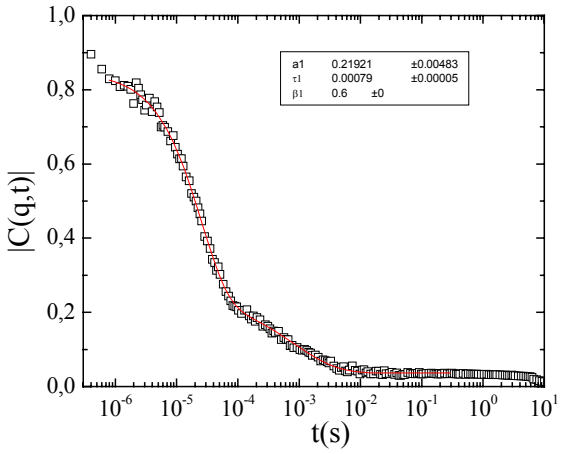

Figure 2.10 Characteristic correlation function (□) and the KWW fit (red line).

2.2.2 X-ray diffraction

X-ray diffraction has been used since the early part of this century for the investigation of crystalline materials and for the determination of their crystal structure. Crystals, regularly repeating structures, are capable of diffracting radiation with wavelengths similar to the interatomic separation of the order of 1Å. Diffraction is the result of interaction between X-rays and the electrons of atoms.

X-rays generation

X-rays are generated when an electron beam, provided by a heated Wolfram filament, is accelerated towards an anode by a potential difference of 30-50 kV and strikes the target, a piece of copper fixed at the anode. The anode is kept at a high vacuum chamber in order to avoid collisions between air particles and either the incident electrons or the emitted X-ray photons. The X-rays leave the chamber through windows made of beryllium. The absorption of X-rays which pass through different materials depends strongly on the atomic weight of the elements present in the material. Beryllium is, therefore, one of the most suitable window materials, since it does not scatter or absorb X-Ray photons. While the X-ray generator is in operation, continuous cooling of the anode is necessary because only a small fraction of the energy of the incident electron beam is converted into X-ray photons while most of the energy is converted into heat and the anode would therefore melt if it was not cooled.

X-ray spectrum

The X-ray diffraction spectrum of an element has two main features; the intense monochromatic peaks and the background noise [6].

X-rays are produced when accelerated electrons, collide with matter. These electrons are slowed down or stopped by the collision and some of their lost energy is converted into electromagnetic radiation. Such processes give white (polychromatic) radiation, X-rays which have wavelengths ranging above a certain lower limiting value. This lower wavelength limit corresponding to high energy X-rays occurs when all the kinetic energy of the incident particles is converted into X-rays. It can be calculated from the formula:

$$\lambda_{\min} = \frac{hc}{eV} = \frac{12400}{v} \tag{2.23}$$

where V is the accelerating voltage and eV is the electron kinetic energy.

When the voltage used to accelerate the electrons is sufficiently high (excitation voltage), X-ray spectrum is defined by some intense peaks that are characteristic of the metal target. In this case, the incident electrons have sufficient

energy to ionize some of the metal target 1s (k shell) electrons. An electron in an outer orbital (2p or 3p) immediately drops down to occupy the vacant at 1s level and the energy released during this transition appears as X-radiation. The transition energies have quantum values and thus a spectrum of characteristic X-rays results. The 2p→1s transition is known as K_α radiation and the 3p→1s transition is called K_β radiation. In fact, the K_α transition is a doublet because it has a slightly different energy for the two possible spin values of the 2p electron.

Bragg's Law

The Bragg's approach concerning diffraction assumes that crystals consist of layers or planes that interact with radiation like semi-transparent mirrors. Some of the X-rays are reflected off a plane with the angle of reflection equal to the angle of incidence, and the rest penetrate, to be subsequently reflected by sequential planes.

The equation of Bragg's Law is shown in **Figure 2.11**. Two X-ray beams, 1 and 2, are reflected from adjacent planes within the crystal and we wish to know under what conditions the reflected beams 1′ and 2′ are in phase.

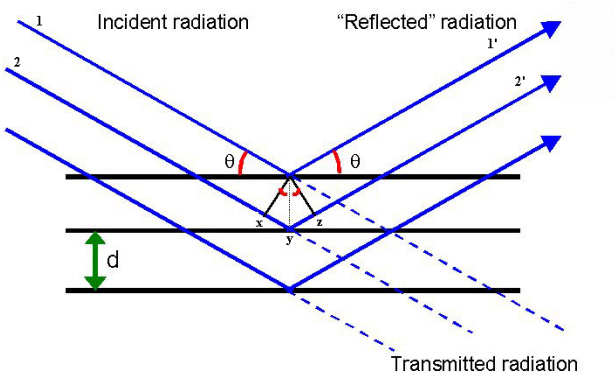

Figure 2.11 Bragg's law. Reflection from adjacent planes within the crystal.

Beam 22′ has to travel the extra distance xyz as compared to beam 11′, and for 1′and 2′ to be in phase, distance xyz must equal a whole number of wavelengths. The perpendicular distance between pairs of adjacent planes, the d-spacing, d, and the angle of incidence, or Bragg angle, θ, are related to the distance xy by

$$xy = yz = d \sin\theta$$

Thus

$$xyz = 2d \sin\theta$$

But

$$xyz = n\lambda$$

Therefore

$$2d \sin\theta = n\lambda \qquad \text{Bragg's Law} \qquad (2.24)$$

When Bragg's Law is satisfied, the reflected beams are in phase and interfere constructively. At angles of incidence other than the Bragg angle, reflected beams are out of phase and destructive interference or cancellation occurs.

For at least one reflection, i.e. the first-order reflection to occur, the condition called *resolution condition* is:

$$d \geq \frac{\lambda}{2} \qquad (2.25)$$

The wavelengths of X-rays are in the angström range and the resolution condition can be met for a number of lattice planes.

The wavelength and the Bragg angle θ may be varied experimentally. For the diffraction conditions to be met, only one of these parameters may be independently fixed. The choice of the variable parameter determines two groups of X-ray diffraction measuring methods:

θ fixed at a certain value, λ varying: Laue method

λ fixed at a certain value, θ varying: Rotation method (for single crystals)

Powder method (for polycrystalline materials), which is the method used in our measurements.

The powder method

The powder method has many important uses, especially in the area of crystallography. This method is used for the characterization of crystalline materials and for the determination of their crystal structures [7].

A monochromatic beam of X-rays strikes a finely powdered (or solid) sample that has crystals randomly arranged in every possible orientation. In such a powder

sample, the various lattice planes are also present in every possible orientation. For each set of planes, therefore, at least some crystals must be oriented at the Bragg angle, θ, to the incident beam and thus, diffraction occurs for these crystals and planes.

For any set of lattice planes, the diffracted radiation forms the surface of a cone, as shown in **Figure 2.12**. If the Bragg angle is θ, then the angle between diffracted and undiffracted beams is 2θ and the angle of the cone is 4θ. Each set of planes gives its own cone of radiation. The cones are detected by a thin strip of film. Each cone intersects the film as two short arcs and in a well powdered sample, each arc appears as a continuous line.

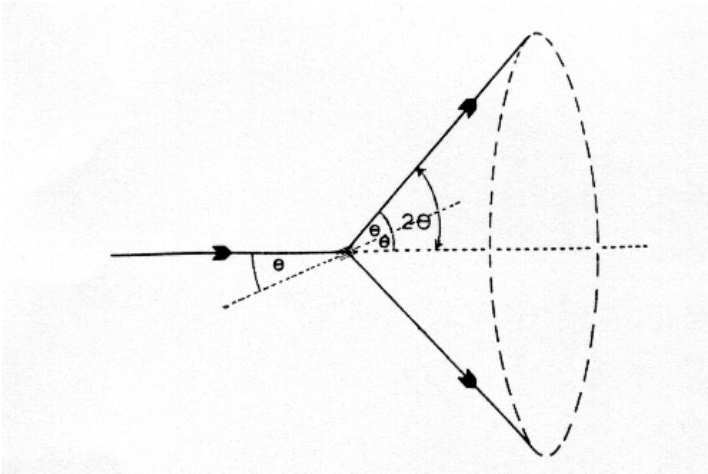

Figure 2.12 The formation of a cone of diffracted radiation in the powder method.

The angles of the diffraction cones are determined solely by the respective interplanar spacings. X-rays reflections on sets of lattice planes with equal interplanar spacings therefore contribute to the intensity diffracted into one diffraction cone.

Grain size

The size of the individual crystals in a polycrystalline sample is important information related to crystal growth conditions and to the mechanical properties of the material. The powder diffraction method provides a simple way of measuring the mean grain size of a specimen [7].

According to the *Laue-Scherrer* relation, the mean diameter t of the particles is:

$$t = \frac{0.9\lambda}{B\cos\theta} \tag{2.26}$$

where λ is the X-ray wavelength, θ the Bragg angle and B the Bragg peak width at half the peak height (FWHM). B is obtained from the Warren formula

$$B^2 = B_M^2 - B_S^2 \tag{2.27}$$

where B_M is the measured peak width in radians at half peak height and B_S is the corresponding width of a peak of a standard material, mixed in with the sample, whose particle size is considerably greater than 2000Å and which has a diffraction peak near to the relevant peak of the sample.

X-Ray Diffractometer

The X-Ray diffractometer used in this study consists of a Rigaku 12kW rotating anode X-Ray generator and a Rigaku RINT 2000 Series wide angle diffractometer equipped with a Thin Film Attachment (**Figure 2.13**).

The beam from the X-Ray generator is collimated with the divergence slit DS (1/2 deg, located 10cm away from the focus point) and it passes through a height limit slit HLS (8mm) before it impinges upon the sample surface, where it is diffracted. After passing a Soller Slit (divergence angle 0.34º) a curved graphite monochromator was used to deliver X-Rays of wavelength λ=1.54Å and finally the diffracted beam is measured by a scintillation counter. A receiving slit RS (width 0.3mm) and a scattering slit SS (1/2 deg.), attached to the Soller Slit are used in order to suppress the off-specular scattering from the sample. Another receiving slit, RSm (width 0.8mm) is used after the monochromator. The goniometer radius is 185mm.

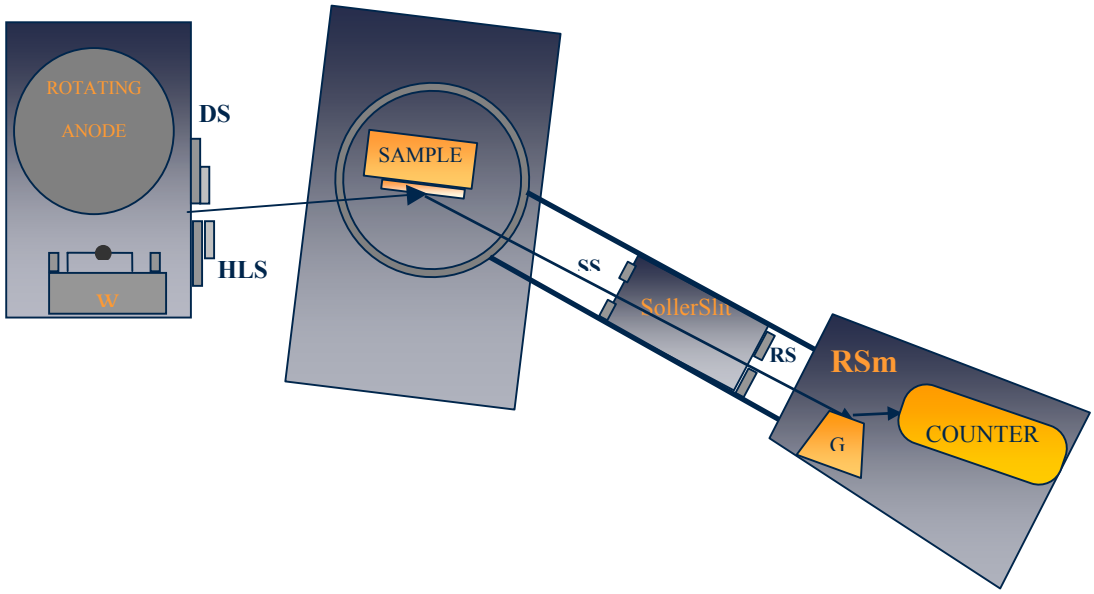

Figure 2.13: X-Ray Diffractometer: DS = divergence slit (1/2 deg) , HLS = Hight Limit Slit (8mm), SS = scattering slit (1/2 deg), Soller slit (Divergence 0.34º), RS=Receiving slit (0.3mm width), G =Monochromator Graphite Crystal, RSm =Monochromator Receiving Slit (0.8mm width).

Diffraction spectra are obtained by rotating the sample by an angle θ and the detector by an angle 2θ with respect to the X-Ray beam while maintaining the scattering vector normal to the surface.

2.2.3 Nuclear magnetic resonance spectroscopy

Nuclear magnetic resonance (NMR) spectroscopy gives information about the neighborhood of the nuclei of the atoms that form a molecular compound. An enormous amount of information can be derived from a single spectrum, and in many cases this facilitates the determination of the chemical structure of a molecule.

The fundamental property of the atomic nucleus involved in this technique is the nuclear spin (I), which takes either even or odd values. A nucleus with nuclear spin I adopts 2I+1 nondegenerate spin orientations in a magnetic field. The energy of

the i^{th} spin state (E_i) is directly proportional to the nucleus spin m_i and the magnetic field strength B_0:

$$E_i = -m_i \frac{\gamma \hbar B_0}{2\pi} \tag{2.28}$$

In this equation h is Planck's constant, while γ is called the magnetogyric ratio, a proportionality constant characteristic of the isotope being examined [8].

The selection rule for the NMR transitions is that m_i can only change by one unit. Thus, the transition energy is given by:

$$\Delta E = \frac{\gamma \hbar B_0}{2\pi} \tag{2.29}$$

Transition from the lower to the upper state is possible by absorption of radiation of the appropriate frequency. This radiation is in the radiofrequency region of the electromagnetic spectrum and its precise frequency can be calculated using the formula:

$$\nu = \frac{\gamma B_0}{2\pi} \tag{2.30}$$

In an NMR experiment either the field B_0 or the frequency ν can be varied.

Theory of chemical shifts

A bare proton nucleous precess at much higher frequency than a proton nucleus surrounded by electrons [8]. The electron cloud surrounding each nucleus in a molecule serves to shield that nucleus from the external magnetic field.

The external magnetic field B_0 causes each electron pair surrounding the nucleus to circulate through its orbital in such a way as to generate an induced magnetic field (B_i) that opposes to the external field. Thus, while a bare proton experiences the full magnitude of the external field, the shielded nucleus experiences an effective field (B_{eff}) that is equal to the external field minus the induced field:

$$B_{eff} = B_0 - B_i \tag{2.31}$$

Because the strength of the induced field is directly proportional to that of the external field, we can define a shielding constant σ that is a function of the exact molecular environment of the nucleus:

$$B_i = \sigma B_0 \tag{2.32}$$

Using equation (2.32), equation (2.31) can be written in the form:

$$B_{eff} = (1-\sigma)\, B_0 \tag{2.33}$$

Substituting this result into equation (2.30) gives:

$$\nu = \frac{\gamma(1-\sigma)B_0}{2\pi} \tag{2.34}$$

Thus, the greater the shielding of the nucleus, the lower is its resonance frequency and the farther to the right it will appear in an NMR spectrum. Conversely, nuclei from which electron density has been withdrawn are said to be deshielded and appear toward the left of the spectrum.

The chemical shift scale

It is virtually impossible to measure absolute frequencies with the high degree of precision necessary in NMR, but it is possible to measure frequency differences very precisely. This is the reason why NMR signal frequencies are measured as the difference ($\Delta\nu_i$) between the precession frequency and the instrument's operating frequency:

$$\Delta\nu_i = \nu_i - \nu_0 \tag{2.35}$$

In order to device a reproducible scale for the frequency axis of an NMR spectrum, we add in each sample a small amount of a standard internal reference compound that gives rise to a sharp signal somewhat apart from the other signals of interest. We arbitrarily assign the reference signal the frequency value zero and measure frequency differences in hertz downfield or upfield of the reference signal. As a result, the signal position is given by:

$$\delta\nu_i = \Delta\nu_i - \Delta\nu_{ref} \quad (2.36)$$

Another problem is that the spectroscopic data, when expressed as δν, will vary from one spectrometer to another if their operation frequency is different. This is because precessional frequencies, and their differences, are directly proportional to the field strength. In order to solve this problem, we define a new quantity called the chemical shift of nucleus i (δ_i) by the equation:

$$\delta_i = \frac{10^6(\Delta\nu_i - \Delta\nu_{ref})}{\nu_0} \quad (2.37)$$

δ scale normalizes the frequency differences over the operating frequency. δ is expressed at part per million (ppm).

Spectrometer

The basic requirement for all high-resolution NMR spectrometers is a radiofrequency (RF) source and a magnetic field, both of which must be characterized by very high stability and homogeneity. The sample is placed in a probe, which is positioned between the poles of the magnet as shown in **figure 2.14.**

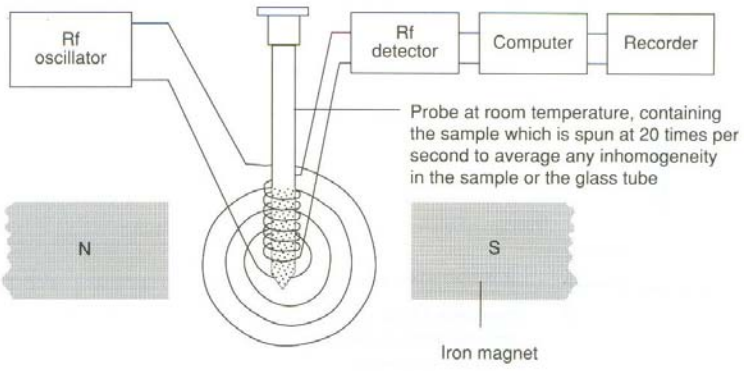

Figure 2.14 NMR spectrometer.

Either the magnetic field or the RF frequency is slowly varied. A radiofrequency detector is set at right angles to the radiofrequency transmitter inducing resonance, and a recorder charts the absorption of energy as a function of the applied field or frequency.

Good resolution is achieved by rotating the sample about its axis using an air jet in the probe. This averages the magnetic field experienced by each part of the sample about the spinning axis, thus producing much increased resolution of the measurement.

2.2.4 Ultraviolet/visible spectroscopy

When light is absorbed by a material, valence electrons are promoted from their ground state to higher energy states. This promotion can occur either in the visible part of the spectrum or in the ultraviolet region. Visible light lies in the wavelength range 400-700 nm, while ultraviolet light lies in the range 190-400 nm. The exact energy differences between the orbitals depends on the atoms present and the nature of the bonding system.

Absorption laws

According to Beer's law the absorption is proportional to the concentration of absorbing molecules (this is only true for dilute solutions) while Lambert's law define that the fraction of radiation absorbed is independent of the intensity of the radiation [8]. Combining these two laws, we can derive the Beer-Lambert law:

$$\log_{10} \frac{I_0}{I} = \varepsilon l c \tag{2.38}$$

where: I_0 = the intensity of the incident radiation

I = the intensity of the transmitted radiation

ε = a constant characteristic for each absorbing material, known as the molar absorption coefficient measured as $mol^{-1}\ dm^3\ cm^{-1}$, but by convention the units are not quoted

l = the sample path length in cm

c = the concentration of the absorbing species in mol dm^{-3}

The value of $\log_{10}(I_0/I)$ is known as the absorbance of the solution and can be read directly from the spectrum, often in 'arbitary' absorbance units.

Absorption curves

The energy of the orbitals involved in electronic transitions have fixed values, and since energy is quantized, one would expect that absorption peaks in ultraviolet/visible spectroscopy would be sharp. However, this is rarely true. Instead, broad absorption peaks are often obtained. This is because a number of vibrational energy levels are available at each electronic energy level, and thus transitions can occur to and from the different vibrational levels. These transitions result in peak broadening. The situation is further complicated by the fact that different rotational energy levels are also available in absorbing materials.

The spectrometer

In conventional spectrometers electromagnetic radiation passes through the sample which is held in a small square-section cell **(Figure 2.15)**. Radiation across the whole ultraviolet/visible range is scanned over a period of approximately 30 s, which passes both through the sample cell and a reference cell containing only the solvent. Photocells then detect the radiation transmitted and the spectrometer records the absorption by comparing the difference between the intensity of the radiation passing through the sample and the reference cells.

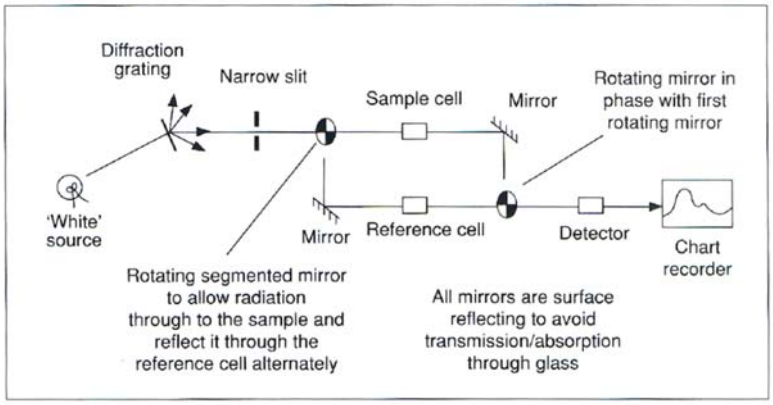

Figure 2.15 The ultraviolet/visible spectrometer.

No single lamp provides radiation across the whole range required, thus two lamps are used. A hydrogen or deuterium discharge lamp which covers the ultraviolet range, and a tungsten filament which covers the visible range. The radiation is separated to its different wavelength components by a diffraction grating followed by a narrow slit. The slit ensures that the radiation is monochromatic.

The cells used in the ultraviolet range must be made of pure silica because soda glass absorbs below 365 nm, and pyrex glass below 320 nm.

Detection of the radiation transmitted through the sample and reference cell is achieved by either a photomultiplier or a photodiode, that converts photons of radiation into electrical currents. The spectrum is produced by comparing the currents generated by the sample and the reference beams.

2.2.5 Transmission Electron Microscopy

Transmission electron microscopy (TEM) allows the visualization of the internal structure of specimens using transmitted electrons. A beam of highly focused electrons are directed toward a thinned sample. These highly energetic incident electrons interact with the atoms in the sample and produce characteristic radiation that is used in material characterization [8].

Like all matter, electrons have both wave and particle properties. The expression that relates the motion of the electrons and their wavelength is:

$$\lambda = \frac{h}{mv} \tag{2.39}$$

where:

(h) Planck's constant

(m) electron mass

(v) electron velocity

Electrons are charged particles that can be accelerated by the application of an electrostatic field. Their velocity depends on the field and can be calculated by the expression:

$$\frac{mv^2}{2} = eV \tag{2.40}$$

where:

(e) electron charge

(V) the accelerating voltage

Combining the above expressions, and substituting with the relative constants the following expression is obtained:

$$\lambda(A) = \frac{12{,}3}{\sqrt{V(v)}} \tag{2.41}$$

From this last expression, it is obvious that the wavelength can be tuned by adjusting the accelerating field, and can be much smaller than that of light. Thus, microscopy using electrons offers a much greater resolving power than optical microscopy.

Transmission electron microscopy gives information about the size, shape, and distribution of the phases that consist the material. It also gives the distribution of the material elements, including segregation if present. It shows the crystal structure of the phases and the character of the crystal defects. However, it does have some limitations. Images of living systems cannot be obtained, and the preparation of a specimen can be complicated and expensive.

The microscope

The incident electrons are usually generated by passing an electric current through a tungsten filament at the top of a column. A voltage, usually in the range 80-200 kV, is applied between the electron source (the cathode) and the rest of the column (the anode). This voltage accelerates the electrons down the column, towards the specimen (**figure 2.16)**. High potentials are necessary in order to give the electrons sufficient energy to penetrate the specimen.

Electromagnetic condenser coils collimate the beam, which then strikes the specimen. The specimen must be dry, solid, stable, and capable of withstanding the heating effect of the electron beam. It must also be extremely thin and transparent to the beam.

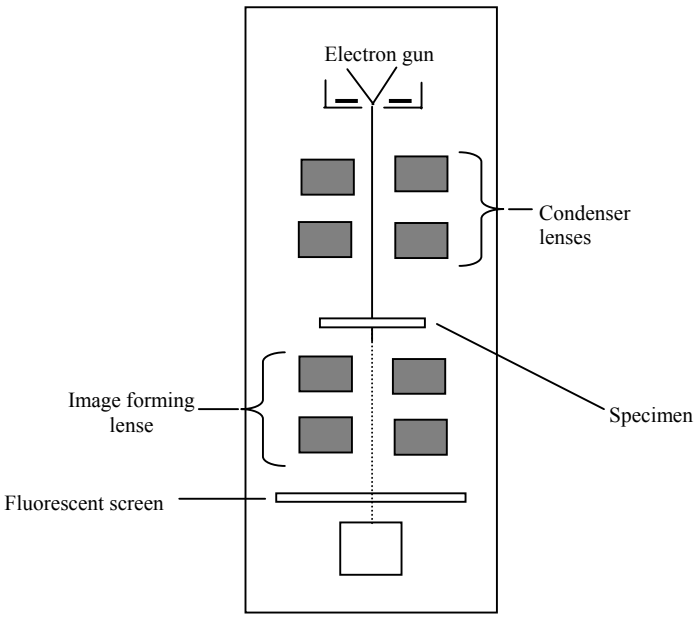

Figure 2.16 The transmission electron microscope (TEM).

Once the electron beam passes through the specimen it is magnified and focused by an image forming electromagnetic lens. It then strikes a fluorescent screen where the energy of the electrons is converted to visible light, and the image is formed. Alternatively, the screen can be replaced by a camera so that a photographic image is recorded.

2.3 Sample preparation

2.3.1 General

All copolymers were dried in a vacuum oven for half an hour prior to use in order to remove any trace of moisture. Dilute solutions of the polymers were prepared in pre-filtered nanopure water (filter pore size: 0.2 μm) titrated to pH 2 (or α=2) using 12 M HCl. The appropriate amount of polymer was added in the low pH water and the samples were left stirring overnight to ensure complete polymer dissolution.

Finally, the pH (or α) of all samples was adjusted to the required value by the addition of 0.1 M NaOH and was allowed to stir for another 12h.

In order to obtain the desirable α value, the amount of the associated acid or base was calculated from the ratio:

$$\frac{[mole\ acid\ /\ base]}{[mole\ a\min e\ group]} = \frac{\alpha}{1},$$

assuming that all of the H^+ from the added acid protonate the amine groups.

For the microgel particles, the initial concentrated latex dispersion (0.92 wt%) was first diluted to the required concentration with pre-filtered nanopure water. Next the solution pH was adjusted to the appropriate value by adding either 0.1 M HCl or 0.1 M NaOH and the solution was allowed to stir overnight to ensure equilibrium swelling.

2.3.2 Metal incorporation and metal nanoparticle formation

Two different procedures were used for the introduction of the metal compounds within the polymer micelles.

In the first method the appropriate amount of diblock copolymer to obtain a 0.33 wt% polymer solution was dissolved in water at pH 2. The sample was stirred overnight to ensure complete polymer dissolution. Next the metal precursor (H_2PtCl_6 or K_2PtCl_6) was added to the molecular polymer solution at N/Pt=3/1 molar ratio. The solution was stirred for 24 h to allow metal complexation to occur. The metal precursor can be present both inside and outside the micelles due to its solubility in water. The excess of ionic species was removed by ultrafiltration using an Amicon® Stirred Ultrafiltration Cell by Millipore with regenerated cellulose ultrafiltration membranes, NMWL: 3000. Reduction of the sample was carried out using a 3-fold excess of sodium borohydride ($NaBH_4$) and the pH was increased to 10 with the addition of NaOH (0.1 M). The reduced sample was left stirring overnight.

The second method involved the molecular dissolution of the copolymer under stirring overnight in water at pH 2. Then the pH was raised to 10 using NaOH (0.1 M)

to form the polymeric micelles. After stirring overnight the metal precursor was added to the micellar solution at N/Pt=3/1 molar ratio. The solution was stirred for 24 h to allow metal for complexation to occur, followed by ultrafiltration. Metal reduction was carried out using a 3-fold excess of sodium borohydride.

Two different methodologies were also employed for the introduction of the metal compounds within the microgel particles.

In the first method the initial concentrated latex dispersion was first diluted to 0.05 wt% concentration by adding the appropriate amount of water at pH 2. The sample was stirred overnight to ensure total protonation of the tertiary amines and H_2PtCl_6 was added next to the swollen particles at N/Pt=3/1 molar ratio. The solution was stirred for 24 h to allow for metal complexation to occur, followed by ultrafiltration. Reduction of the sample was carried out and the pH was increased to 10 with the addition of NaOH (0.1 M). The sample was left stirring overnight.

In the second method, water without any previous adjustment of the pH was added in order to obtain a 0.05 wt% latex dispersion. After stirring overnight the metal precursor (H_2PtCl_6) was added to the sample followed by ultrafiltration and metal reduction as described above.

2.3.3 Dynamic light scattering (DLS)

Samples for DLS were prepared following a procedure similar to that described above. All samples were filtered and allowed to equilibrate for an hour before being measured. The pore size of the filters used for the diblock copolymers solutions was 0.45 μm while filters with pore size 1.2 μm and 3 μm were used for the microgel particles at high and low pH respectively. An ALV spectrophotometer and an Nd-YAG laser with λ=532 nm was used, while all measurements were performed at 20 ºC.

2.3.4 X-ray diffraction (XRD)

Samples for XRD were prepared as described in section 2.3.1. All samples used in the XRD experiments were previously dried under vacuum at room temperature to remove the solvent. A Rigaku RINT 2000 Series wide angle diffractometer was used. Measurements were made from θ=2º to θ=110º in steps θ = 0.006º and the operating conditions in all measurements performed were Current = 40mA and Voltage = 178kV.

2.3.5 ^{1}H NMR spectroscopy

For the ^{1}H NMR experiments deuterium oxide (D_2O) 99.9% was used. The deuterated water was titrated to pH = 2 (or α = 2) by the addition of deuterium chloride (DCl) 35 wt% solution in D_2O. The diblock copolymer was then added at a 2 wt% concentration and the solution was left stirring overnight. Finally, the pH (or α) of the samples was adjusted to the required value by the addition of sodium deuteroxide 40 wt% solution in D_2O. Samples were allowed to stir for one day in order to equilibrate before being placed in NMR tubes and measured. For the experiments a Bruker AMX-500 spectrometer was used.

2.3.6 Ultraviolet/Visible spectroscopy (UV/Vis)

All samples were prepared as described above. Dilutions to the required polymer concentration were performed using water titrated to the pH of the sample. They were then placed in a 1cm quartz cell. UV/Vis absorption spectra in the range 190-1100 nm were recorded on a Perkin Elmer Lambda 45 spectrometer.

2.3.7 Transmission electron microscopy (TEM)

Samples for TEM were prepared following a procedure similar to that described for the DLS experiments. All samples were previously diluted with water adjusted to the appropriate pH. A drop of the diluted sample was then placed on a carbon-coated copper grid and left to dry in air overnight. A JEOL JEM-100C

instrument at an electron accelerating voltage of 80kV was employed for the measurements.

2.4 References

[1] M. Vamvakaki, L. Papoutsakis, V. Katsamanis, T. Afchoudia, P. G. Fragouli, H. Iatrou, N. Hadjichristidis, S. P. Armes, S. Sidorov, D. Zhirov, V. Zhirov, M. Kostylev, L. Bronstein and S. H. Anastasiadis *Faraday Discuss.*, 2005, **128**, 129-147.

[2] J. I. Amalvy, E. J. Wanless, Y. Li, V. Michailidou, S. P. Armes, Y. Duccini *Langmuir*, 2004, **20**, 8992-8999.

[3] B. Berne, R. Pecora, *Dynamic Light Scattering*, Willey Interscience Publications, New York.

[4] M. Doi, S. F. Edwards, *The theory of polymer dynamics*, Science Publications, Oxford.

[5] ALV-5000, Multiple Tau, Digital Correlator. User's Reference Manual.

[6] J. P. Eberhart, *Structural and chemical analysis of materials*, Willey Publications, Sussex.

[7] R. Jenkins, R. L. Snyder in Indroduction to X-ray Powder Diffractometry, John Wiley & Sons, Inc., 1996.

[8] B. Faust, *Modern Chemical Techniques*, Education Division, The Royal Society of Chemistry, London.

Chapter 3

3.1 Responsive diblock copolymers

3.1.1 Degree of protonation

The aqueous solution properties of PHEGMA-*b*-PDEAEMA diblock copolymers are investigated. At low pH the copolymer is in its unimer state due to the hydrophilicity of the protonated DEAEMA units, while an increase of the solution pH above 7 results in the deprotonation of the amine groups, which become hydrophobic and lead to the formation of micelles. PDEAEMA form the micelle cores while the hydrophilic PHEGMA in the micelle corona stabilize them in solution. The hydrodynamic radius of these micelles formed above pH 7 was measured in previous studies by DLS and was found around 14 nm for copolymers with the PHEGMA block comprising fifty monomer units while the length of the DEAEMA block was varied systematically between 20 and 50.

However, the parameter that more accurately determines the formation of the micelles is not the pH, which is a property of the solution surrounding the polymer chains, but the degree of protonation (α) of the DEAEMA units, which is rather related to changes in the polymer structure, upon addition of acid or base [1]. Thus, in order to obtain a more detailed picture of the micellization process we examined the effect of α on the solution properties of the above diblock copolymers. In the present study the degree of protonation is defined as the fraction of the charged tertiary amine units of the diblock copolymers and takes values between zero and one. Assuming that all of the protons from the added HCl protonate the amine groups the degree of protonation is defined as the net moles of HCl added, divided by the moles of the amine units in solution. This is expressed as:

$$\alpha = \frac{[net\ HCl]}{[DEAEMA]} \qquad 0 \le \alpha \le 1$$

3.1.2 Effect of α on the copolymer solution properties

The polymer characteristics in a $PHEGMA_{50}$-*b*-$PDEAEMA_{50}$ copolymer solution as a function of the degree of protonation of the PDEAEMA block was initially studied by DLS.

Figure 3.1 illustrates the intensity autocorrelation functions C(q,t) of a 0.1 wt% $PHEGMA_{50}$-*b*-$PDEAEMA_{50}$ diblock copolymer solution at scattering angle 90º for three different degrees of protonation α = 0.6, 0.1 and 0.0. The corresponding inverse laplace transformations are also shown in the inset.

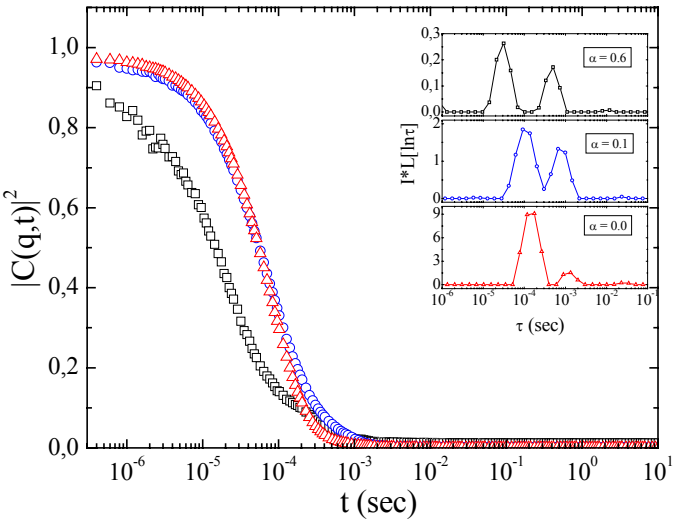

Figure 3.1 Intensity autocorrelation functions C(q,t) of a 0.1 wt% $PHEGMA_{50}$-*b*-$PDEAEMA_{50}$ solution at scattering angle θ = 90º and α=0.6 (□), α=0.1 (○) and α=0.0 (△). Inset: distributions of relaxation times multiplied by the total scattering intensities (normalized to that of toluene) for the respective degrees of protonation.

At α = 0.6 two processes with low intensity are observed. The fast process with a diffusivity $D_1 = 6.74 \times 10^{-7}$ cm^2/s which corresponds to a hydrodynamic radius $R_{h,1}$ = (3.2 ± 0.2) nm is attributed to the single polymer chains and the second slow process with diffusivity $D_2 = 3.76 \times 10^{-8}$ cm^2/s which corresponds to $R_{h,2}$ = (57 ± 2) nm is attributed to a few polymer aggregates. For α = 0.1 a sharp increase in the scattered

intensity is obtained while two processes are again identified with $D_1 = 1.87x10^{-7}$ cm^2/s and $D_2 = 2.73x10^{-8}$ cm^2/s corresponding to hydrodynamic radii $R_{h,1} = (11.4 \pm 0.5)$ nm and $R_{h,2} = (78 \pm 2)$ nm respectively and which are attributed to the diffusion of polymer micelles and micellar aggregates. Two processes of high intensity are consistently obtained for $\alpha = 0.0$ with corresponding diffusivities $D_1 = 1.43x10^{-7}$ cm^2/s and $D_2 = 1.57x10^{-8}$ cm^2/s and hydrodynamic radii $R_{h,1} = (15.0 \pm 0.5)$ nm and $R_{h,2} = (137 \pm 2)$ nm respectively attributed to the equilibrium polymer micelles and the micellar aggregates obtained in previous studies at high pH [2].

Figure 3.2a illustrates the intensity of the scattered light versus the degree of protonation of the DEAEMA units for a 0.1 wt% aqueous solution of the $PHEGMA_{50}$-*b*-$PDEAEMA_{50}$ diblock copolymer, while **Figure 3.2b** illustrates the hydrodynamic sizes found for the corresponding degrees of protonation.

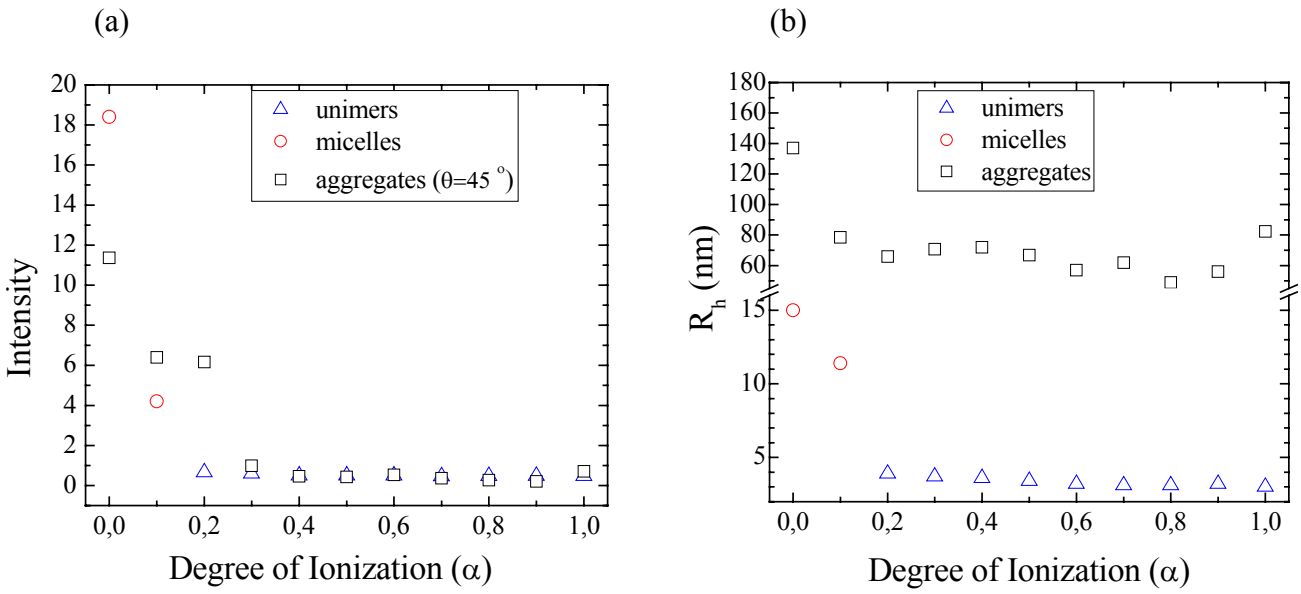

Figure 3.2 Intensity of the scattered light (normalized to that of toluene) versus the degree of protonation of the DEAEMA units for a 0.1 wt% $PHEGMA_{50}$-*b*-$PDEAEMA_{50}$ solution (a) and hydrodynamic sizes calculated for the corresponding degrees of protonation of the DEAEMA groups (b).

It can be easily observed that for $0.2 < \alpha < 1$ two processes of low intensity are obtained. The fast process is attributed to the diffusion of single copolymer chains with hydrodynamic radius $R_h \sim 4$ nm and a q^2-independent intensity ~ 0.5 while a

slower process is also obtained attributed to the diffusion of polymer aggregates with an R_h ~ 70 nm and a very low q^2-dependent intensity I (45º) ~ 0.5. The contrast and, thus, the scattering intensity of the peak related to the aggregates remains relatively low, suggesting that they are either very few in number or highly hydrated, due to the high degree of protonation of the DEAEMA units. The formation of these aggregates is attributed to the polyelectrolyte effect and will be discussed later. For $\alpha = 0.2$ while the intensity and the size of the unimers remains constant, the scattered intensity due to the aggregates increases, while their size is similar to that obtained at higher values of α, suggesting either an increase of their number or an increase of their contrast; this is because the fraction of deprotonated DEAEMA units has increased and so do the hydrophobic interactions of the polymer chains leading to an increase in polymer aggregation. For $\alpha = 0.1$ a sharp increase of the scattered intensity is observed, accompanied by a great increase of the hydrodynamic size of the fast process to an R_h = 11 nm. This latter process is attributed to the diffusion of polymer micelles which are thus formed at $\alpha = 0.1$. It is worth noting that both the size and the scattered intensity of the aggregates remain almost constant from $\alpha = 0.2$ to $\alpha = 0.1$. Finally, for $\alpha = 0.0$ an increase of the micelle size and intensity is identified which reaches the equilibrium values obtained in previous experiments at high pH (> 7). An increase of the hydrodynamic radius and the intensity of the slow process are also observed, attributed to the formation of a few micellar aggregates. These micellar aggregates are attributed to a non-effective steric stabilization conferred by the short hydrophilic PHEGMA blocks that form the micelle corona.

The solution behavior of the $PHEGMA_{50}$-*b*-$PDEAEMA_{50}$ diblock copolymer as a function of the degree of protonation, α, was also studied by ^{1}H NMR in D_2O/DCl and the results were compared to those obtained by DLS.

In previous studies, ^{1}H NMR spectroscopy has been used to investigate the solution properties of the PHEGMA-*b*-PDEAEMA diblock copolymers as a function of solution pH [3]. **Figure 3.3** shows the proton NMR spectra of the $PHEGMA_{50}$-*b*-$PDEAEMA_{34}$ diblock copolymer as a function of solution pH. Over the pH range from 2 to 7 all signals attributed to the protons of both blocks are visible suggesting that the copolymer is in its unimer state. For pH 10 the NMR signals at 1.4, 3.3-3.4, 3.6 and 4.4-4.5 ppm, attributed to the PDEAEMA block disappear completely,

indicating the formation of micelles with the PDEAEMA block forming the micelle core.

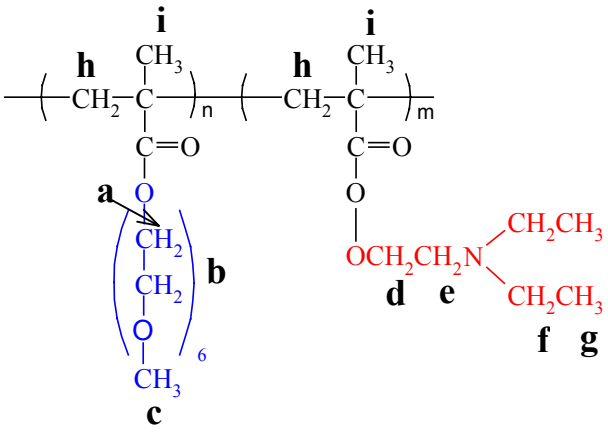

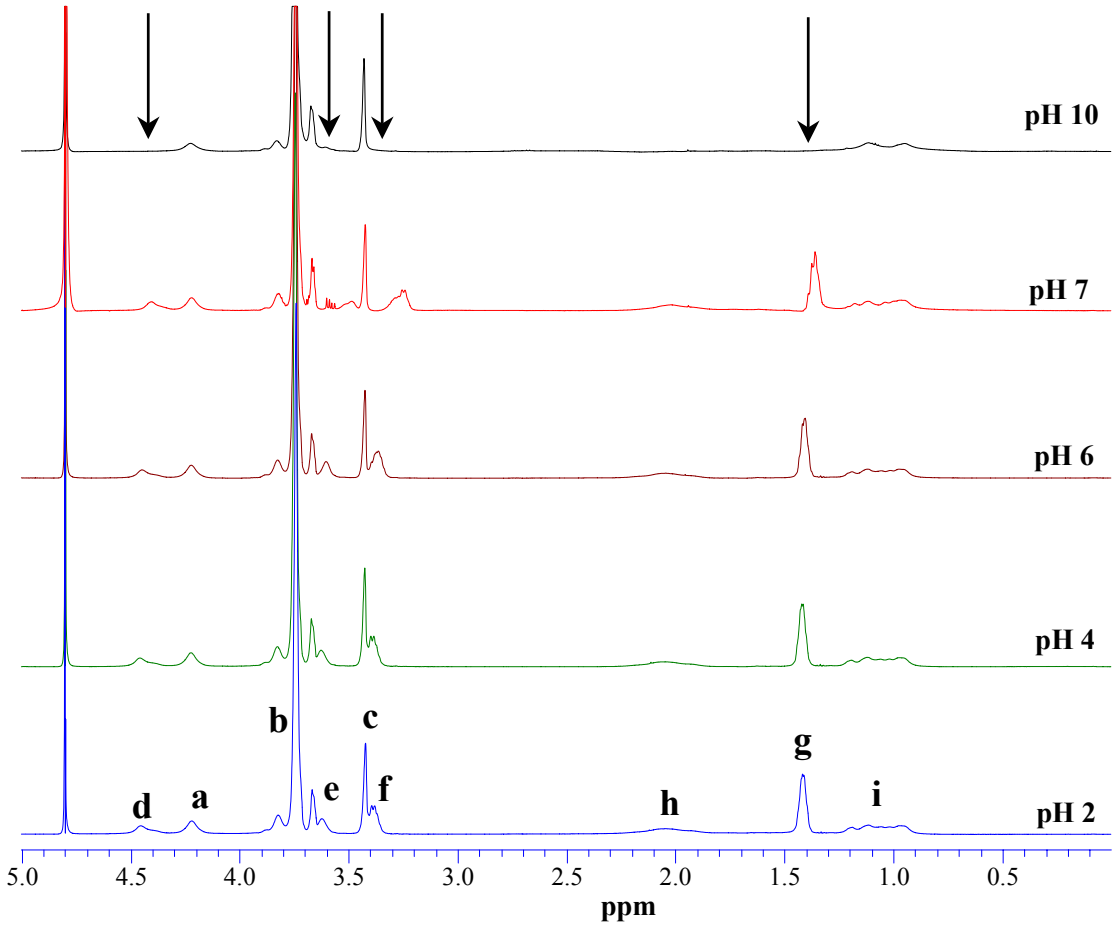

Figure 3.3 ^{1}H NMR spectra for 2 wt% PHEGMA$_{50}$-*b*-PDEAEMA$_{34}$ diblock copolymer solutions in D_2O/DCl and D_2O/NaOD for different pH values.

Further NMR studies focused in the pH range from 6.5 to 8 allowed a more detailed investigation of the critical pH region where the solution properties of the polymer chains are altered and structure formation is induced. The NMR spectra from pH 6.5 to pH 8.0 are shown in **Figure 3.4**. At pH 6.5 all signals of the protons attributed to DEAEMA units are visible. However, in the spectra at pH 7.0, 7.5 and 7.75 the signals at 1.4, 3.3-3.4, 3.6 and 4.4-4.5 ppm are gradually shifted to lower ppm due to the better shielding of the DEAEMA protons from the electron pair of the deprotonated nitrogen at high pH. At pH 8 the signals due to the protons of the PDEAEMA block disappear indicating the formation of the micelles as discussed above for the spectrum at pH 10.

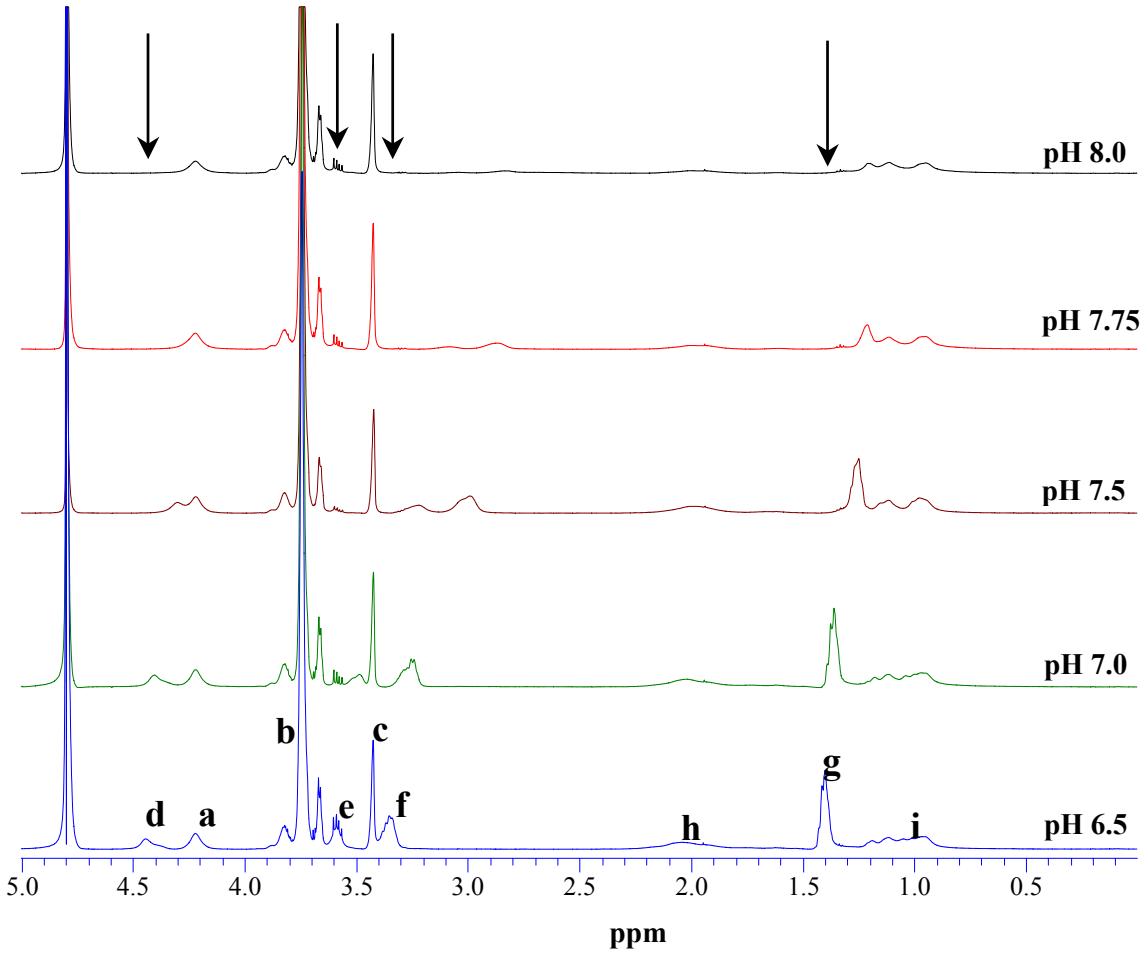

Figure 3.4 ^{1}H NMR spectra for 2 wt% $PHEGMA_{50}$-*b*-$PDEAEMA_{34}$ diblock copolymer solutions in D_2O/DCl and D_2O/NaOD for pH values between 6.5 and 8.0.

In the present study in order to obtain a more detailed picture of the micellization process as discussed above for the DLS study, and verify the shift of the peaks due to the DEAEMA units as the PDEAEMA block becomes deprotonated, we examined the effect of α on the solution properties of the $PHEGMA_{50}$-*b*-$PDEAEMA_{50}$ diblock copolymer. **Figure 3.5** shows the ^1H NMR spectra for 2 wt% $PHEGMA_{50}$-*b*-$PDEAEMA_{50}$ copolymer solutions for α values from 0.0 to 1.0, with a step of 0.1.

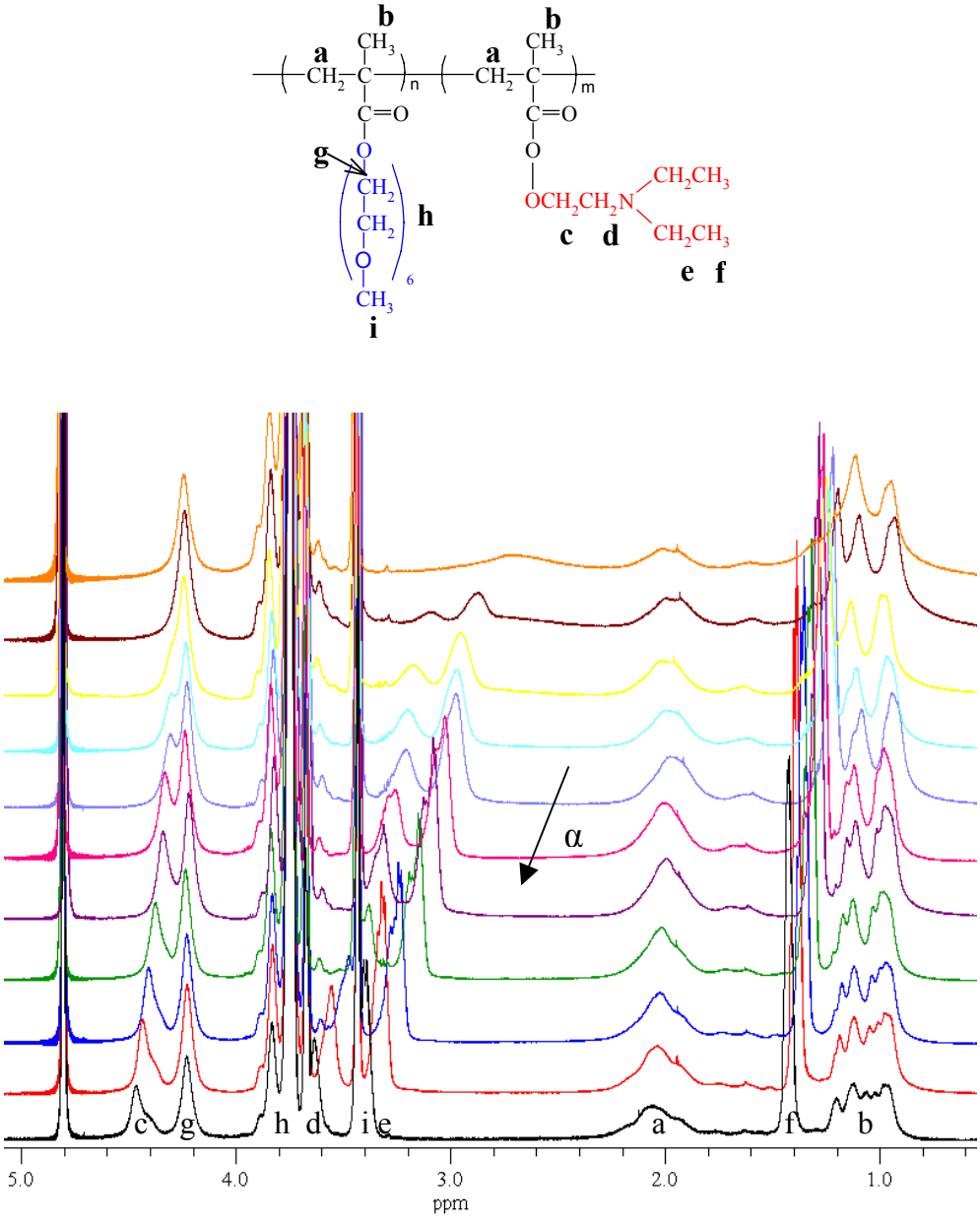

Figure 3.5 ^1H NMR spectra for 2 wt% $PHEGMA_{50}$-*b*- $PDEAEMA_{50}$ diblock copolymer solutions in D_2O/DCl versus the degree of protonation, α, of the DEAEMA units.

The signals observed at 1.4, 3.3-3.4, 3.6 and 4.4-4.5 ppm are due to the protons of the DEAEMA units, as discussed above, while signals at 3.4, 3.8 and 4.2 correspond to the protons of the HEGMA units. We observe a gradual shift of the peaks corresponding to the protons of the DEAEMA side groups to lower ppm as the DEAEMA units become deprotonated at lower α. This is attributed to the better shielding of the DEAEMA protons from the electron pair of the deprotonated nitrogen at low α, causing them to move upfield as discussed above. The disappearance of the PDEAEMA peaks at α = 0 is also observed which confirms the formation of micelles with the deprotonated PDEAEMA block forming the micelle core, while the well-solvated PHEGMA block comprises the micelle corona.

Figure 3.6 illustrates the quantitative results of the NMR experiments, where the % moles of DEAEMA units present in solution (calculated from the peak integrals in the above NMR spectra) are plotted as a function of α.

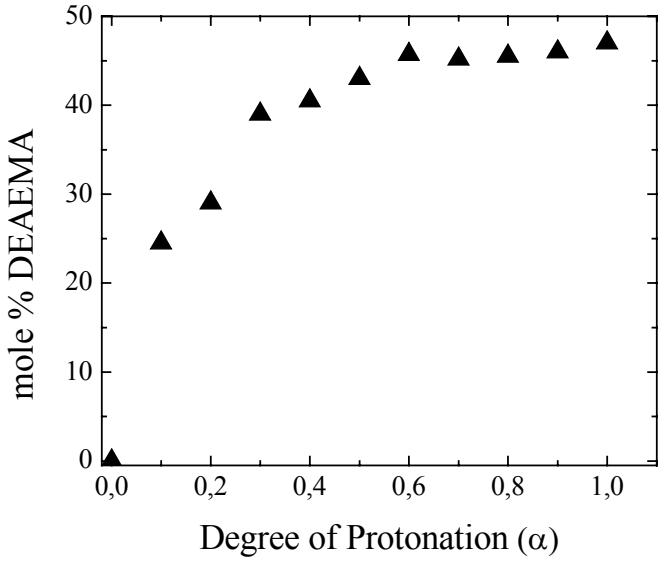

Figure 3.6 Moles % of PDEAEMA units in solution as a function of the degree of protonation α for $PHEGMA_{50}$-*b*-$PDEAEMA_{50}$.

A gradual decrease in the number of DEAEMA units that remain in solution is observed for α = 1.0 down to α = 0.3 while for α = 0.2 a rather sharp decrease of the moles of soluble DEAEMA is obtained. This decrease becomes even more abrupt below α = 0.1 which is in good aggrement with the formation of micelles at such low degrees of protonation, observed above by DLS.

The consistency between our DLS and ^{1}H NMR results as a function of the degree of protonation α of the PHEGMA$_{50}$-*b*-PDEAEMA$_{50}$ diblock copolymer illustrates clearly that the changes in the solution properties of the polymer as α is varied between 1.0 and 0.0 are closely related to changes in the polymer molecular structure for the same values of α. Thus for α = 1.0 to α > 0.3 the number of soluble DEAEMA units decrease only gradually and the polymer exists mainly as unimers in solution in addition to the appearance of a few polymer aggregates of low intensity. However, for α = 0.2 the intensity of the polymer aggregates increases accompanied by a simultaneous decrease in the number of soluble DEAEMA moles. This result suggests an increase in the hydrophobicity of the PDEAEMA block at this value of α, thus leading to increased aggregation before the formation of the equilibrium micelles at α = 0.0 which is also observed as a disappearance of the peaks corresponding to the protons of the PDEAEMA block in the NMR spectrum, and thus a sharp drop to zero of the soluble DEAEMA units.

It is interesting to note that both DLS and NMR results suggest that the polymer remains soluble for as low as 30% protonated DEAEMA units while equilibrium micelles are only formed when all DEAEMA groups become deprotonated. The triggering of the micellization process of the PHEGMA$_{50}$-*b*-PDEAEMA$_{50}$ diblock copolymer in such a narrow range of α, could be advantageous for either the development of very sensitive sensing elements where even very small changes in the acidity/basicity of the solution can be observed or in biomedical applications where for example a very small change in the pH could trigger drug release.

In order to further explore the formation of the few polymer aggregates at low pH [2] and high α as discussed above when the PDEAEMA block is fully protonated and thus hydrophilic we examined the solution properties of a PHEGMA$_{50}$-*b*-PDEAEMA$_{50}$ copolymer solution as a function of salt concentration.

The PHEGMA$_{50}$-*b*-PDEAEMA$_{50}$ diblock copolymer was first dissolved in water at pH 2 and at a 0.1 wt% polymer concentration. DLS study of this solution revealed a low scattered intensity and two processes corresponding to hydrodynamic radii $R_{h,1}$ = (3.5 ± 0.2) nm and $R_{h,2}$ = (82 ± 2) nm and attributed to unimers and polymer aggregates respectively. **Figure 3.7** illustrates the wavevector dependence of the intensity of the two processes.

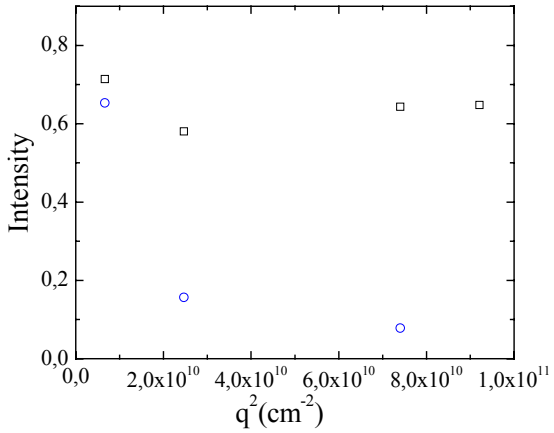

Figure 3.7 Wavevector dependence of the intensities of the fast (□) and the slow (○) process obtained for a 0.1 wt% $PHEGMA_{50}$-*b*-$PDEAEMA_{50}$ diblock copolymer solution at pH 2.

Next, the solution pH was increased by the addition of NaOH to pH 10 and the sample was left stirring overnight. At this pH the scattered intensity increased sharply and both micelles with $R_{h,1}$ = (13.0 ± 0.5) nm and micellar aggregates with $R_{h,2}$ = (103 ± 2) nm were observed by DLS. **Figure 3.8** shows the q-dependence of the intensity of the two processes.

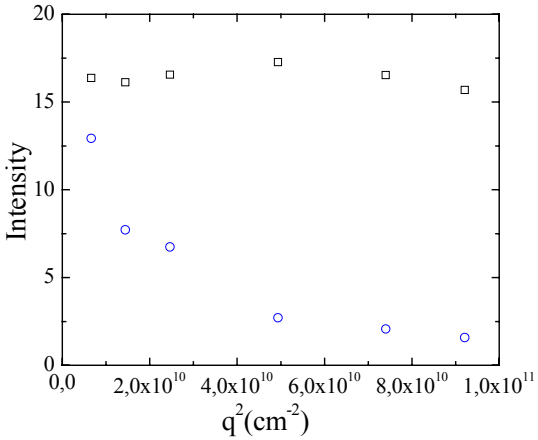

Figure 3.8 Wavevector dependence of the intensities of the fast (□) and the slow (○) process obtained for a 0.1 wt% $PHEGMA_{50}$-*b*-$PDEAEMA_{50}$ diblock copolymer solution at pH 10.

Subsequently, the pH of the solution was decreased back to pH 2 by the addition of HCl. The calculated amount of salt formed in this solution due to the

addition of both HCl and NaOH was found 0.004 M. DLS studies showed a significant drop of the scattered intensity and two processes with hydrodynamic radii $R_{h,1}$ = (4.0 ± 0.2) nm and $R_{h,2}$ = (110 ± 2) nm, attributed to the diffusion of unimers and polymer aggregates respectively, as discussed above, for pH 2. **Figure 3.9** illustrates the wavevector dependence of the intensity of the two processes.

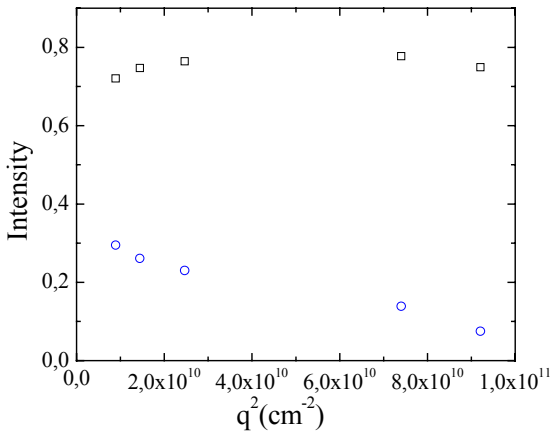

Figure 3.9 Wavevector dependence of the intensities of the fast (□) and the slow (○) process obtained for a 0.1 wt% $PHEGMA_{50}$-*b*-$PDEAEMA_{50}$ diblock copolymer solution at pH 2 in the presence of 0.004 M salt.

It is interesting to note that while the intensity of the unimers remain fairly constant (**Figures 3.7** and **3.9**) a decrease of the intensity of the slow process in the presence of salt is observed suggesting that the aggregates diminish upon addition of salt in solution.

Next, $PHEGMA_{50}$-*b*-$PDEAEMA_{50}$ copolymer solutions were examined systematically at different salt concentrations in order to verify the above mentioned argument and determine the salt concentration at which the aggregates disappear. Copolymer solutions at a 0.1 wt% polymer concentration and pH 2 were investigated for added salt concentrations 0.025 M, 0.1 M and 0.15 M which are higher than the amount of salt formed when the pH of a 0.1 wt% block copolymer solution is increased from pH 2 to pH 10 and then decreased back to 2 (0.004 M). For 0.025 M salt concentration two processes were again obtained by DLS with $R_{h,1}$ = (4.0 ± 0.2) nm and $R_{h,2}$ = (91 ± 2) nm, attributed to the diffusion of unimers and polymer aggregates respectively. **Figure 3.10** illustrates the wavevector dependence of the intensity of the two processes, at salt concentration c = 0.025 M.

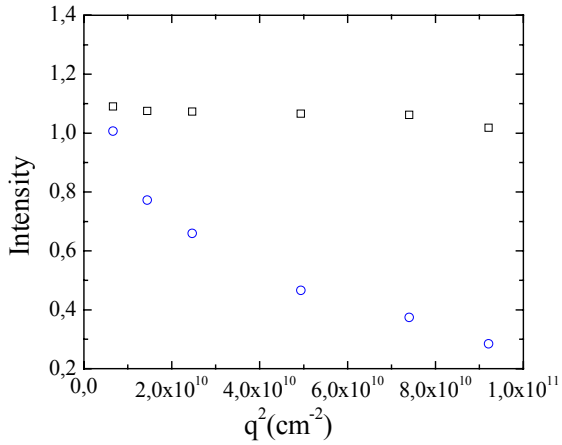

Figure 3.10 Wavevector dependence of the intensities of the fast (□) and the slow (○) process for a 0.1 wt% $PHEGMA_{50}$-*b*-$PDEAEMA_{50}$ diblock copolymer solution at pH 2 in the presence of 0.025 M salt.

Next, a 0.1 wt% copolymer solution at 0.1 M salt concentration and pH 2 was investigated by DLS. **Figure 3.11** illustrates the wavevector dependence of the intensities of the two processes (unimers and polymer aggregates) obtained for this solution. It is interesting to observe that the intensity of the slow process has decreased significantly and is almost constant, as shown in **Figure 3.11**, suggesting that for this salt concentration the aggregates almost disappear.

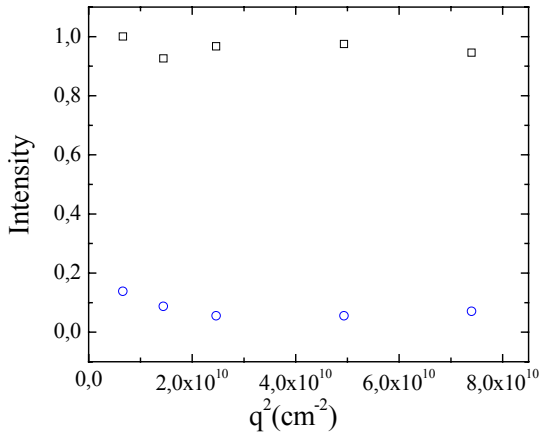

Figure 3.11 Wavevector dependence of the intensities of the fast (□) and the slow (○) process obtained for a 0.1 wt% $PHEGMA_{50}$-*b*-$PDEAEMA_{50}$ diblock copolymer solution at pH 2 in the presence of 0.1 M salt.

Finally, a 0.1 wt% copolymer solution at 0.15 M salt concentration and pH 2 was investigated. **Figure 3.12** illustrates the q-dependence of the intensities of the two processes (unimers and polymer aggregates) obtained for this solution.

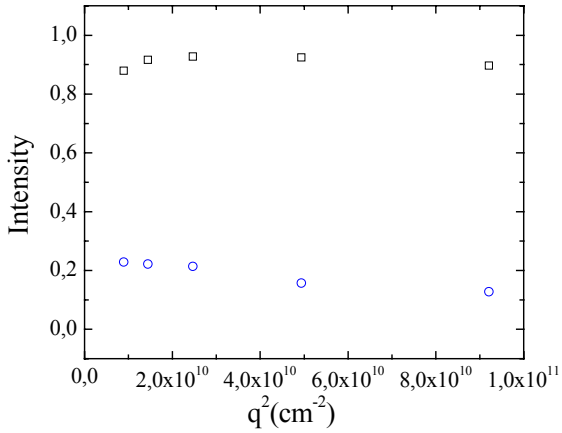

Figure 3.12 Wavevector dependence of the intensities of the fast (□) and the slow (○) process obtained for a 0.1 wt% $PHEGMA_{50}$-*b*-$PDEAEMA_{50}$ diblock copolymer solution at pH 2 in the presence of 0.15 M salt.

From **Figures 3.11** and **3.12** we observe that further addition of salt from 0.1 M to 0.15 M did not affect the intensity of the process attributed to the polymer aggregates, which remains very low and fairly constant suggesting that this process is insignificant.

The above results indicate that the formation of polymer aggregates in the salt-free polyelectrolyte solution at high α values (or low pH) is due to the polyelectrolyte effect [4]. Similar observations have been reported earlier in the literature where the unusual scattering from salt-free polyelectrolyte solutions was attributed to strong interactions of unscreened charges along the polymer chain which dominate the dynamics of the system. These electrostatic interactions are known as the so-called polyelectrolyte effect [5, 6, 7].

3.2 Metal nanoparticle formation

3.2.1 General

In an earlier study [8] it was shown that the core of the above micelles is able to dissolve metal compounds due to coordination with the amine units. In these micellar nanoreactors, metal nanoparticles nucleate and grow upon reduction with sizes in the range of a few nanometers. The polymer behavior, polymer-metal interactions and metal nanoparticle characteristics upon metal precursor incorporation and after metal reduction, were studied by dynamic light scattering, UV/Vis and ^{1}H NMR spectroscopy, transmission electron microscopy and X-ray diffraction. Two different methods for metal incorporation have been explored. In the first method (Method A), the metal compounds (H_2PtCl_6 and K_2PtCl_6) were added to a polymer solution in its unimer state at low pH. Metal reduction was carried out next at both low and high pH and its effect on the polymer characteristics was examined by DLS. In the second method (Method B), the metal compounds were introduced in a micellar polymer solution at high pH followed by metal reduction.

3.2.2 Method A: Addition of the metal precursor at low pH

3.2.2.1 Hexachloroplatinic acid (H_2PtCl_6) - Metal reduction at low pH

In this method, the $PHEGMA_{50}$-*b*-$PDEAEMA_{40}$ diblock copolymer was first dissolved in water at pH 2.3, at a 0.33 wt% polymer concentration. At this pH the amine groups of the PDEAEMA block are prototated and thus hydrophilic and the polymer exist as unimers in solution. Two processes with low intensities (**Figure 3.13**) are observed in the distribution of relaxation times similar to the results discussed above for high α in section 3.1.2. The fast process is attributed to the diffusion of free chains of the polymer with $R_{h,1}$ = (3.0 ± 0.2) nm, while the second slow process is attributed to the diffusion of polymer aggregates with $R_{h,2}$ = (60 ± 2) nm. Guinier fit of the slow process gives the radius of gyration R_g = (55 ± 4)nm.

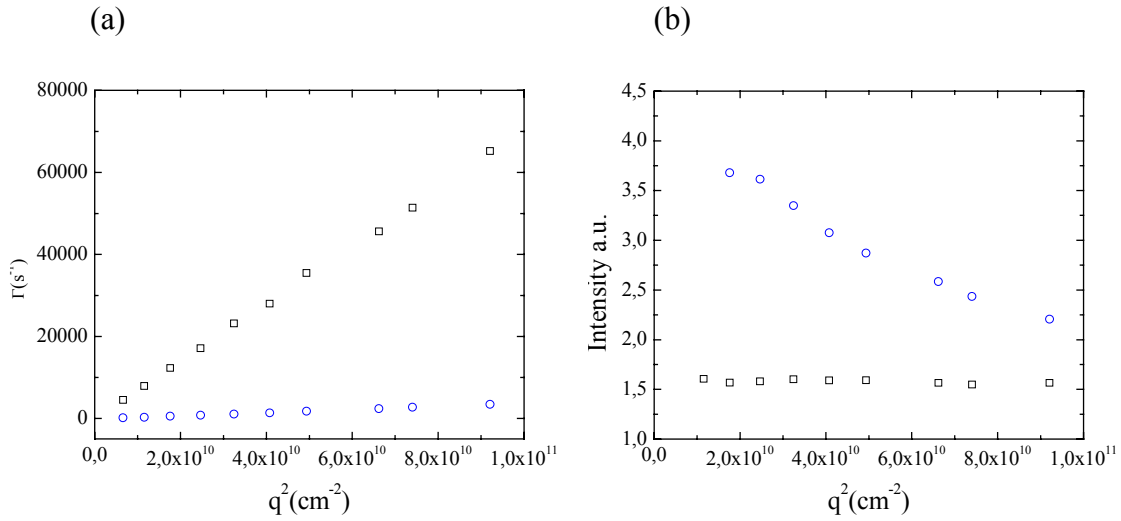

Figure 3.13 Wavevector dependence of a) the rates and b) the intensities of the fast (□) and the slow (○) process of a 0.33 wt% PHEGMA$_{50}$-*b*-PDEAEMA$_{40}$ diblock copolymer solution at pH 2.3.

Hexachloroplatinic(IV) acid (H_2PtCl_6) at a N/Pt = 3/1 molar ratio was added next in the unimer solution causing the pH to decrease to 2.1. **Figure 3.14** shows the intensity autocorrelation functions for the metallated PHEGMA$_{50}$-*b*-PDEAEMA$_{40}$ diblock copolymer solution at various scattering angles.

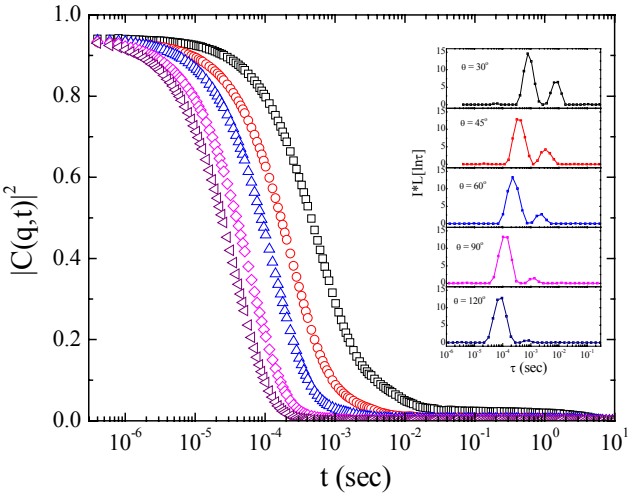

Figure 3.14 Intensity autocorrelation functions for a 0.33 wt% metallated (H_2PtCl_6) PHEGMA$_{50}$-*b*-PDEAEMA$_{40}$ diblock copolymer solution at pH 2.1 and scattering angle 30º (□), 45º (○), 60º (△), 90º (◇) and 120º (◁). Inset: distribution of relaxation times multiplied by the total scattering intensity (normalized to that of toluene).

Two processes with very strong intensities are observed in the autocorrelation function with diffusivities $D_1 = 1.69 \times 10^{-7}$ cm^2/s and $D_2 = 1.79 \times 10^{-8}$ cm^2/s which correspond to hydrodynamic radii $R_{h,1} = (12.6 \pm 0.5)$ nm and $R_{h,2} = (119 \pm 2)$ nm respectively. The intensity of the slow process is q^2-dependent; guinier fit gives the radius of gyration $R_g = (106 \pm 4)$ nm (**Figure 3.15**).

The fast process observed in the distribution of relaxation times is attributed to the formation of micelles due to electrostatic interactions between the divalent metal anions $PtCl_6^{2-}$ and the positively charged protonated DEAEMA units of the polymer leading to metal-induced micellization with the platinic anions incorporated within the cores of the micelles. It should be emphasized that a divalent anion is necessary for metal-induced micellization to occur while monovalent anions (i.e. Cl^-) cannot lead to micellization due to their 1:1 interactions with the charged amines. It is also worth noting that the size of these metal-induced micelles is comparable to that of the non-metallated micellar structures formed at low values of α when the PDEAEMA block becomes hydrophobic (see section 3.1.2). The slow process observed in the distribution of relaxation times is attributed to the diffusion of micellar aggregates which are formed due to the insufficient stability conferred by the short micelle coronas.

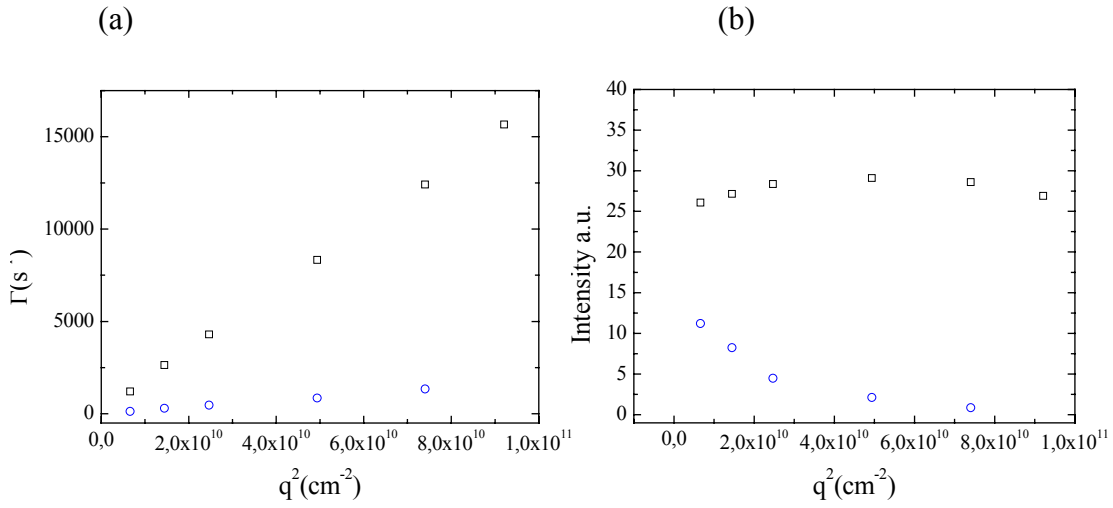

Figure 3.15 Wavevector dependence of a) the rates and b) the intensities of the fast (□) and the slow (○) process of a 0.33 wt% $PHEGMA_{50}$-*b*-$PDEAEMA_{40}$ diblock copolymer solution in the presence of H_2PtCl_6 at pH 2.1.

Platinum reduction using $NaBH_4$ results in metal nanoparticle formation and causes an increase of the solution pH to 2.5. Upon metal reduction the solution turns instantly black and thus has very high absorbance at λ = 532 nm which hinders the DLS measurement of the sample. To overcome this problem a 3-fold dilution was performed to a final polymer concentration of ~ 0.1 wt%. DLS measurement of this diluted sample depicts two diffusive processes with diffusion coefficients D_1 = 2.46×10^{-7} cm^2/s and D_2 = 1.96×10^{-8} cm^2/s corresponding to hydrodynamic radii $R_{h,1}$ = (8.8 ± 0.5) nm and $R_{h,2}$ = (109 ± 2) nm respectively.

It is interesting to observe that both the size and the intensity of the fast process decrease compared to those obtained for the metal-induced micelles at low pH **(Figures 3.15 and 3.16)**. Therefore, metal reduction at low pH leads to the partial decomposition of the metal-induced micelles due to the elimination of the strong polymer-metal electrostatic interactions while the process obtained after metal reduction is attributed to the diffusion of a few loose structures formed due to the remaining weak polymer-metal interactions. The slow process is again attributed to the diffusion of polymer aggregates with very low q^2-dependent intensity. The radius of gyration was calculated to be (95 ± 4) nm. These DLS results are in good agreement with our NMR studies discussed in a following section.

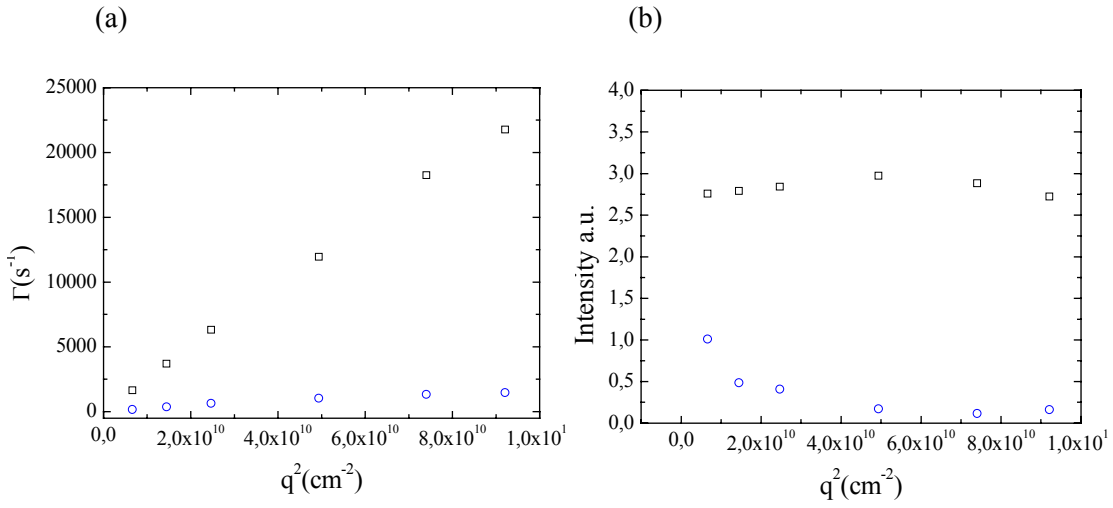

Figure 3.16 Wavevector dependence of a) the rates and b) the intensities of the fast (□) and the slow (○) process of a 0.1 wt% $PHEGMA_{50}$-*b*-$PDEAEMA_{40}$ diblock copolymer solution (H_2PtCl_6) after metal reduction at pH 2.5.

Finally, the pH of the solution was increased to 9.5 using 0.1 M NaOH. The distribution of relaxation times of the reduced sample exhibit a dominant mode with strong and constant intensity (**inset Figure 3.18**). The diffusion coefficient of this process is $D_1 = 1.72x10^{-7}$ cm^2/s, corresponding to a hydrodynamic radius $R_{h,1}$ = (12.5 ± 0.5) nm and is attributed to the diffusion of polymer micelles which contain metal nanoparticles when formed at high pH. **Figure 3.17** illustrates the wavevector dependence of the intensity and the rate of the fast process.

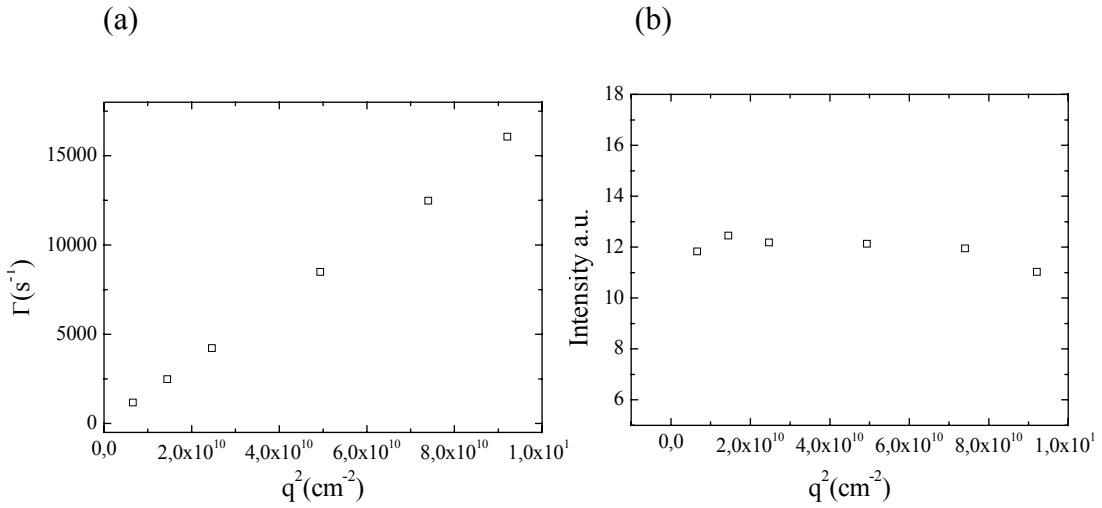

Figure 3.17 Wavevector dependence of a) the rate and b) the intensity of the process of a 0.1 wt% $PHEGMA_{50}$-*b*-$PDEAEMA_{40}$ diblock copolymer solution (H_2PtCl_6) after metal reduction at pH 9.5.

Figure 3.18 shows the autocorrelation functions at 60º scattering angle for all samples discussed above. The distributions of relaxation times shown in the inset depict clearly the transition from single polymer chains of low intensity to metal-induced micelles upon addition of H_2PtCl_6 and the subsequent formation of smaller and low intensity structures upon metal reduction at low pH. Finally the formation of polymer micelles with high intensity due to the hydrophobicity of the DEAEMA units at high pH is observed. The significantly higher scattering intensity of the micelles compared to that of the micellar aggregates in the last sample suggests that the later are very few in number and their analysis was not possible.

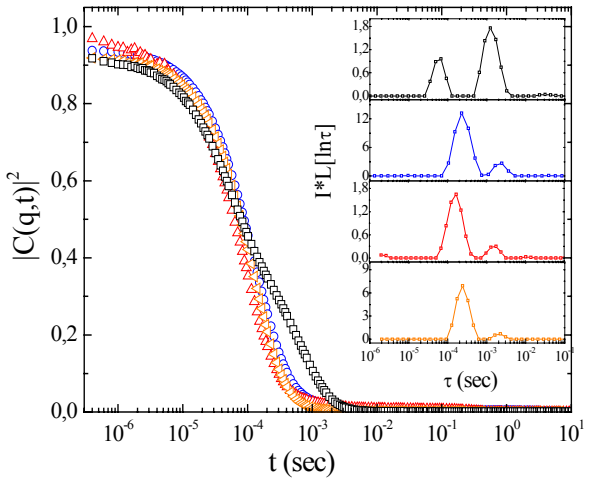

Figure 3.18 Autocorrelation functions of a $PHEGMA_{50}$-*b*-$PDEAEMA_{40}$ diblock copolymer solution at 60º scattering angle; at pH 2.3 and c = 0.33 wt% (□), the same solution in the presence of H_2PtCl_6 at pH 2.1 (○), the sample after metal reduction at c = 0.1 wt% and pH 2.5 (△), the final solution at c = 0.1 wt% and pH 9.5 (◁). Inset: distribution of relaxation times multiplied by the total scattering intensity (normalized to that of toluene).

3.2.2.2 Hexachloroplatinic acid (H_2PtCl_6) - Metal reduction at high pH

Similar to the above method the $PHEGMA_{50}$-*b*-$PDEAEMA_{50}$ diblock copolymer was first dissolved in water at pH 2.3, at a 0.33 wt% polymer concentration. At this pH the copolymer is in its unimer state due to the hydrophilicity of the DEAEMA units with $R_{h,1}$ = (4.0 ± 0.2) nm, as discussed above and was again confirmed by DLS. A few aggregates also exist in solution with hydrodynamic radius $R_{h,2}$ = (65 ± 2) nm and radius of gyration R_g = (58 ± 4) nm. **Figure 3.19** illustrates the wavevector depedence of the intensities and the rates of these two processes.

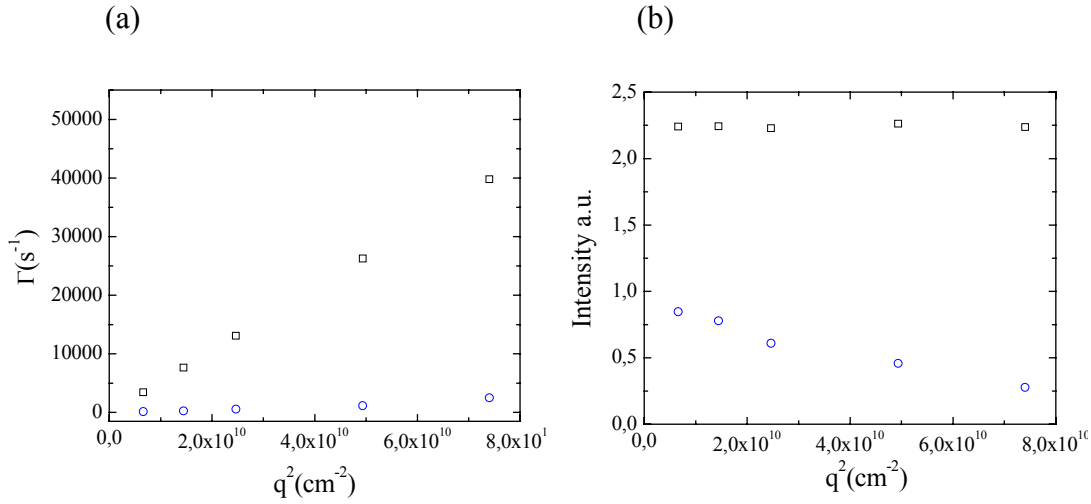

Figure 3.19 Wavevector dependence of a) the rates and b) the intensities of the fast (□) and the slow (○) process of a 0.33 wt% $PHEGMA_{50}$-*b*-$PDEAEMA_{50}$ diblock copolymer solution at pH 2.3.

Addition of H_2PtCl_6 at a N/Pt = 3/1 molar ratio in this polymer solution resulted in the decrease of the solution pH to 2.1. DLS measurement of this sample showed one process with very high intensity and strong dynamics which dominates the correlation function.

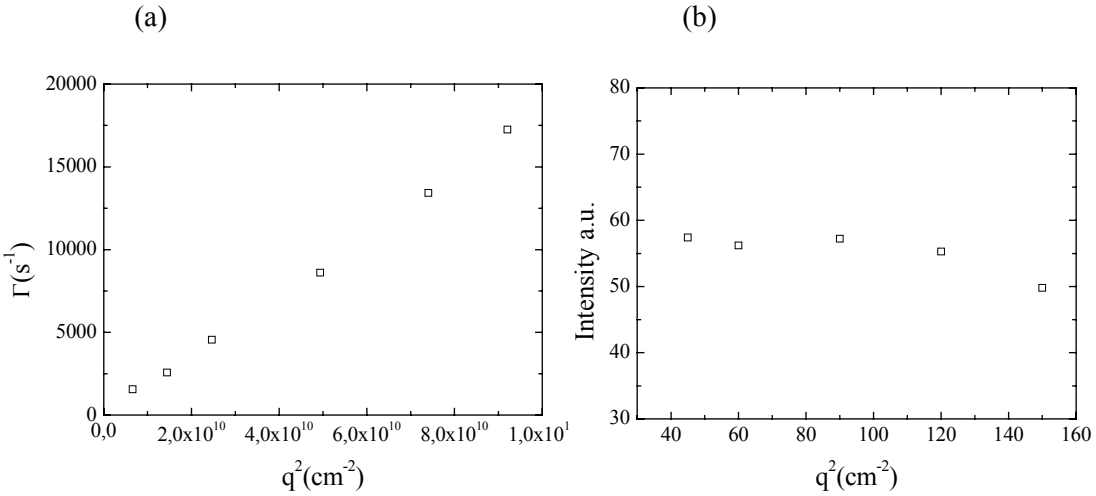

Figure 3.20 Wavevector dependence of a) the rate and b) the intensity of the process of a 0.33 wt% $PHEGMA_{50}$-*b*-$PDEAEMA_{50}$ diblock copolymer solution in the presence of H_2PtCl_6 at pH 2.1.

The diffusivity of the process was found $D_1 = 1.83 \times 10^{-7}$ cm^2/s which corresponds to a hydrodynamic radius $R_h = (12 \pm 0.5)$ nm and was attributed to the diffusion of the metal-induced micelles, formed at low pH and discussed in the section above for a similar sample. **Figure 3.20** illustrates the wavevector depedence of the intensity and the rate of the above process.

Next, the solution pH was increased to 9.5 by the addition of NaOH. Two processes with diffusion coefficients $D_1 = 1.53 \times 10^{-7}$ cm^2/s and $D_2 = 1.62 \times 10^{-8}$ cm^2/s corresponding to hydrodynamic radii $R_{h,1} = (14.0 \pm 0.5)$ nm and $R_{h,2} = (130 \pm 2)$ nm were obtained by DLS. The wavevector dependence of the rates and the intensities of the two processes are shown in **Figure 3.21**. The fast process is attributed to the diffusion of micelles formed due to the hydrophobicity of the amine groups of the copolymer at high pH, while the second slow process corresponds to the diffusion of micellar aggregates. It is worth noting that the intensity of the fast process (**Figure 3.21b**) exhibits strong fluctuations which might result from interactions between the non-captured $PtCl_6^{2-}$ anions and the PHEGMA blocks forming the corona of the micelles.

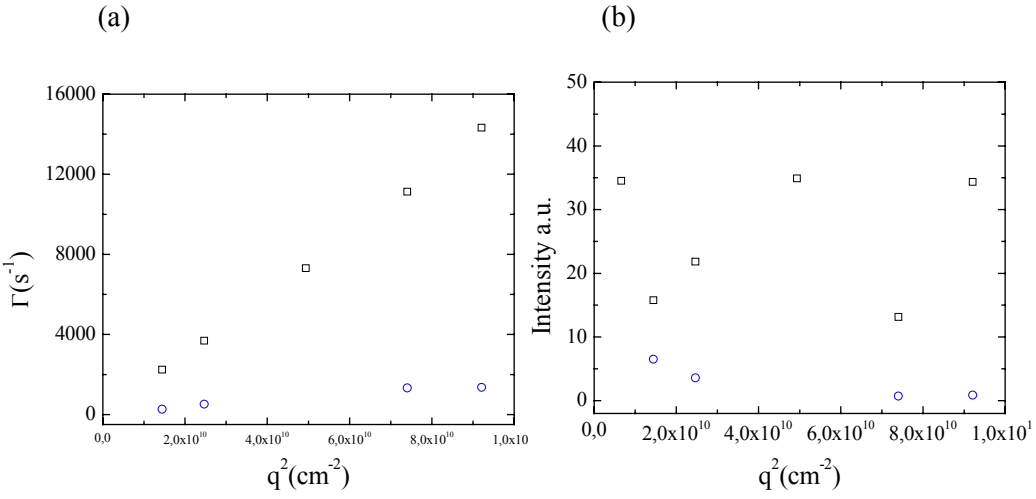

Figure 3.21 Wavevector dependence of a) the rates and b) the intensities of the fast (□) and the slow (○) process of a 0.33 wt% $PHEGMA_{50}$-*b*-$PDEAEMA_{50}$ diblock copolymer solution in the presence of H_2PtCl_6 at pH 9.5.

Finally, metal reduction using $NaBH_4$ resulted in the increase of the solution pH to 9.8 and the formation of the metal nanoparticles. After a 3-fold dilution, the

sample was studied by DLS. Two diffusive processes were obtained with diffusion coefficients $D_1 = 1.61 \times 10^{-7}$ cm^2/s and $D_2 = 4.08 \times 10^{-8}$ cm^2/s corresponding to micelles and micellar aggregates with hydrodynamic radii $R_{h,1} = (13.5 \pm 0.5)$ nm and $R_{h,2} = (52 \pm 2)$ nm respectively. **Figure 3.22** illustrates the q-depedence of the intensities and the rates for the two processes. It is worth noting that in the reduced sample an extraordinary high intensity for the slow process is obtained suggesting extensive micelle aggregation caused by the reduction of the metal and the possible interactions of the reduced metal particles with the PHEGMA blocks in the corona of the micelles.

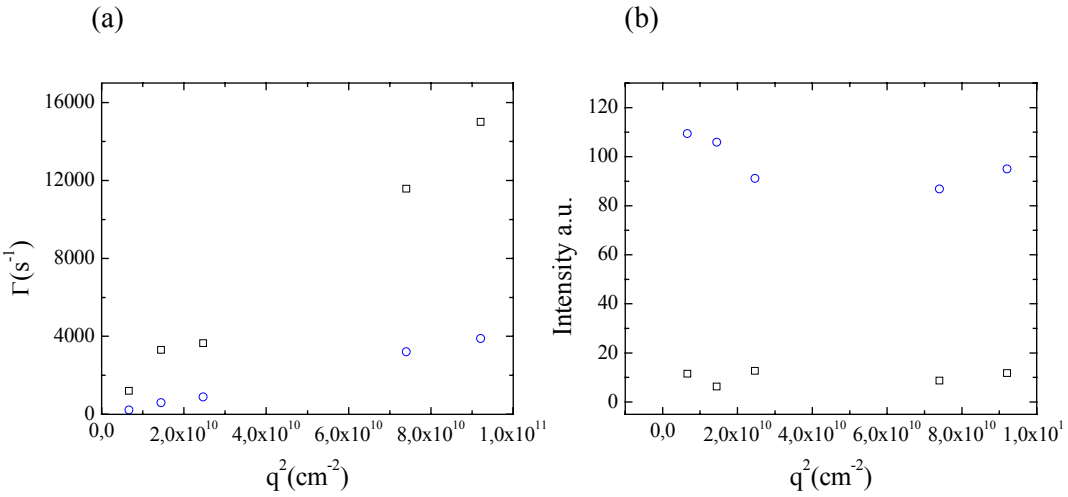

Figure 3.22 Wavevector dependence of a) the rates and b) the intensities of the fast (□) and the slow (○) process of a 0.1 wt% $PHEGMA_{50}$-*b*-$PDEAEMA_{50}$ diblock copolymer solution (H_2PtCl_6) after metal reduction at pH 9.8.

Figure 3.23 shows the autocorrelation functions for all samples discussed above at 60º scattering angle. The transition from low intensity single polymer chains to metal-induced micelles of high intensity upon addition of H_2PtCl_6 at low pH is observed similar to the results for the first method discussed above for the previous sample. Next the formation of regular micelles at high pH values is obtained with sizes similar to their metal-induced analogues and big fluctuations in their intensity. Finally, upon metal reduction at high pH besides the micelles, extensive micelle aggregation is observed as suggested by the high intensity of the aggregates.

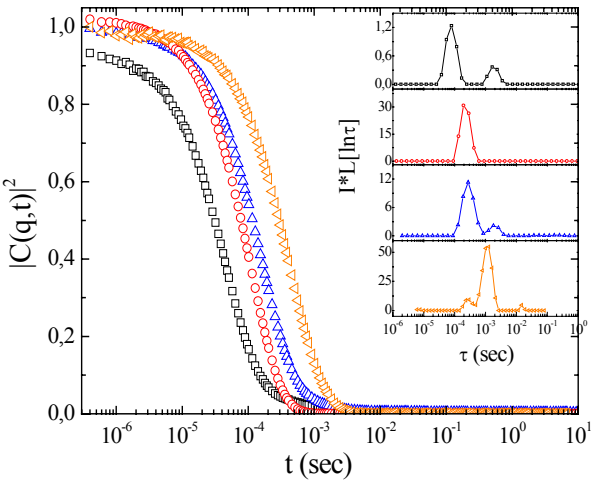

Figure 3.23 Autocorrelation functions of a $PHEGMA_{50}$-*b*-$PDEAEMA_{50}$ diblock copolymer solution at 60º scattering angle, at pH 2.3 and c = 0.33 wt% (□), the same solution in the presence of H_2PtCl_6 at pH 2.1 (○) the metallated sample after addition of NaOH at pH 9.5 (△) the final sample upon metal reduction at pH 9.5 and c = 0.1 wt% (◁). Inset: distribution of relaxation times multiplied by the total scattering intensity (normalized to that of toluene).

3.2.2.3 Potassium Hexachloroplatinate (K_2PtCl_6) - Metal reduction at low pH

Similar to the procedure followed above for the addition of the platinic acid, the $PHEGMA_{50}$-*b*-$PDEAEMA_{50}$ diblock copolymer was first dissolved in water at pH 2.1, at a 0.33 wt% polymer concentration. DLS study of the this sample consistently showed the existence of two processes with diffusion coefficients $D_1 = 5.36 \times 10^{-7}$ cm^2/s and $D_2 = 2.67 \times 10^{-8}$ cm^2/s corresponding to hydrodynamic radii $R_{h,1} = (4.0 \pm 0.2)$ nm and $R_{h,2} = (80 \pm 2)$ nm respectively. **Figure 3.24** illustrates the q-depedence of the intensities and the rates of the two processes, which are similar to the data obtained above (**Figures 3.13 and 3.19**) for the addition of H_2PtCl_6. The low intensity fast process is attributed to the diffusion of the free chains of the copolymer, while the slow process is attributed to the diffusion of a few polymer aggregates as discussed above (see above section 3.1.2).

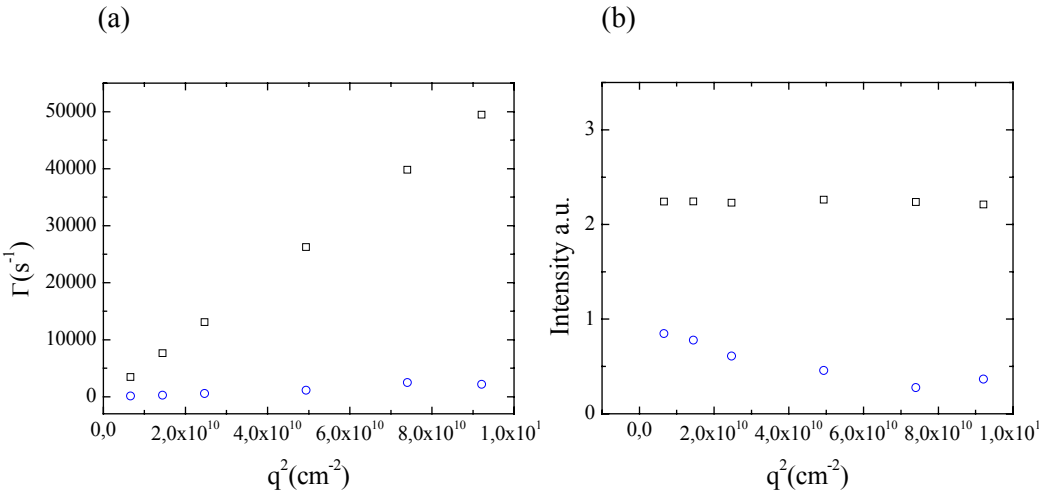

Figure 3.24 Wavevector dependence of a) the rates and b) the intensities of the fast (□) and the slow (○) process of a 0.33 wt% $PHEGMA_{50}$-*b*-$PDEAEMA_{50}$ diblock copolymer solution at pH 2.1.

The platinic salt, K_2PtCl_6, at a N/Pt = 3/1 molar ratio was introduced next in the solution and had no effect on the solution pH, as expected. The autocorrelation functions for this metallated sample (**Figure 3.25**) depict the existence of two processes with diffusivities D_1 = 1.87x10^{-7} cm^2/s and D_2 = 1.77x10^{-8} cm^2/s which correspond to hydrodynamic radii $R_{h,1}$ = (11.5 ± 0.5) nm and $R_{h,2}$ = (120 ± 2) nm respectively.

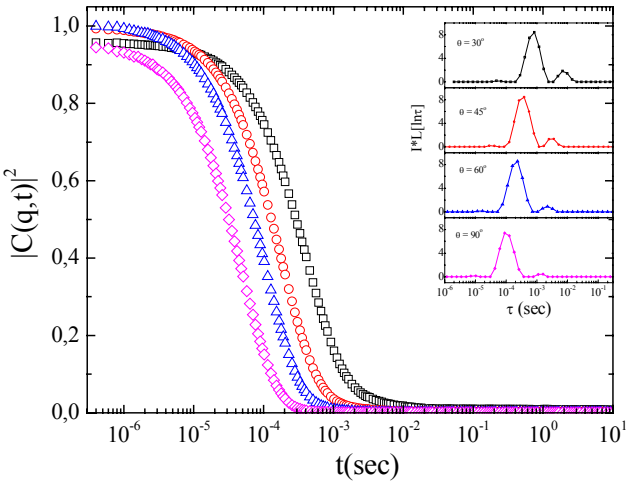

Figure 3.25 Intensity autocorrelation functions for a 0.33 wt% metallated (K_2PtCl_6) $PHEGMA_{50}$-*b*-$PDEAEMA_{50}$ diblock copolymer solution at pH 2.1 and scattering angle 30º (□), 45º (○), 60º (△) and 90º (◇). Inset: distribution of relaxation times multiplied by the total scattering intensity (normalized to that of toluene).

The fast process observed in the distribution of relaxation times (**inset Figure 3.25**) has high intensity and strong dynamics (**Figure 3.26**) and is attributed to the diffusion of the metal-induced micelles formed due to the electrostatic interactions between the divalent metal anions $PtCl_6^{2-}$ and the protonated cationic DEAEMA units of the polymer, as discussed above. It is interesting to note that the size of these micelles is similar to those obtained before both for the non-metallated samples at high pH and the H_2PtCl_6 containing sample at low pH when similar metal-induced micellization was observed, suggesting the formation of stable equilibrium structures in all cases controlled rather by the polymer characteristics and not the preparation method. The second slow process which has very low and q^2-dependent intensity (**Figure 3.26b**) corresponds to the diffusion of a few large micellar aggregates (R_g = (108 ± 4) nm) similar to the results obtained above for the H_2PtCl_6 - containing sample (**Figure 3.15**).

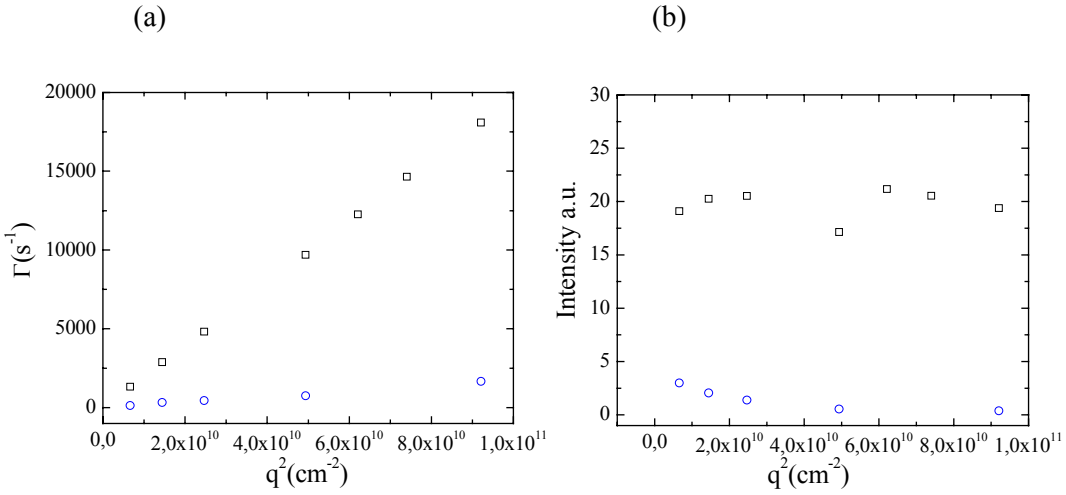

Figure 3.26 Wavevector dependence of a) the rates and b) the intensities of the fast (□) and the slow (○) process of a 0.33 wt% $PHEGMA_{50}$-*b*-$PDEAEMA_{50}$ diblock copolymer solution in the presence of K_2PtCl_6 at pH 2.1.

Metal reduction was carried out next, using $NaBH_4$ which caused the solution pH to increase to 2.3 and the solution became black in color due to the formation of the metal nanoparticles. A 3-fold dilution of the solution was required before the DLS study, in order to minimize light absorbance by the sample. The distribution of

relaxation times for this sample revealed two processes with diffusion coefficients D_1 = 2.31x10^{-7} cm^2/s and D_2 = 2.62x10^{-8} cm^2/s corresponding to hydrodynamic radii $R_{h,1}$ = (9.3 ± 0.5) nm and $R_{h,2}$ = (82 ± 2) nm respectively. **Figure 3.27** illustrates the q-depedence of the intensities and the rates of these two processes. Guinier fit of the intensity of the slow process gives the radius of gyration R_g = (58 ± 4) nm.

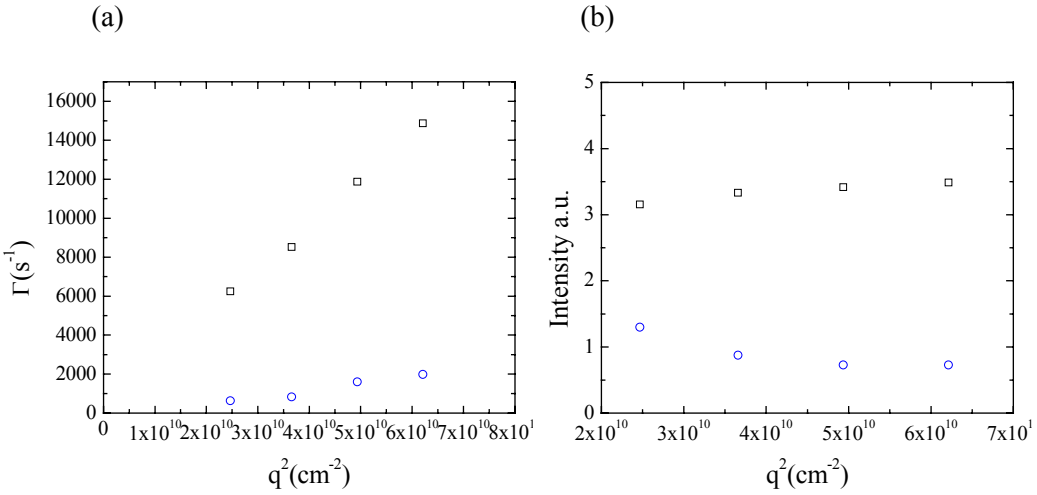

Figure 3.27 Wavevector dependence of a) the rates and b) the intensities of the fast (□) and the slow (○) process of a 0.1 wt% $PHEGMA_{50}$-*b*-$PDEAEMA_{50}$ diblock copolymer solution (+K_2PtCl_6) after metal reduction at pH 2.3.

Upon metal reduction a decrease in the intensity (**Figure 3.27b**) and the size of the fast process was observed suggesting the partial decomposition of the metal-induced micelles, as discussed above for the reduction of H_2PtCl_6 (**Figure 3.16**). This has been attributed to the elimination of the strong polymer-metal electrostatic interactions upon metal reduction and the presence of only weak polymer-metal interactions which result in the formation of the loose structures observed in the reduced sample at low pH. The slow process is again related to the formation of a few large polymer aggregates with low q^2-dependent intensity.

Next, the solution pH was increased to 9.5 by the addition of NaOH. DLS measurement revealed the formation of both micelles of high intensity and micellar aggregates in solution with hydrodynamic radii $R_{h,1}$ = (13.1 ± 0.5) nm and $R_{h,2}$ = 109 ± 2) nm respectively (D_1 = 1.63x10^{-7} cm^2/s and D_2 = 1.96x10^{-8} cm^2/s). These micelles are the metal-nanoparticle containing polymer structures formed at high pH following

metal reduction. **Figure 3.28** shows the q-depedence of the intensities and the rates of the two processes. Both the size and the intensities of the two processes are in good agreement with the results obtained above for the metal nanoparticle containing sample at high pH using H_2PtCl_6 as the metal precursor (**Figure 3.17**).

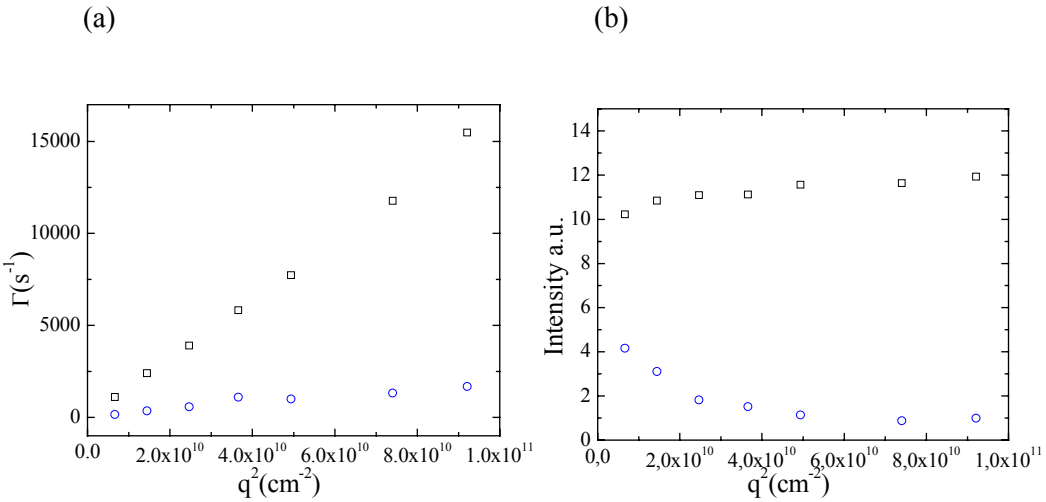

Figure 3.28 Wavevector dependence of a) the rates and b) the intensities of the fast (□) and the slow (○) process of a 0.1 wt% $PHEGMA_{50}$-*b*-$PDEAEMA_{50}$ diblock copolymer solution (+ K_2PtCl_6) upon metal reduction at pH 9.5.

Figure 3.29 shows the autocorrelation functions for all samples discussed above for K_2PtCl_6 incorporation and metal nanoparticle formation. Similar to the data obtained for H_2PtCl_6 (**Figure 3.18**), the formation of metal-induced micelles upon addition of K_2PtCl_6 in a unimer polymer solution, the partial decomposition of these micelles and the formation of smaller loose structures of low intensity after metal reduction at low pH and the reformation of micelles due to the hydrophobicity of the DEAEMA units at high pH, are followed nicely both in the autocorrelation functions and the distribution of relaxation times, shown in the insets.

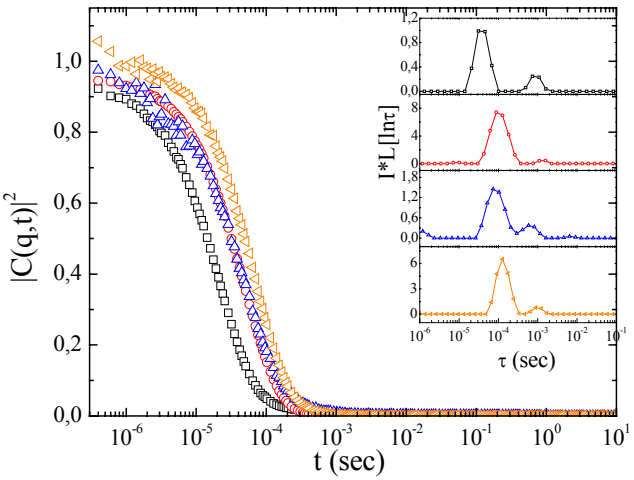

Figure 3.29 Autocorrelation functions of a PHEGMA$_{50}$-*b*-PDEAEMA$_{50}$ diblock copolymer solution at 90º scattering angle, at pH 2.1 and c = 0.33 wt% (□), the same solution in the presence of K_2PtCl_6 at pH 2.1 (○), the sample after metal reduction at c = 0.1 wt% and pH 2.5 (△) the final solution at c = 0.1 wt% and pH 9.5 (◁). Inset: distribution of relaxation times multiplied by the total scattering intensity (normalized to that of toluene).

3.2.2.4 Potassium Hexachloroplatinate (K_2PtCl_6) - Metal reduction at high pH

In this method the PHEGMA$_{50}$-*b*-PDEAEMA$_{50}$ diblock copolymer was first dissolved in water at pH 1.9, at a 0.33 wt% polymer concentration where unimers were formed due to the hydrophilicity of the protonated DEAEMA units (data not shown).

Next K_2PtCl_6 was added at a N/Pt = 3/1 molar ratio that had no effect on the pH of the solution. DLS study revealed one process with very high intensity and strong dynamics which dominated the correlation functions of the metallated sample; its diffusivity D = 1.74x10^{-7} cm^2/s corresponds to a hydrodynamic radius R_h = (12.3 ± 0.5) nm, which is attributed to the formation of the metal-induced micelles discussed previously. **Figure 3.30** shows the q-dependence of the intensitiy and the rate of this process which are similar to the data obtained for the addition of H_2PtCl_6 in the same sample (**Figure 3.20**).

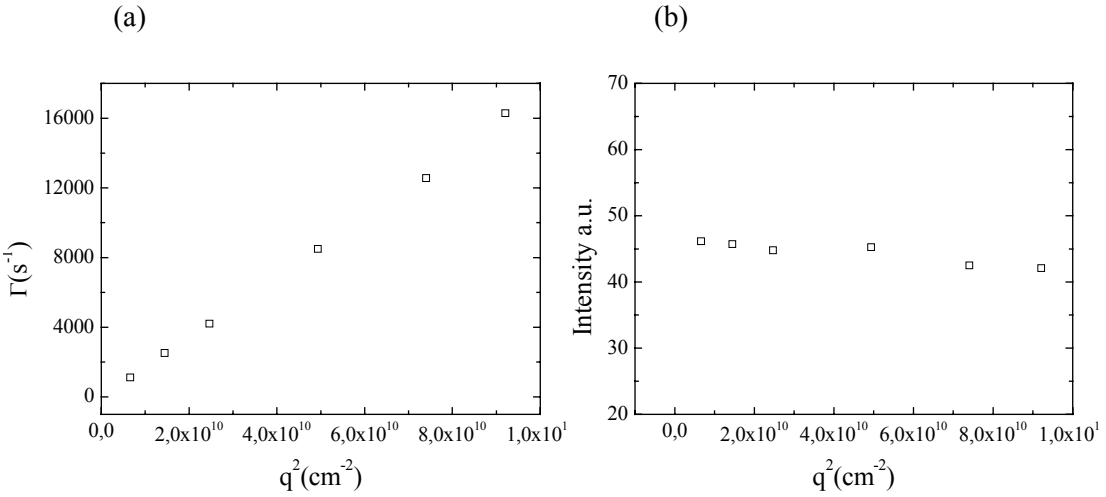

Figure 3.30 Wavevector dependence of a) the rate and b) the intensity of the process of a 0.33 wt% $PHEGMA_{50}$-*b*-$PDEAEMA_{50}$ diblock copolymer solution in the presence of K_2PtCl_6 at pH 1.9.

Next, the pH of the solution was increased to 9.5 by the addition of NaOH. One process was obtained for this sample by DLS with diffusion coefficient D = $1.8x10^{-7}$ cm^2/s that corresponds to a hydrodynamic radius R_h = (11.9 ± 0.5) nm and is attributed to the diffusion of micelles formed at this high pH due to the deprotonation of the amine groups of the copolymer which become hydrophobic. The wavevector dependence of the rate and the intensity of the process are shown in **Figure 3.31**.

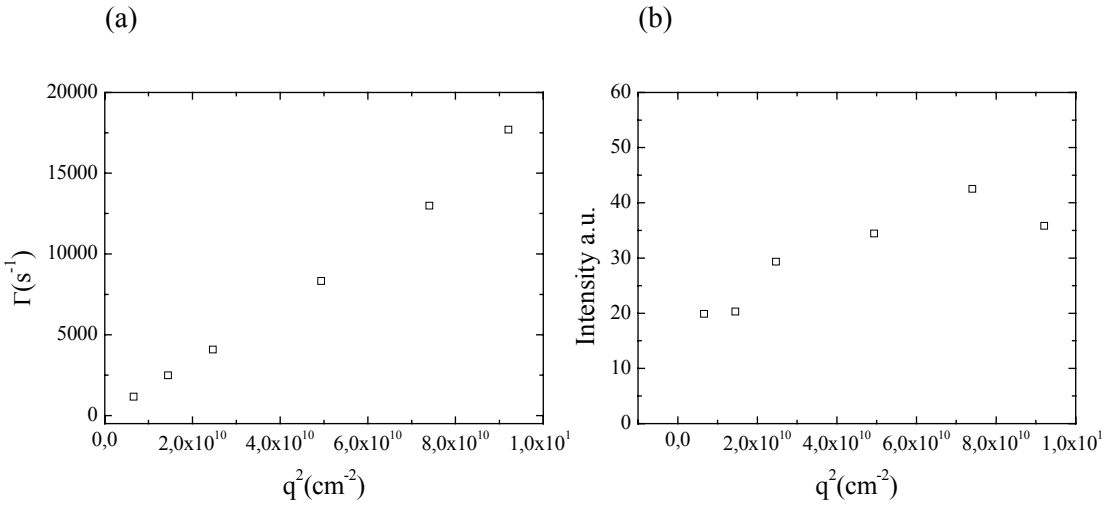

Figure 3.31 Wavevector dependence of a) the rate and b) the intensity of a 0.33 wt% $PHEGMA_{50}$-*b*-$PDEAEMA_{50}$ diblock copolymer solution in the presence of K_2PtCl_6 at pH 9.5.

What is interesting to observe here is that the intensity of the process exhibits strong fluctuations as observed earlier for a $PHEGMA_{50}$-*b*-$PDEAEMA_{50}$ diblock copolymer solution in the presence of H_2PtCl_6 at high pH and were attributed to interactions between the non-entrapped $PtCl_6^{2-}$ anions and the PHEGMA blocks forming the corona of the micelles.

Finally, upon metal reduction using $NaBH_4$ the pH of the above solution increased to 9.7. After a 3-fold dilution the sample was studied by DLS, which showed two processes with diffusion coefficients $D_1 = 1.49x10^{-7}$ cm^2/s, $D_2 = 3.53x10^{-8}$ cm^2/s corresponding to hydrodynamic radii $R_{h,1} = (14.5 \pm 0.5)$ nm and $R_{h,2} = (61 \pm 2)$ nm respectively. In consistency with our results above under similar conditions metal nanoparticle containing micelles and micellar aggregates are formed in the reduced sample at this high pH. **Figure 3.32** illustrates the wavevector dependence of the rates and the intensities of the two processes discussed above.

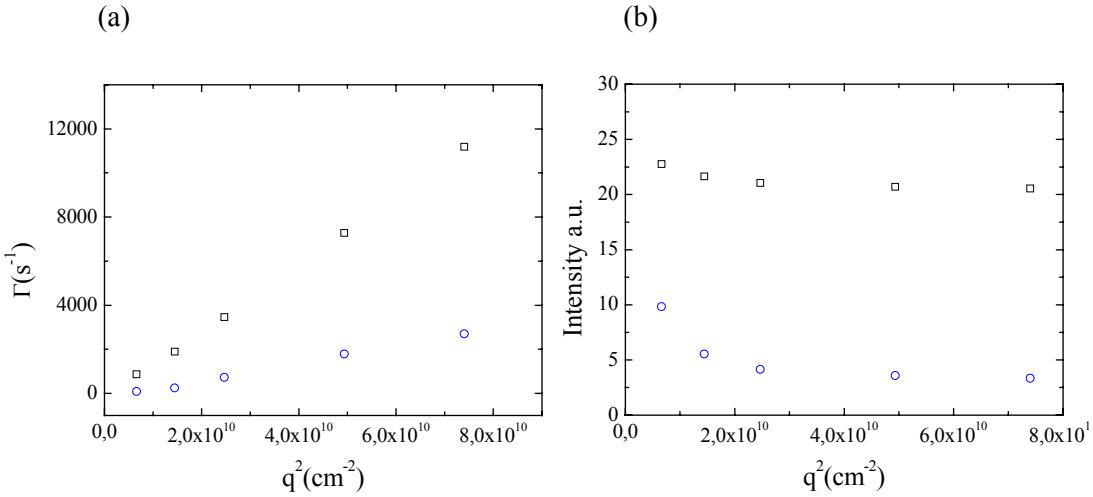

Figure 3.32 Wavevector dependence of a) the rates and b) the intensities of the fast (□) and the slow (○) process of a 0.1 wt% $PHEGMA_{50}$-*b*-$PDEAEMA_{50}$ diblock copolymer solution (+ K_2PtCl_6) after metal reduction at pH 9.5.

Figure 3.33 shows the autocorrelation functions for all samples discussed above at 90º scattering angle. The metal-induced micellization upon addition of K_2PtCl_6 at low pH and the formation of micelles at high pH values which do not change significantly upon metal reduction are observed both in the correlation functions and the distribution of relaxation times shown in the insets.

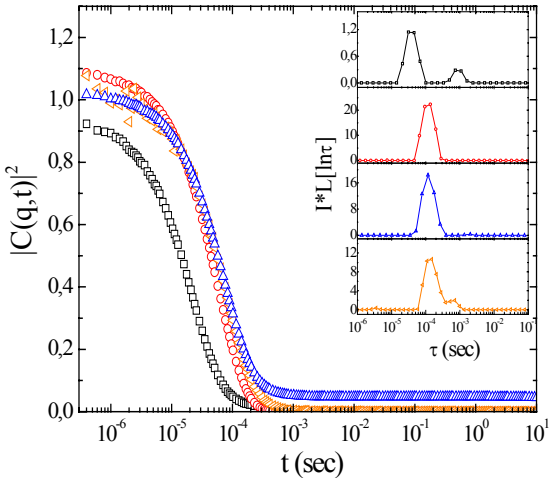

Figure 3.33 Autocorrelation functions of a $PHEGMA_{50}$-*b*-$PDEAEMA_{50}$ diblock copolymer solution at 90º scattering angle, at pH 1.9 and c = 0.33 wt% (□), the same solution in the presence of K_2PtCl_6 at pH 1.9 (○), the metallated sample after addition of NaOH at pH 9.5 (△), the final sample upon metal reduction at c=0.1 wt% and pH 9.7 (◁).Inset: distribution of relaxation times multiplied by the total scattering intensity (normalized to that of toluene).

In summary the above data have shown that in Method A the addition of the metal precursor at low pH results in the formation of micelles due to electrostatic interactions between the positively charged protonated DEAEMA units of the copolymer and the metal precursor anions. However, metal reduction at low pH leads to partial decomposition of these metal-induced micelles due to the elimination of the strong polymer-metal electrostatic interactions, while an increase of the solution pH leads to the formation of well-defined metal nanoparticle containing micelles. From the above data it is not possible to quantify the fraction of nanoparticles that are finally included within the micelle cores, and further studies are required to investigate the incorporation of the nanoparticles within the hydrophobic cores of the micelles formed upon increasing the solution pH, in the last step of the procedure. Moreover, the formation of metal nanoparticle containing micelles by metal reduction at high pH does not seem to be the most appropriate for metal incorporation, since DLS studies revealed strong fluctuations of the scattered intensity possibly resulting from interactions between the non-captured $PtCl_6^{2-}$ anions and the HEGMA units comprising the corona of the micelle. The latter suggests that a significant fraction of metal anions are only weakly bound in the exterior of the micellar structures thus

leading to the formation of only weakly stabilized metal nanoparticles after metal reduction.

3.2.3 Method B: Addition of the metal precursor at high pH

3.2.3.1 Hexachloroplatinic acid (H_2PtCl_6)

In this method a 0.33 wt% $PHEGMA_{50}$-*b*-$PDEAEMA_{50}$ diblock copolymer solution at pH 2 was first prepared. Next the pH of the solution was raised to 10 by the addition of NaOH. This causes deprotonation of the tertiary amine block, which becomes hydrophobic, and leads to the formation of well defined micelles. The distribution of relaxation times exhibit a dominant mode with strong and constant intensity (**see Figure 3.34b**) and a q^2 –dependent rate (**see Figure 3.34a**), which corresponds to the diffusion of polymer micelles with a hydrodynamic radius of $R_{h,1}$ = (12.0 ± 0.5)nm. The second slower diffusive process has significantly lower intensity, which is q-dependent (radius of gyration R_g = (89 ± 4) nm) and is attributed to the formation of a small number of micellar aggregates with hydrodynamic radius $R_{h,2}$ = (96 ± 2) nm.

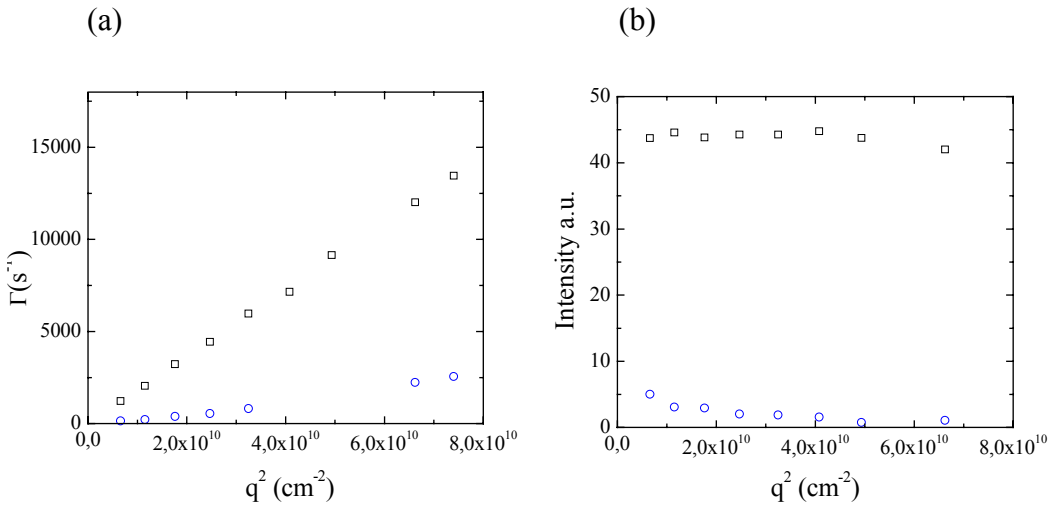

Figure 3.34 Wavevector dependence of a) the rates and b) the intensities of the fast (□) and the slow (○) process of a 0.33 wt% $PHEGMA_{50}$-*b*-$PDEAEMA_{50}$ diblock copolymer solution at pH 10.1.

Next, H_2PtCl_6 at a N/Pt = 3/1 molar ratio was added to the micellar copolymer solution and the pH dropped to 6.7. **Figure 3.35** shows the intensity autocorrelation functions for the metallated PHEGMA$_{50}$-*b*-PDEAEMA$_{50}$ diblock copolymer solution at various scattering angles. Two processes with diffusion coefficients $D_1 = 15.26 \times 10^{-7}$ cm^2/s, $D_2 = 3.01 \times 10^{-8}$ cm^2/s, corresponding to hydrodynamic radii $R_{h,1} = (4.1 \pm 0.2)$ nm and $R_{h,2} = (70 \pm 2)$ nm were obtained by DLS.

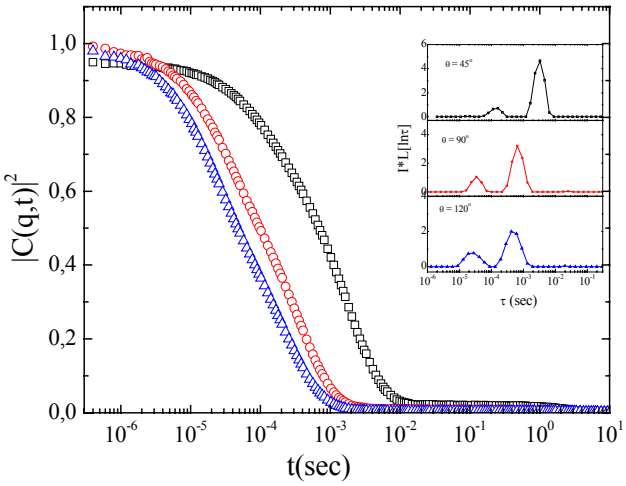

Figure 3.35 Intensity autocorrelation functions for a 0.33 wt% metallated (H_2PtCl_6) PHEGMA$_{50}$-*b*-PDEAEMA$_{50}$ diblock copolymer solution at pH 6.7 and scattering angle 45º (□), 90º (○) and 120º (△). Inset: distribution of relaxation times multiplied by the total scattering intensity (normalized to that of toluene).

The low intensity fast process (**Figure 3.36**) is attributed to the diffusion of single polymer chains, while the slow process is attributed to the diffusion of polymer aggregates, similar to those discussed in section 3.1.2 for non-metallated copolymer solutions at pH < 7. At first this result is expected since the platinic acid protonates the DEAEMA units of the polymer thus causing the destabilization of the micellar structures and the formation of unimers. However, upon a careful consideration of our data it is interesting to note that the metal-induced micellization, discussed above for polymer solutions at low pH in the presence of the metal precursors and attributed to the electrostatic interactions between the positively charged amine groups of the copolymer and the divalent metal anions is not observed in this sample. This is in contrast with the results obtained above for all metallated copolymer samples at low pH where a metal-induced micellization process was observed.

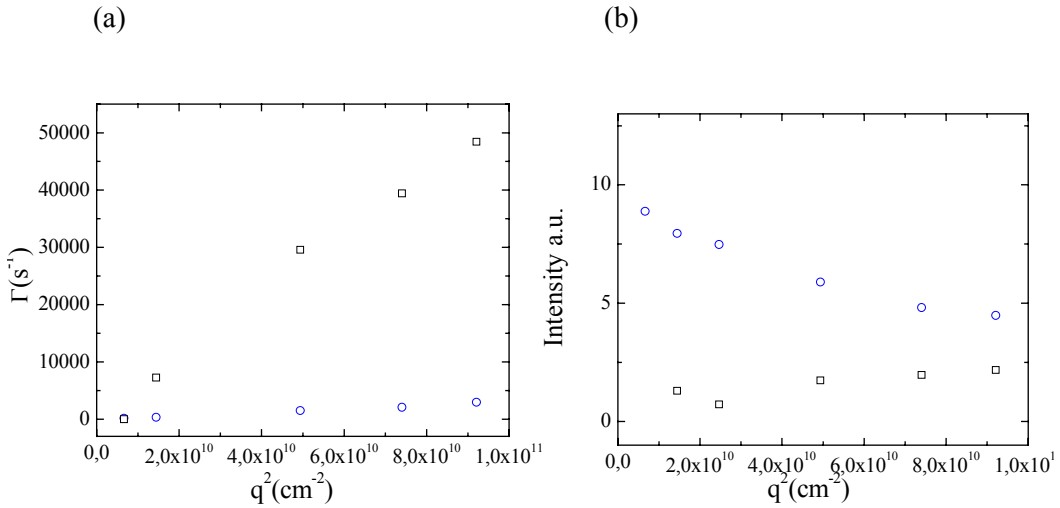

Figure 3.36 Wavevector dependence of a) the rates and b) the intensities of the fast (□) and the slow (○) process of a 0.33 wt% $PHEGMA_{50}$-*b*-$PDEAEMA_{50}$ diblock copolymer solution after the addition of H_2PtCl_6 at pH 6.7.

In an attempt to understand the above contradiction we examined the effect of the solution pH on the copolymer structure after addition of H_2PtCl_6 in a micellar copolymer solution. Thus the above method was repeated with a copolymer micellar solution of higher initial pH (~ 10.5). This resulted in a drop of the solution pH to a value above pH 7 upon addition of H_2PtCl_6.

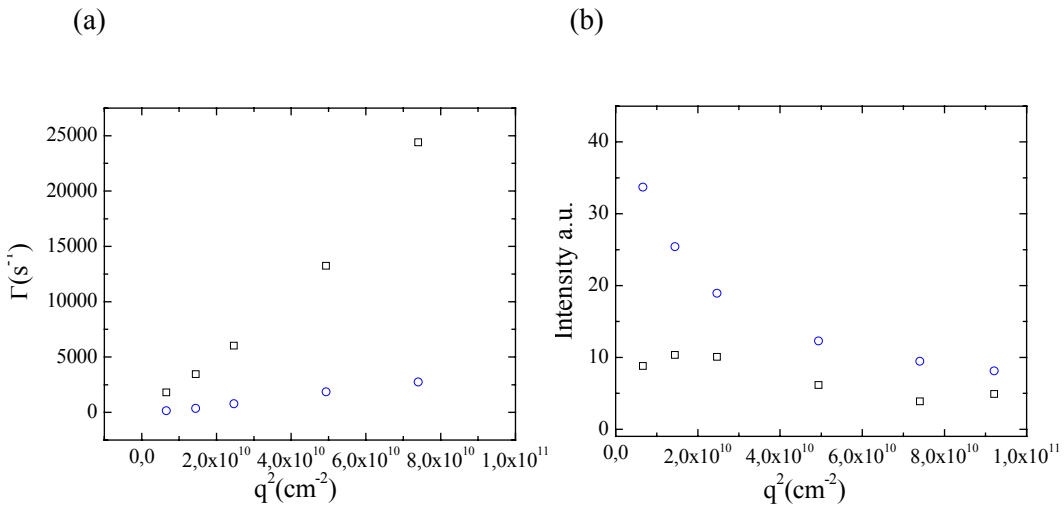

Figure 3.37 Wavevector dependence of a) the rates and b) the intensities of the fast (□) and the slow (○) process of a 0.33 wt% $PHEGMA_{50}$-*b*-$PDEAEMA_{50}$ diblock copolymer solution in the presence of H_2PtCl_6 at pH 7.2.

DLS study of this sample revealed two processes. **Figure 3.37** shows the q-depedence of the intensities and the rates of the two processes. From the Γ vs q^2 dependence the diffusivities $D_1 = 2.82 \times 10^{-7}$ cm^2/s and $D_2 = 3.28 \times 10^{-8}$ cm^2/s were calculated which correspond to hydrodynamic radii $R_{h,1} = (8.0 \pm 0.5)$ nm and $R_{h,2} = (65 \pm 2)$ nm respectively, while the q^2-dependent intensity of the slow process gives a radius of gyration $R_g = (70 \pm 4)$ nm.

The decrease in the hydrodynamic radius of the fast process from (12.0 ± 0.5) nm to (8.0 ± 0.5) nm is attributed to the partial protonation of the amine groups by the platinic acid, which results in the destabilization of the initial micelles and the detachment of free polymer chains from the micellar structure which thus becomes smaller. These free polymer chains are not observed by DLS due to their much lower scattering intensity in comparison with the high scattering intensity from the copolymer micelles. It is interesting to note that the presence of the metal precursor in the solution does not prohibit the decomposition of the micelles, as one might expect if a metal-induced micellization process took place, thus suggesting only weak polymer-metal interactions and the formation of loose polymer structures due to the remaining hydrophobic interactions between the non-protonated DEAEMA units. Moreover, extensive polymer aggregation is obtained for this sample as suggested by the high intensity of the slow process (**Figure 3.37**) attributed to possible polymer-metal interactions.

Next the sample was subjected to ultrafiltration to remove any hexachloroplatinate anions that have not been complexed by the polymer. This would allow to estimate the metal that has been complexed by the polymer and thus provide an indication of the polymer-metal interactions. DLS data for this sample showed two processes with diffusivities $D_1 = 4.12 \times 10^{-7}$ cm^2/s and $D_2 = 5.51 \times 10^{-8}$ cm^2/s corresponding to hydrodynamic radii $R_{h,1} = (5.2 \pm 0.2)$ nm and $R_{h,2} = (39 \pm 2)$ nm respectively. The observed decrease of the hydrodynamic radius of the fast process after ultrafiltration is attributed to the further decomposition of the loose structures discussed for the previous sample. This decomposition is accompanied by a decrease in the scattering intensity of the process (**Figure 3.38**). The small size and low intensity of this process are similar to those obtained for a non-metallated polymer solution at pH 2 and thus indicates the formation of single polymer chains in the solution. The second slow process has a size and intensity similar to the polymer

aggregates observed for low pH copolymer solutions. Furthermore, during ultrafiltration a change in the color of the sample from yellow to clear transparent is observed while the filtrate has a pale yellow color even after the third cycle suggesting that the metal is almost quantitatively removed and is not captured by the polymer.

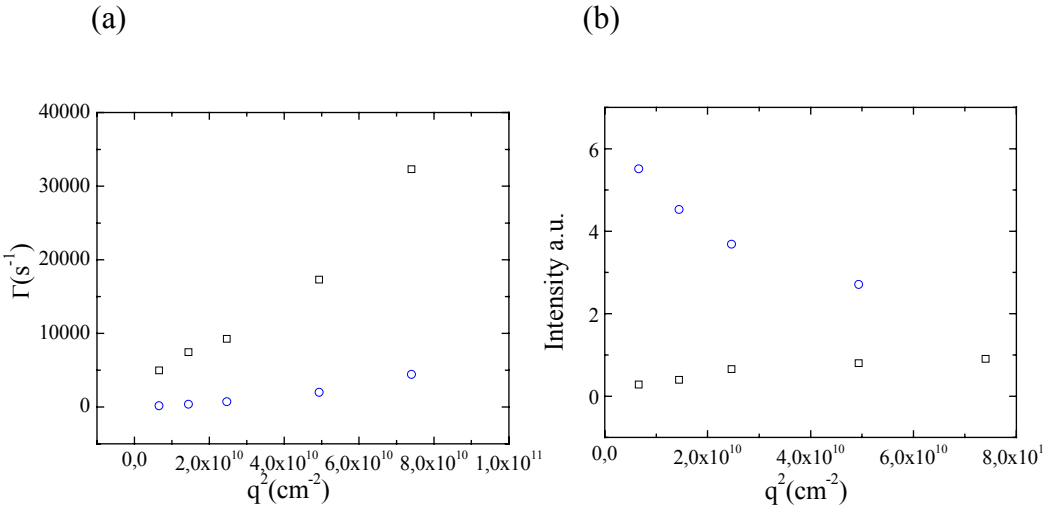

Figure 3.38 Wavevector dependence of a) the rates and b) the intensities of the fast (□) and the slow (○) process of a 0.33 wt% $PHEGMA_{50}$-*b*-$PDEAEMA_{50}$ diblock copolymer solution in the presence of H_2PtCl_6 and after ultrafiltration at pH 7.5.

Figure 3.39 shows the intensity autocorrelation functions for the metallated $PHEGMA_{50}$-*b*-$PDEAEMA_{50}$ diblock copolymer solutions at pH ~ 7.0, before and after ultrafiltration. The observed decrease in the size and the intensity of the fast process after ultrafiltration and the simultaneous change in the color of the polymer solution, suggest that the polymer is in its unimer state and no polymer-metal complexation takes place. These results again contradict our previous findings where a metal-induced micellization process was observed due to the electrostatic interactions of the metal anions and the charged single polymer chains at low pH.

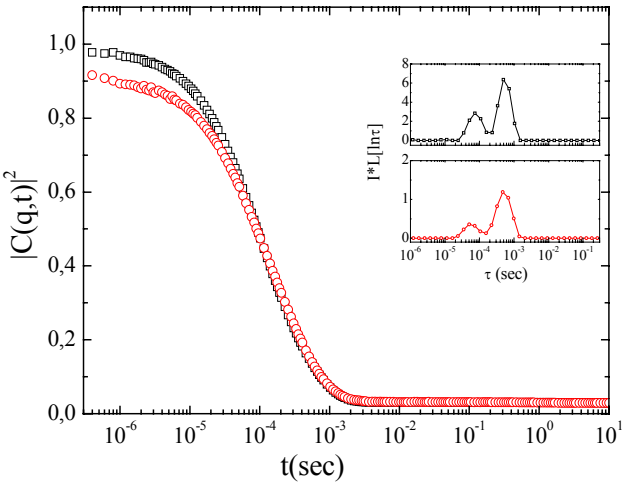

Figure 3.39 Autocorrelation functions of a 0.33 wt% PHEGMA$_{50}$-*b*-PDEAEMA$_{50}$ diblock copolymer solution in the presence of H_2PtCl_6 at 90º scattering angle, before ultrafiltration at pH 7.2 (□), and after ultrafiltration at pH 7.5. Inset: distribution of relaxation times multiplied by the total scattering intensity (normalized to that of toluene).

We next tried to elucidate this contradiction by investigating the effect of salt concentration on the metal-induced micellization process. For the polymer solutions at low pH where the metal-induced micellization process has been observed a salt free solution is used. However, the micellar copolymer solution at high pH at which the H_2PtCl_6 is added in Method B contains a certain amount of NaCl salt. Hence the presence of Na^+ and Cl^- ions in the copolymer solution upon metal addition is examined and its role in prohibiting the complexation between the $PtCl_6^{2-}$ anions and the positively charged amine groups, thus preventing metal-induced micellization is investigated.

NaCl salt was added in a 0.33 wt% PHEGMA$_{50}$-*b*-PDEAEMA$_{50}$ diblock copolymer solution in the presence of H_2PtCl_6 at pH 2.1. The final salt concentration in the solution was 0.012 M equal to the amount of salt formed when the pH of a 0.33 wt% polymer solution is increased from 2 to pH 10. Prior to salt addition, DLS study of the metallated sample revealed one process of high intensity and strong dynamics which dominates the correlation function. **Figure 3.40** illustrates the q-dependence of the intensity and the rate of this process. The diffusion coefficient D = 1.42x10^{-7}

cm^2/s of the process corresponds to a hydrodynamic radius R_h = (15 ± 0.5) nm and is attributed to the diffusion of metal-induced micelles as discussed previously.

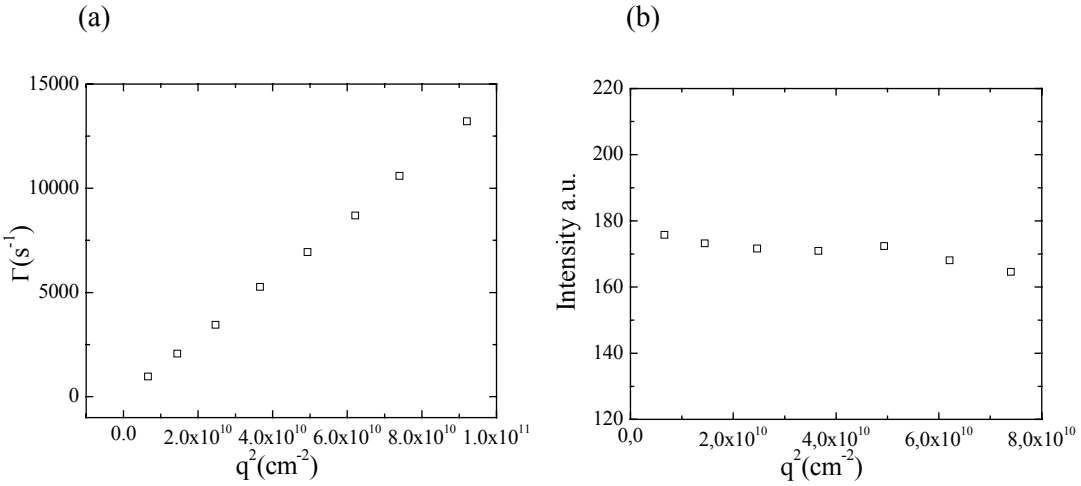

Figure 3.40 Wavevector dependence of a) the rate and b) the intensity of a 0.33 wt% $PHEGMA_{50}$-*b*-$PDEAEMA_{50}$ diblock copolymer solution after addition of H_2PtCl_6 at pH2.1.

Upon addition of NaCl (0.012 M) one process is again obtained with diffusion coefficient D = $1.42x10^{-7}$ cm^2/s corresponding to a hydrodynamic radius R_h = (14.5 ± 0.5) nm.

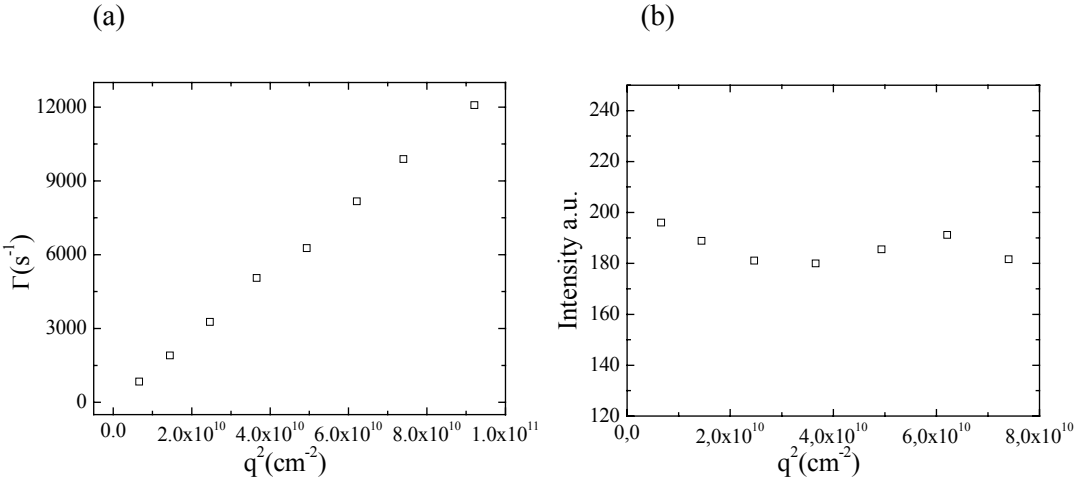

Figure 3.41 Wavevector dependence of a) the rate and b) the intensity of a 0.33 wt% $PHEGMA_{50}$-*b*-$PDEAEMA_{50}$ diblock copolymer solution in the presence of H_2PtCl_6 and after addition of 0.012 M NaCl at pH 2.1.

Both the size and the high intensity (**Figure 3.41**) of this process (which are similar to those observed before the addition of salt), signify that the salt did not cause the decomposition of the metal induced micelles to free polymer chains and thus had no effect on the electrostatic interactions between the metal anion and the positively charged DEAEMA units. This result indicates that the addition of salt in preformed metal-induced micelles cannot weaken the polymer-metal electrostatic interactions leading to micelle decomposition and the formation of free polymer chains.

In the next experiment the effect of the presence of salt before the addition of the metal precursor on the ability of the free polymer chains to associate with the metal anions upon the addition of the metal precursor was examined. Thus first salt at 0.012 M concentration was added in a 0.33 wt% $PHEGMA_{50}$-*b*-$PDEAEMA_{50}$ diblock copolymer solution at pH 2.3. DLS study of this sample revealed two processes of low intensity which are consistently obtained for polymer solutions at low pH (**Figure 3.42**); their diffusivities $D_1 = 5.84x10^{-7}$ cm^2/s and $D_2 = 1.82x10^{-8}$ cm^2/s correspond to hydrodynamic radii $R_{h,1}$ = (3.7 ± 0.2) nm and $R_{h,2}$ = (117 ± 2) nm respectively. The fast process is related to free polymer chains while the slow process is attributed to polymer aggregates as discussed previously.

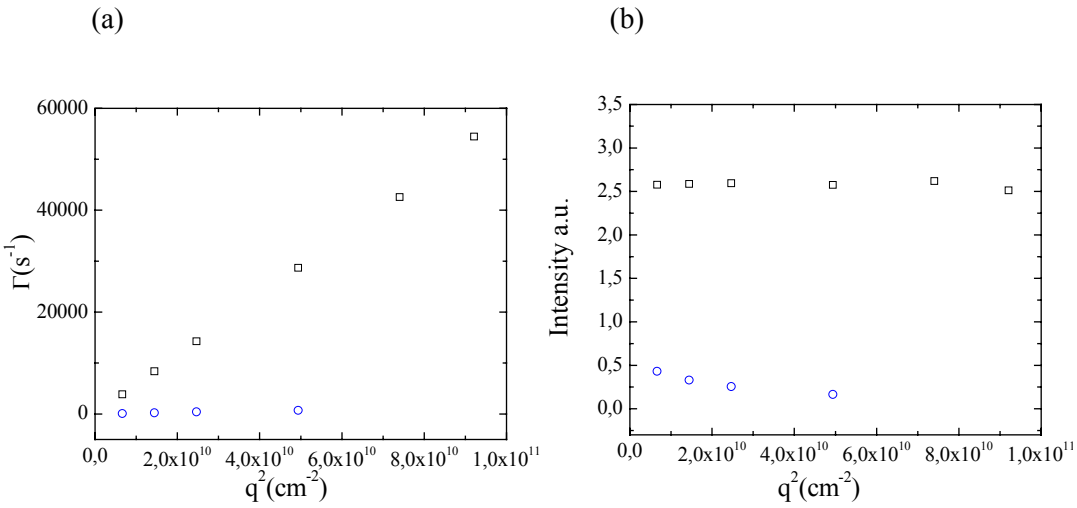

Figure 3.42 Wavevector dependence of a) the rates and b) the intensities of a 0.33 wt% $PHEGMA_{50}$-*b*-$PDEAEMA_{50}$ diblock copolymer solution upon addition of salt at pH 2.3.

H_2PtCl_6 at a N/Pt=3/1 molar ratio was then added in the above solution causing a further decrease of the solution pH to 2.1. For the metallated sample one

process with high intensity and with diffusion coefficient D = 1.75×10^{-7} cm^2/s corresponding to hydrodynamic radius R_h = (12.2 ± 0.5) nm was obtained by DLS (**Figure 3.43**). This process is attributed to the diffusion of metal-induced micelles, indicating that the presence of salt in a low pH polymer solution does not prohibit complexation between the $PtCl_6^{2-}$ anion and the positively charged amine groups and thus the formation of metal-induced micelles.

The above discussion indicates that the presence of salt at c = 0.012 M in solution has no effect on the polymer-metal electrostatic interactions and thus further studies are required to elucidate the contradiction between the metal-induced micelles formed at low pH and the existence of free polymer chains upon metal incorporation in a micellar copolymer solution.

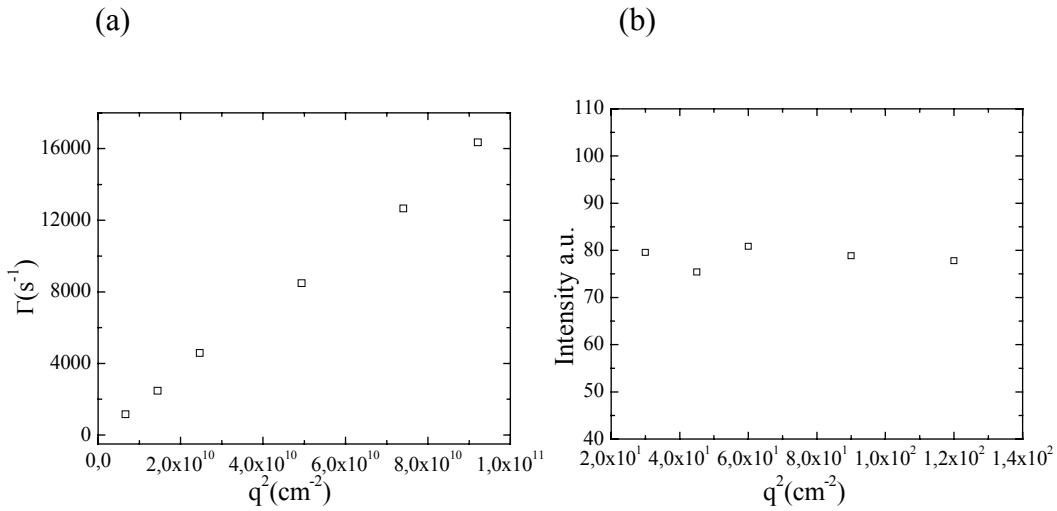

Figure 3.43 Wavevector dependence of a) the rate and b) the intensity of a 0.33 wt% $PHEGMA_{50}$-*b*-$PDEAEMA_{50}$ diblock copolymer solution in the presence of 0.012 M NaCl and after addition of H_2PtCl_6 at pH 2.1.

3.2.3.2 Potassium Hexachloroplatinate (K_2PtCl_6)

The effect of the addition of K_2PtCl_6 in a micellar copolymer solution was also investigated. K_2PtCl_6 is a salt and cannot cause protonation of the DEAEMA units. Thus metal incorporation can only occur due to the possible coordination of the metal precursor with the tertiary amine groups of the polymer via the electron pair on the nitrogen atom. The effect of K_2PtCl_6 addition was studied by DLS. K_2PtCl_6 at a N/Pt=3/1 molar ratio was added in a 0.33 wt% micellar $PHEGMA_{50}$-*b*-$PDEAEMA_{50}$

diblock copolymer solution at pH 8.5. The solution was stirred for 5 days to allow for metal complexation to occur and ultrafiltration followed. The autocorrelation function for this sample depicted two processes with diffusion coefficients $D_1 = 1.93 \times 10^{-7}$ cm^2/s and $D_2 = 2.79 \times 10^{-8}$ cm^2/s corresponding to hydrodynamic radii $R_{h,1} = (11.0 \pm 0.5)$ nm and $R_{h,2} = (77 \pm 2)$ nm respectively. The wavevector dependence of the intensities and the rates of the two processes are shown in **Figure 3.44**.

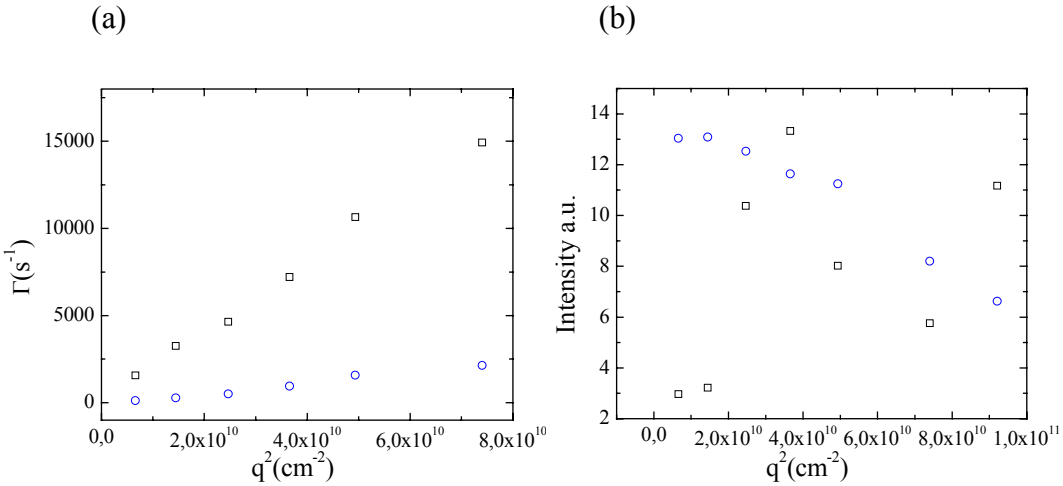

Figure 3.44 Wavevector dependence of a) the rates and b) the intensities of the fast (□) and the slow (○) process of a 0.33 wt% $PHEGMA_{50}$-*b*-$PDEAEMA_{50}$ diblock copolymer solution in the presence of K_2PtCl_6 and after ultrafiltration at pH 8.5.

At this pH the DEAEMA units of the copolymer are deprotonated and thus the fast process observed in the autocorrelation function is attributed to the diffusion of micelles formed by the hydrophobic PDEAEMA blocks and stabilized by the PHEGMA hydrophilic blocks. The slow process corresponds to the diffusion of micellar aggregates discussed previously in section 3.1. We should also note the large fluctuations of the intensity of the fast process which are consistently observed for high pH metallated samples. Furthermore, during ultrafiltration a change in the color of the sample from yellow to clear transparent was observed suggesting the absence of efficient polymer-metal interactions and thus indicating that metal incorporation is very low.

Metal reduction resulted in a slight increase of the solution pH to 8.7. However, the color of the solution was black-grey in contrast to the dark black color

obtained upon metal reduction for the samples containing K_2PtCl_6 at low pH suggesting little metal incorporation. DLS measurement of a 3-fold diluted sample showed again the existence of two processes in the correlation function (**Figure 3.45**); their diffusivities $D_1 = 1.56 \times 10^{-7}$ cm^2/s and $D_2 = 2.15 \times 10^{-8}$ cm^2/s correspond to hydrodynamic radii $R_{h,1} = (13.8 \pm 0.5)$ nm and $R_{h,2} = (100 \pm 2)$ nm respectively. The fast process is attributed to the diffusion of polymer micelles formed by the hydrophobic PDEAEMA blocks at high pH values, while the slow process corresponds to the diffusion of micellar aggregates.

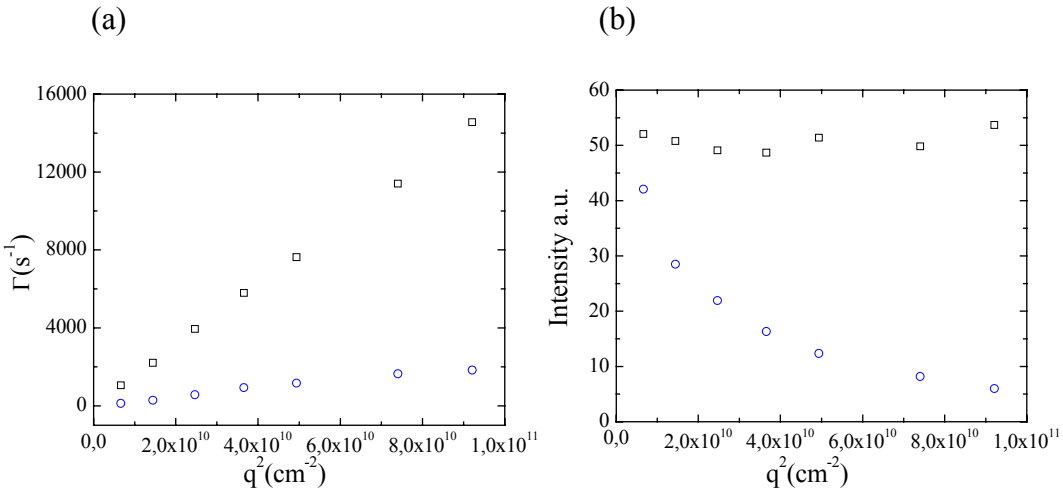

Figure 3.45 Wavevector dependence of a) the rates and b) the intensities of the fast (□) and the slow (○) process of a 0.1 wt% $PHEGMA_{50}$-*b*-$PDEAEMA_{50}$ diblock copolymer solution (+ K_2PtCl_6) after metal reduction at pH 8.7.

Figure 3.46 shows the intensity autocorrelation functions for the metallated (K_2PtCl_6) $PHEGMA_{50}$-*b*-$PDEAEMA_{50}$ diblock copolymer solution at high pH, before and after metal reduction at 90º scattering angle.

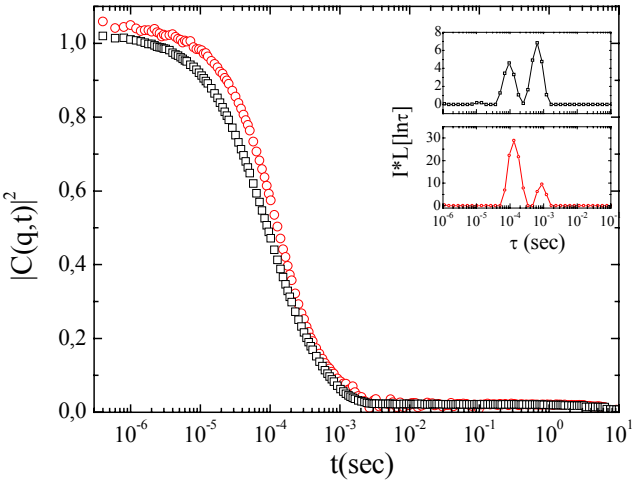

Figure 3.46 Autocorrelation functions of a $PHEGMA_{50}$-*b*-$PDEAEMA_{50}$ diblock copolymer solution at 90º scattering angle, in the presence of K_2PtCl_6 and after ultrafiltration at pH 8.5 and c =0.33 wt% (□), the same sample after metal reduction at pH 8.7 and c =0.1 wt% (○). Inset: distribution of relaxation times multiplied by the total scattering intensity (normalized to that of toluene).

Summarizing Method B, addition of H_2PtCl_6 in a micellar diblock copolymer solution at high pH leads to the partial protonation of the amine groups by the platinic acid and therefore to the detachment of free polymer chains from the micellar structure. In addition, it is unclear why metal-induced micellization due to electrostatic interactions between the positively charged amine groups of the copolymer and the divalent metal anions is not observed. Furthermore, for the K_2PtCl_6, metal incorporation at high pH is very low suggesting that metal incorporation via coordination is not effective and thus Method B is not appropriate for metal nanoparticle formation within the cores of the micelles.

3.2.4 NMR studies

Proton NMR spectroscopy has been used to investigate the effect of metallation on the properties of the polymeric matrix and to elucidate the polymer-metal interactions. Proton NMR spectra of the samples for all steps of metallation and metal reduction were obtained using both metallation Method A and Method B. **Figure 3.47** shows the ^1H NMR spectra of all samples during metallation Method A.

At α = 2 the DEAEMA units are all protonated and thus hydrophilic, the polymer is fully soluble in the aqueous medium and thus the corresponding peaks of the protons of both blocks appear in the NMR spectrum of the polymer. Upon addition of the metal precursor the disappearance of the peaks attributed to the protons of the PDEAEMA block confirms the metal-amine complexation discussed above for the light scattering data which results in the metal induced micellization and the immobilization of the DEAEMA groups within the micellar core. It is worth noting that all DEAEMA peaks completely disappear (apart from that attributed to the two methyl groups at 1.4 ppm which has however a much lower intensity) suggesting the complete dehydration of the cores of the metal-induced micelles and the formation of dense micellar structures. This might at first seem surprising considering that these micellar cores comprise ionic charged species but can be better understood as a process analogous to the charge neutralization of the proteins at their isoelectric point which results in their complete dehydration and thus precipitation from an aqueous solution. For the spectrum after metal reduction at low pH the peaks due to the protons of the PDEAEMA block appear again in the spectrum of the reduced sample, suggesting the solvation of both blocks of the copolymer. This reappearance of the DEAEMA peaks, and hence the complete solubility of our copolymer upon metal reduction is consistent with our DLS studies (section 3.2.2.1) which revealed one process of low intensity and with smaller hydrodynamic radius than that obtained for the metal-induced micelles. This process was attributed to the diffusion of loose structures arising from only weak interactions between the reduced metal and the charged polymer and suggested the decomposition of the metal-induced micelles upon metal reduction, which leads to the solubility of the protonated PDEAEMA block at pH ~ 2 as verified by NMR.

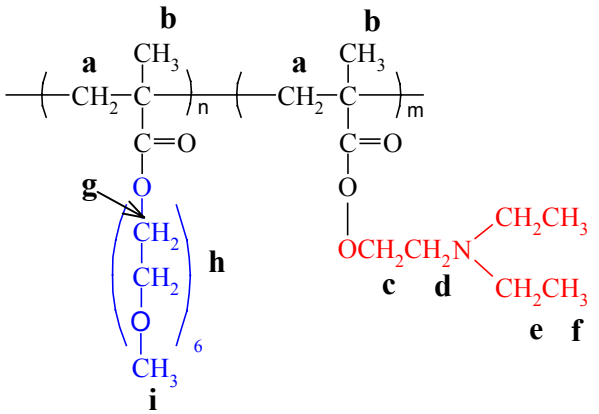

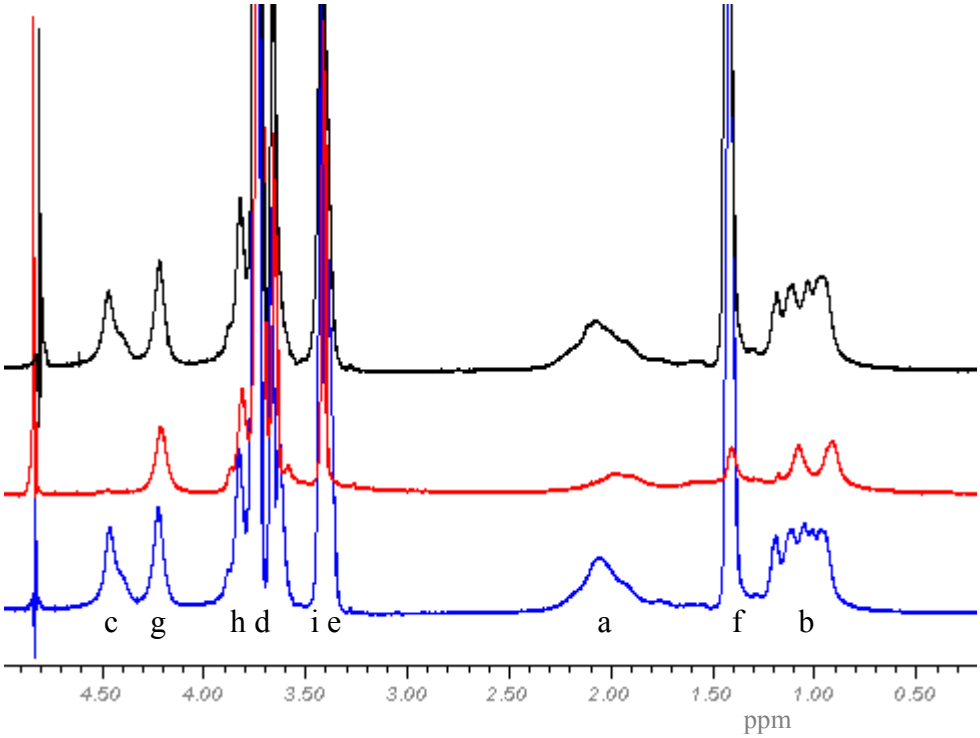

Figure 3.47 ^{1}H NMR spectra for all steps of polymer metallation using Method A. A 2 wt% $PHEGMA_{50}$-*b*-$PDEAEMA_{50}$ diblock copolymer solution at α = 2 (—), the polymer solution in the presence of H_2PtCl_6 at a N/Pt = 3/1 molar ratio (—) and the reduced sample at α = 2 (—).

The second method (Method B) of metallation was also followed by ^{1}H NMR. **Figure 3.48** shows the ^{1}H NMR spectra of a c = 2 wt% $PHEGMA_{50}$-*b*-$PDEAEMA_{50}$ diblock copolymer solution at α = 0, the solution in the presence of H_2PtCl_6 at a N/Pt = 3/1 molar ratio and the reduced sample at α = 0. At α = 0 the DEAEMA units are deprotonated and thus hydrophobic and micelles are formed in the aqueous medium (as discussed previously for the DLS data) resulting in the disappearance of the peaks due to the protons of the PDEAEMA blocks which form the micelle core. Upon addition of H_2PtCl_6, the spectrum is similar to that obtained for α = 0 where only the peaks due to the PHEGMA block appear in the spectrum, although one would possibly expect the re-appearance of the DEAEMA peaks due to the protonation of the DEAEMA units by the protons of the added platinic acid. Moreover, DLS studies revealed that metal-induced micellization does not occur upon addition of the platinic acid in a micellar copolymer solution (section 3.2.3.1) and the polymer exists rather as unimers which should be fully soluble and thus both blocks should appear in the NMR spectrum. However, it is worth noting that the metallation process was studied

by DLS as a function of the solution pH, while NMR studies of metallation were performed as a function of the degree of protonation of the amine groups. It is thus possible that the DEAEMA units are charged to a different extent for the two samples and it is not clear from the present study whether the disappearance of the peaks of PDEAEMA is due to hydrophobic interactions of the amine groups or due to polymer-metal interactions leading to the insolubility of PDEAEMA in the aqueous medium. Further metallation studies are required employing Method B as a function of the degree of protonation of the amine groups to elucidate these results. Finally, after metal reduction the peaks corresponding to the PDEAEMA blocks are again not observed in the spectrum, as expected for $\alpha = 0$.

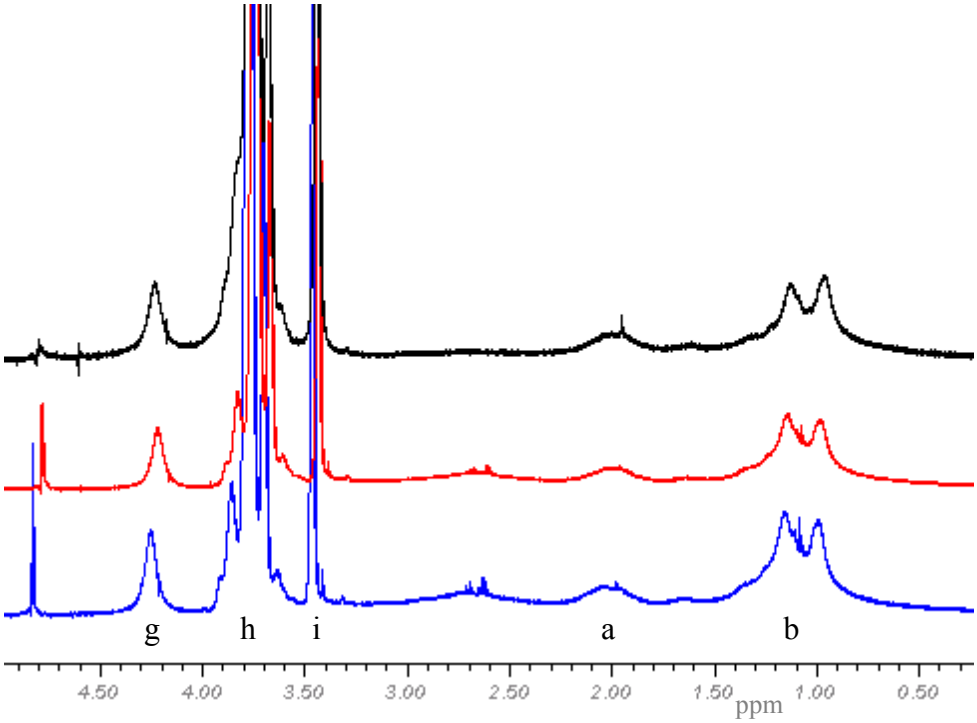

Figure 3.48 ^{1}H NMR spectra for all steps of metallation using Method B. A 2 wt% $PHEGMA_{50}$-*b*-$PDEAEMA_{50}$ diblock copolymer solution at $\alpha = 0$ (—), the polymer solution in the presence of H_2PtCl_6 at a N/Pt = 3/1 molar ratio (—) and the reduced sample at $\alpha = 0$.

3.2.5 TEM

The characteristics of the micelles formed upon metallation using Method A as well as the metal nanoparticle formation after metal reduction were also studied by TEM. H_2PtCl_6 was added in a 0.1 wt% $PHEGMA_{50}$-*b*-$PDEAEMA_{50}$ diblock

copolymer solution at pH 2 at a molar ratio N/Pt=3/1, followed by ultrafiltration. Dilution of the sample to a final polymer concentration of 0.075 wt% was carried out next to avoid extensive polymer aggregation. Metal-induced micelles were formed in this solution as verified earlier by DLS and ^{1}H NMR spectroscopy, with the Pt species being incorporated within the micelle cores and thus providing the necessary contrast for TEM visualization of these structures. **Figure 3.49a** shows both spherical micelles, and the micellar aggregates formed in the metallated sample.

(a) (b)

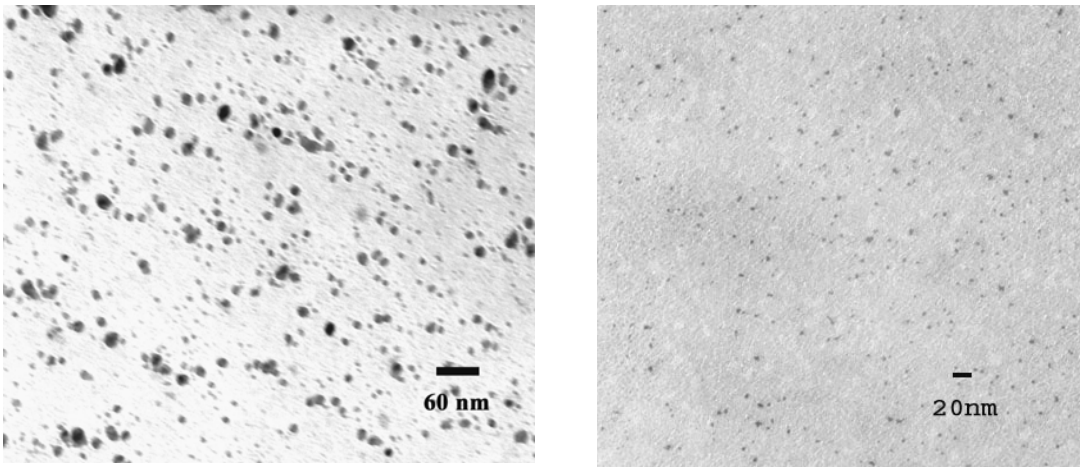

Figure 3.49 TEM images of a) the diblock $PHEGMA_{50}$-*b*-$PDEAEMA_{50}$ copolymer micelles after incorporation of H_2PtCl_6 at N/Pt=3/1 molar ratio and b) the Pt nanoparticles after metal reduction.

The size of the micelles seems lower than the micellar size (30 nm) measured earlier by DLS (section 3.2.2.1 and 3.2.2.2). This can be explained as both an effect of the two-dimensional imaging in TEM rather than the 3-D objects measured by DLS, but even more important in TEM we are only visualizing the compact micellar cores which have the appropriate contrast due to the presence of the platinic compound while DLS gives the hydrodynamic size of the whole micellar structure, which also includes the corona of the micelle. Metal reduction using $NaBH_4$ and addition of NaOH leads to the formation of the metal nanoparticles inside the micellar cores which are illustrated in **Figure 3.49b.** The contrast between the nanoparticles formed

within the micelles and the polymeric material is so high that the micelles become invisible. The size of the nanoparticles was estimated by TEM to be around 5nm.

3.2.6 UV/Vis studies of metallation

The polymer behavior and in particular the polymer-metal interactions upon metal precursor incorporation and after metal reduction were also studied by UV/Vis spectroscopy. UV/Vis spectra were obtained for both metallation processes (Method A and Method B), using either H_2PtCl_6 or K_2PtCl_6 as metal precursors. **Figure 3.50** illustrates the UV/Vis spectra for a 0.0025 wt% $PHEGMA_{50}$-*b*-$PDEAEMA_{50}$ diblock copolymer solution at pH 2 in the presence of H_2PtCl_6 at a N/Pt = 3/1 molar ratio and the same sample after metal reduction at pH 10. We should note the appearance of a peak at 266 nm for the H_2PtCl_6 containing polymer solution at low pH. This peak does not appear neither in spectrum of the pure polymer in water at the same pH nor when H_2PtCl_6 is dissolved in pure water, and thus is attributed to the interaction between the $PtCl_6^{2-}$ anions and the protonated amine groups of the polymer [9]. This result is consistent with the metal-amine complexation and the metal-induced micellization found earlier by DLS and ^{1}H NMR studies and are now also confirmed by our UV/Vis measurements. After reduction, the total disappearance of the peak confirms the complete metal reduction and the elimination of the metal-polymer interactions, which is also in good agreement with our DLS and ^{1}H NMR results. In the inset we observe the peak at 266 nm for three different N/Pt molar ratios 3/1, 2/1 and 1/1. It is obvious that the absorption increases linearly for the N/Pt=3/1 and 2/1 molar ratios, while for N/Pt=1/1 only a slight increase in the absorption is observed. This is expected since the protonated amines are monovalent, while the metal anions are divalent. Thus, for charge neutralization a saturation point at N/Pt=2/1 is reached and very little further metal complexation takes place upon increasing the amount of added metal to N/Pt = 1/1.

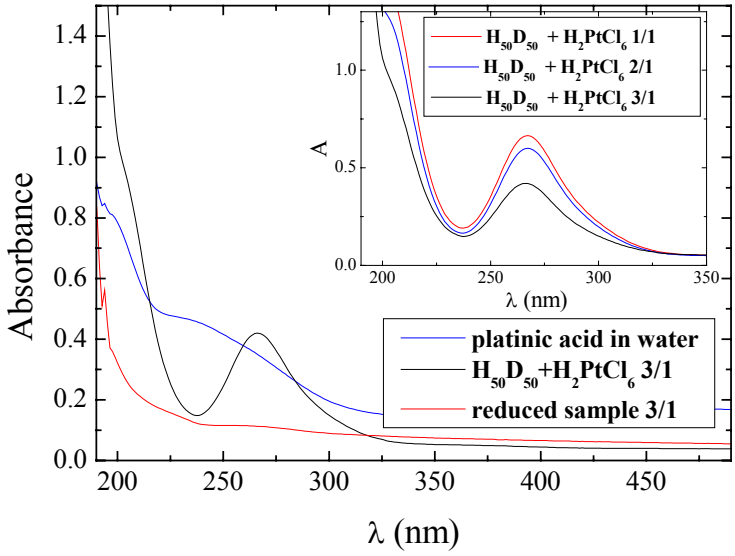

Figure 3.50 UV/Vis spectra for 0.0025 wt% $PHEGMA_{50}$-*b*-$PDEAEMA_{50}$ diblock copolymer solutions; in the presence of H_2PtCl_6 at N/Pt=3/1 and pH 2 (—), the reduced sample at pH 10 (—). A 0.0025 wt% solution of H_2PtCl_6 in pure water is also shown (—).

Next, in order to examine the effect of the nature of the metal precursor (acid *vs* salt) on the polymer-metal interactions, K_2PtCl_6 was added to a 0.0025 wt% $PHEGMA_{50}$-*b*-$PDEAEMA_{50}$ diblock copolymer solution in its unimer state at low pH. **Figure 3.51** shows the UV/Vis spectra for the $PHEGMA_{50}$-*b*-$PDEAEMA_{50}$ diblock copolymer solution in the presence of K_2PtCl_6 at a N/Pt = 1/1 molar ratio and the sample after metal reduction at pH 10. Similar to the results for H_2PtCl_6 discussed above, the characteristic peak at 266 nm is observed for the metallated sample, signifying the electrostatic interaction between the divalent $PtCl_6^{2-}$ anions and the positively charged amine groups of the polymer. These results were also verified earlier by DLS (section 3.2.2.3) where a similar metal-induced micellization was observed upon addition of K_2PtCl_6 in a polymer solution at pH 2. Furthermore, this peak completely disappears again in the reduced sample suggesting that metal reduction is quantitative.

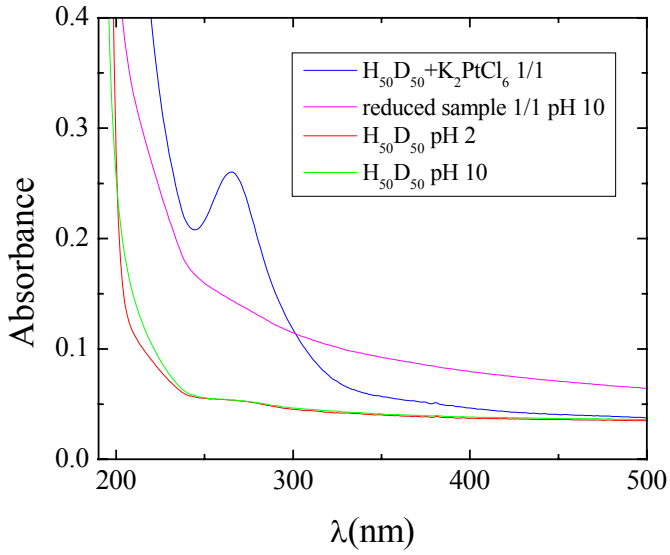

Figure 3.51 UV/Vis spectra for a 0.0025 wt% PHEGMA$_{50}$-*b*-PDEAEMA$_{50}$ diblock copolymer solution at pH 2 (—) and pH 10 (—), the same polymer solution in the presence of K_2PtCl_6 at N/Pt =1/1 and pH 2 (—) and the reduced sample at pH10 (—).

Finally, the polymer-metal interactions using metallation Method B, which involves metal incorporation in a polymer solution at high pH, were examined. K_2PtCl_6 was introduced in a 0.0025 wt% micellar PHEGMA$_{50}$-*b*-PDEAEMA$_{50}$ diblock copolymer solution. In accordance to our previous studies [2], the solution was left stirring for 5 days to allow for polymer metal complexation to take place due to coordination of the nitrogen atom of the amine groups of the polymer to the metal atoms. **Figure 3.52** illustrates the UV/Vis spectra for the PHEGMA$_{50}$-*b*-PDEAEMA$_{50}$ diblock copolymer solution at high pH in the presence of K_2PtCl_6 at a N/Pt = 1/1 molar ratio and the same sample after metal reduction. The peak at 266 nm discussed above is not observed in the K_2PtCl_6 containing polymer solution, indicating the absence of interactions between the polymer and the metal species at this high pH. This result is consistent with our previous DLS studies, where no effect on the polymer structure upon addition of the platinic salt at high pH (section 3.2.3.2) was found while the metal was removed by ultrafiltration suggesting that no metal incorporation takes place.

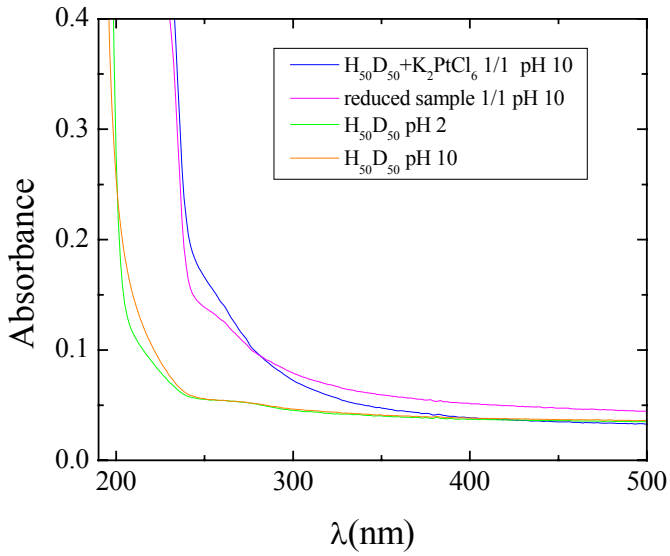

Figure 3.52 UV/Vis spectra for a 0.0025 wt% PHEGMA$_{50}$-*b*-PDEAEMA$_{50}$ diblock copolymer solution at pH 2 (—) and pH 10 (—), the same solution in the presence of K_2PtCl_6 at N/Pt =1/1 and pH 10 (—) and the reduced sample at pH 10 (—).

3.2.7 X-Ray diffraction studies of the metal nanoparticles

X-Ray diffraction has been used to investigate the metal nanoparticle characteristics after metal reduction. **Figure 3.53** shows the XRD spectra for the pure PHEGMA$_{50}$-*b*-PDEAEMA$_{50}$ diblock copolymer, the polymer in the presence of H_2PtCl_6 and the reduced samples for N/Pt = 3/1 and 1/1 using Method A for metal incorporation. The broad peak at θ ~ 20º observed in all spectra, is attributed to the polymer structure. The sharper peaks obtained in the reduced samples at 40º, 46º, 67.5º, 81º, 85.5º, 103.5º are characteristic of the crystal structure of platinum, signifying the formation of metal nanocrystals within cores of the polymer micelles. From the FWHM the size of the nanocrystals was calculated to be ~ 3.5 nm for both N/Pt = 3/1 and 1/1 molar ratios suggesting that the metal loading does not have a significant effect on the size of the final metal nanoparticles formed, at least for the loading ratios used in the present study. It is worth noting that even for such small particle sizes the metal nanoparticles formed within the cores of the polymer micelles, exhibit an ordered crystalline structure that could have certain advantages for many

applications such as those related to the preparation of magnetic or photonic materials. The platinum metal nanoparticles prepared within the polymeric micelles in this study have been shown to have significantly enhanced catalytic properties in hydrogenation and oxidation reactions, which are intermediate steps in the production of vitamins A, C and E.

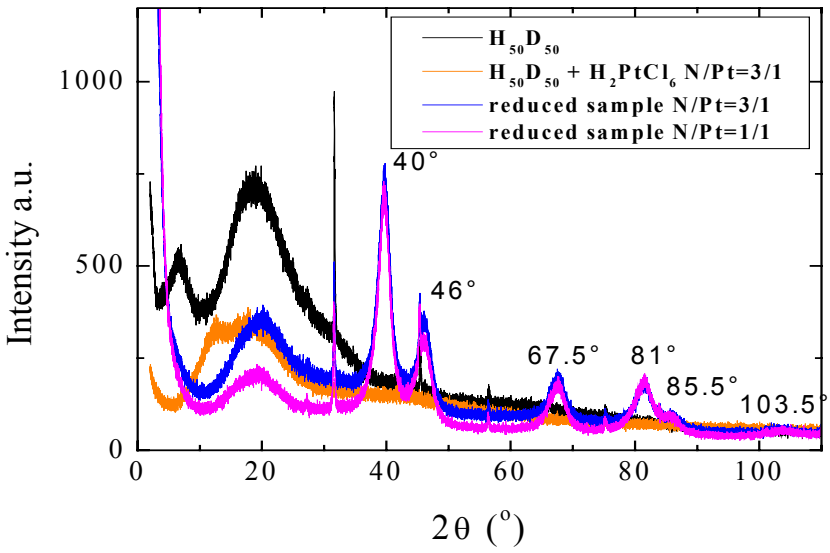

Figure 3.53 XRD spectra for the $PHEGMA_{50}$-*b*-$PDEAEMA_{50}$ diblock copolymer (—), the polymer in the presence of H_2PtCl_6 (—) and the reduced samples for N/Pt = 3/1(—) and 1/1(—). Metallation was carried out using Method A.

3.3 pH responsive microgels

3.3.1 DLS studies

In the present work the aqueous solution properties of pH-responsive PDEAEMA microgel particles were also investigated. The change in the hydrodynamic diameter of the microgel particles when altering the solution pH was followed by dynamic light scattering. **Figure 3.54** shows the autocorrelation functions of a 0.05 wt% PDEAEMA microgel solution in water for two different pH values 2 and 7. For the sample at pH 7 one process with very strong intensity and dynamics dominates the autocorrelation functions. From the corresponding inverse laplace transformation (see inset) a hydrodynamic radius R_h = (111 ± 2) nm was calculated.

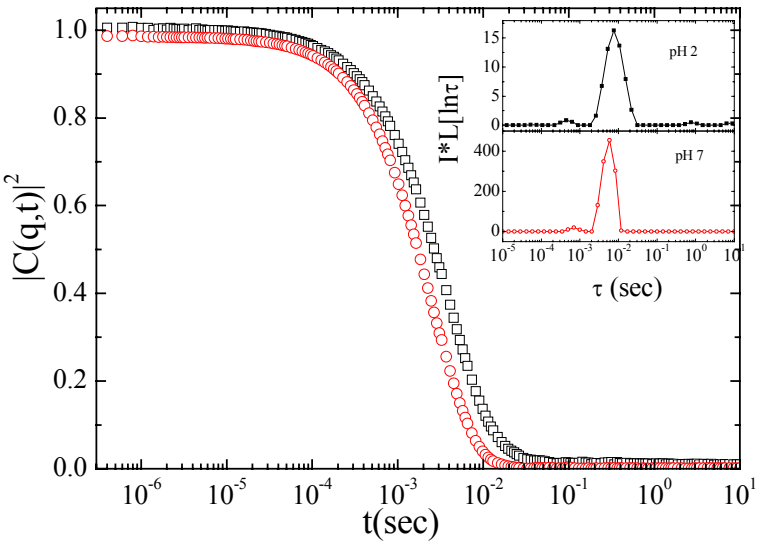

Figure 3.54 Intensity autocorrelation functions of a 0.05 wt% PDEAEMA microgel solution at 45° scattering angle for pH 2 (□) and pH 7 (○). Inset: distribution of relaxation times multiplied by the total scattering intensity (normalized to that of toluene).

At this pH value (≥7) the DEAEMA units are deprotonated and thus hydrophobic, resulting in the formation of compact (high contrast) PDEAEMA latex particles in the aqueous medium. However, for the sample at pH 2 a sharp decrease in the scattering intensity is observed while the hydrodynamic size calculated by DLS was found to increase to (180 ± 2) nm. This swelling of the particles is attributed to the protonation of the tertiary amine units at low pH (< 7), which become hydrophilic and thus allow water to enter into the microgel particles (**Figure 3.55**).

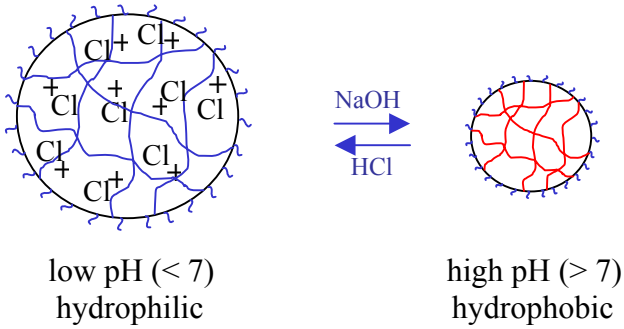

Figure 3.55 Schematic representation of the swelling-deswelling process at low and high pH.

The above is a fully reversible process, which means that one can obtain again the hydrophobic latex particles by increasing the solution pH above 7 with NaOH. It should also be mentioned that this swelling process is accompanied by a change in the turbidity of the sample from milky-white in alkaline media to clear transparent at low pH values. Furthermore, addition of base in an acidic transparent solution induces an increase in the turbidity suggesting the reversibility of the swelling-deswelling process. Due to the turbidity of the sample at high pH all DLS measurements were performed at low microgel concentration (0.05 wt%) in order to avoid undesired light absorption during the experiment.

3.4 Metallated microgel particles

3.4.1 General

The formation of colloidal metal nanoparticles in polymer microgel matrices was also examined. **Figure 3.56** shows a schematic representation of the procedure

followed for the formation of metal particles in the nanometer size range, within the polymer microgels. This procedure is very similar to that described above for the metallation of the diblock copolymer micelles.

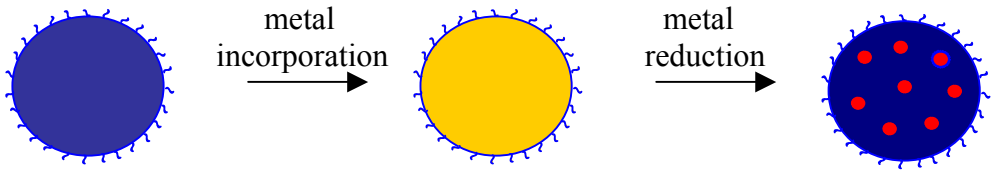

Figure 3.56 Schematic representation of metal nanoparticle formation within microgel particles.

The metal particles formed within the microgel matrices are expected to have improved catalytic behavior as compared to those formed within the polymer micelles. The reason for this is the higher metal loading of the microgels due to their higher amine content. Besides, the microgel catalyst matrices retain their colloidal stability over the whole pH range due to the presence of permanent chemical crosslinks, between the PDEAEMA chains, in contrast to the polymer micelles that can break apart for pH values below 7 when the DEAEMA units in the micelle core become protonated and thus hydrophilic.

The formation of metal nanoparticles within the microgel particles was studied by dynamic light scattering and UV/Vis spectroscopy, while their nanoparticle structure and size was investigated by X- Ray diffraction. The metallated microgel particles and the metal nanoparticle characteristics were also studied by TEM, while TGA was used to access the microgel metal content.

3.4.2 DLS studies

Two methods were used for the metallation of the microgel particles. In the first method an as synthesized microgel solution at pH 7.3 was first diluted to a concentration c = 0.05 wt%. Next $H_2PtCl_6 \cdot 6H_2O$ was added at a N/Pt=3/1 molar ratio and the pH dropped to 4.7. The solution was left stirring for 24 h in order to reach equilibrium. Finally, metal reduction took place upon addition of an excess amount of $NaBH_4$ and the pH increased again to 7. The above procedure was followed by DLS

to determine the effect of metal incorporation and metal reduction on the characteristics of the microgel particles (**Figure 3.57**). For the platinic acid containing microgel sample a 10-fold dilution was carried out before being analyzed by DLS in order to avoid the absorbance due to its dense yellow color. The reduced sample was also diluted before analysis because its measurement at c=0.005 wt% concentration was prohibited due to its high absorbance. Some absorbance (~ 10%) was observed even at c=0.001 wt% which however did not impend significantly the DLS experiment.

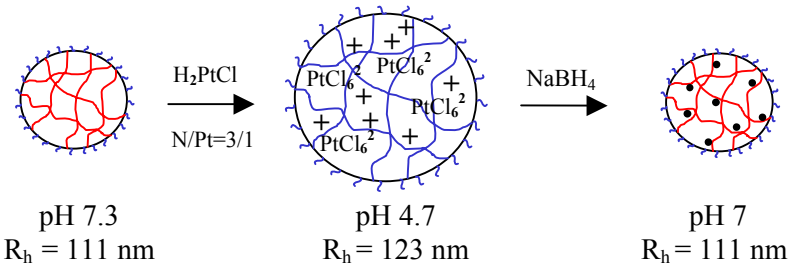

Figure 3.57 Schematic representation of metal nanoparticle formation within microgel particles at pH 7.

Figure 3.58 shows the intensity autocorrelation functions C(q,t) and the corresponding inverse laplace transformations at 60º scattering angle of a microgel solution at 0.05 wt % and pH = 7.3, the metallated microgel solution at 0.005 wt% and pH = 4.7 and the reduced sample at 0.001 wt% and pH = 7. From the distributions of relaxation times the respective hydrodynamic sizes were calculated.

For the microgel at 0.05 wt% and pH 7.3 one process dominates the autocorrelation functions with very strong intensities and dynamics that correspond to a hydrodynamic radius R_h = (111 ± 2) nm (see inset). This is attributed to the non-metallated latex particles comprising hydrophobic PDEAEMA chains.

After addition of the H_2PtCl_6 in the microgel aqueous solution the scattering intensity increases sharply while the hydrodynamic radius of the microgel particles increased only slightly from (111 ± 2) nm to (123 ± 2) nm for the metallated sample as found by DLS. In order to explain this small increase in the size of the metal-containing particles we should consider the two opposing effects that take place. First, the addition of an acid to the PDEAEMA particles which protonates the tertiary amine

groups, render them hydrophilic and cause the particles swell. However, one should expect that the size of the metallated microgel particles should thus reach 180 nm, as we discussed earlier for the addition of HCl and the protonation of the PDEAEMA units at low pH (section 3.3.1). In order to explain this result, which appears to conflict our earlier findings one should consider what happens after the addition of H_2PtCl_6 in a low pH solution of our previous system, the double-hydrophilic diblock copolymers. There, we observed metal-induced micellization due to complexation of the $PtCl_6^{-2}$ anions with the protonated amine groups of the polymer. A similar effect takes place for the microgel particles, causing the condensation of the protonated amines by the divalent metal anions, thus preventing extensive swelling of the particles. Finally, reduction of the metal with $NaBH_4$ causes the solution pH to increase again above the p*K*a of the protonated PDEAEMA and the hydrodynamic radius of the metal nanoparticle containing microgel particles to decrease to 111 nm, which is similar to the size of the non-metallated PDEAEMA latex particles at high pH.

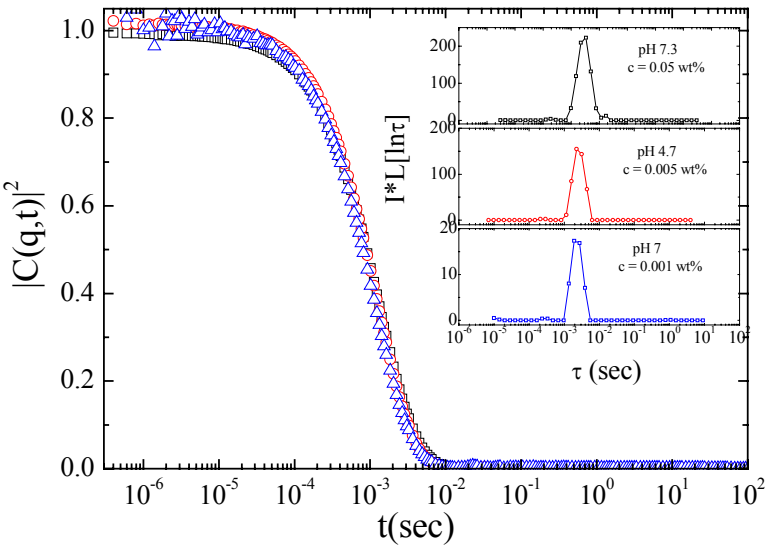

Figure 3.58 Intensity autocorrelation functions of a microgel solution at 60º scattering angle; at 0.05 wt% and pH = 7.3 (□), the metallated (H_2PtCl_6) microgel solution at 0.005 wt% and pH = 4.7 (○), the reduced sample at 0.001 wt% and pH = 7 (△). Inset: distribution of relaxation times multiplied by the total scattering intensity (normalized to that of toluene).

In the second method used for the metallation of the microgel particles a microgel solution at c=0.05 wt% was first taken to pH 2.3. Next $H_2PtCl_6 \cdot 6H_2O$ was added at a N/Pt=3/1 molar ratio and the pH dropped to 2. After stirring for 24 h metal reduction with $NaBH_4$ was carried out and the solution was stirred for another half an hour, before increasing again the pH to 9 with NaOH, followed by stirring for 24 h (**Figure 3.59**). Metallated samples and metal nanoparticle containing microgel solutions were first subjected to a 10-fold and an additional 5-fold dilution respectively before being measured by DLS in order to avoid the high light absorbance by the colored samples.

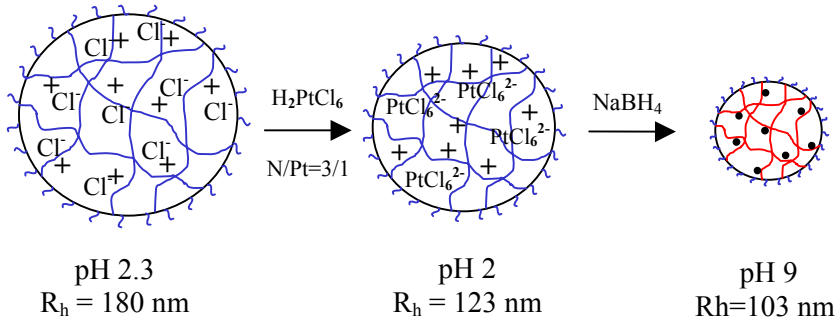

Figure 3.59 Schematic representation of metal nanoparticle formation within microgel particles at pH 2.

Figure 3.60 shows the intensity autocorrelation functions C(q,t) and the corresponding inverse laplace transformations at 60º scattering angle of a microgel solution at 0.05 wt% and pH = 2.3, the metallated microgel solution at 0.005 wt% and pH = 2 and the reduced sample at 0.001 wt% and pH = 9. From the distributions of relaxation times the respective hydrodynamic sizes were calculated.

During this metallation procedure we first obtained the swollen hydrophilic microgel particles at pH = 2.3, with a hydrodynamic radius of (180 ± 2) nm. Upon addition of H_2PtCl_6, the scattering intensity increases sharply while the calculated hydrodynamic radius decreases to (123 ± 2) nm due to the condensation of the protonated tertiary amine groups by the platinum anions as discussed above. We should note that the size obtained is similar to that found previously for the metallated

microgel using the first method of metal incorporation at high pH, suggesting that the metallated microgel characteristics are not influenced by the metallation procedure. After metal reduction the solution pH was raised to 9. A great increase of the scattered intensity is observed (high contrast) while the hydrodynamic radius of the metal nanoparticles containing microgel particles decreases to (103 ± 2) nm, since the DEAEMA units become deprotonated and thus hydrophobic, resulting in the formation of PDEAEMA latex particles.

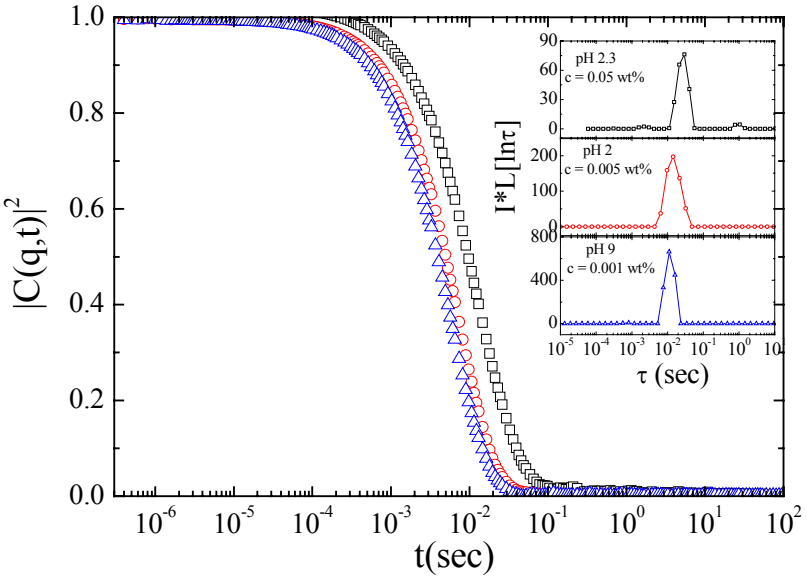

Figure 3.60 Intensity autocorrelation functions of a microgel solution at 30º scattering angle; at 0.05 wt% and pH = 2.3 (□), the metallated (H_2PtCl_6) microgel solution at 0.005 wt% and pH = 2 (○), the reduced sample at 0.001 wt% and pH = 9 (△). Inset: distribution of relaxation times multiplied by the total scattering intensity (normalized to that of toluene).

3.4.3 TEM images

The metallation process of the microgel particles and the metal nanoparticle formation was also verified by TEM studies. **Figure 3.61** shows the TEM images for the microgel particles upon addition of H_2PtCl_6 and after metal reduction for N/Pt =

1/1 molar ratio. The H_2PtCl_6 containing microgel particles are shown in **Figure 3.61a**, while **Figure 3.61b** shows the Pt nanoparticles formed after metal reduction. We should note that the Pt species incorporated inside the microgels provide the necessary contrast for TEM visualization of the particles. After reduction the contrast between the nanoparticles formed within the microgels and the polymeric material is so high that the microgels become invisible. From the images below the mean diameter of the metallated microgel particles before reduction was estimated around 80 nm while that of the platinum nanoparticles after metal reduction around 5 nm. These data are in quite good agreement with the size of the microgels platinic acid containing assessed by PCS earlier. The smaller sizes obtained from TEM than those found by PCS are attributed to the fact that PCS estimates a microgel size in solution while TEM deals with a dried sample. Besides the platinum species should be selectively located within the microgel and thus the diameter assessed by TEM represents the interior of the microgel particles rather than the overall microgel size.

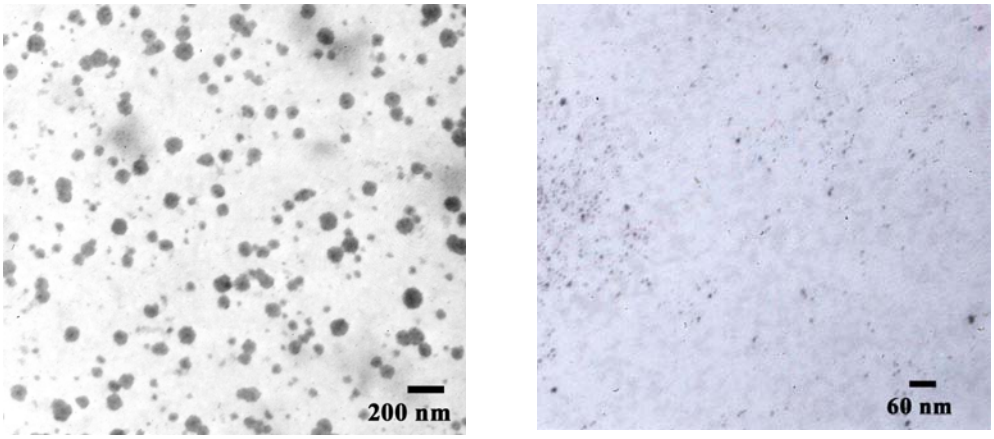

a) b)

Figure 3.61 TEM images of a) the PDEAEMA microgels after H_2PtCl_6 incorporation and b) the Pt nanoparticles after metal reduction at a N/Pt=1/1 molar ratio.

3.4.4 UV/Vis studies of metallation

UV/Vis spectroscopy has been used to study the polymer-metal interactions upon metallation of the microgel particles and after metal reduction. **Figure 3.62** shows the UV/Vis spectra for microgel solutions upon addition of H_2PtCl_6 at pH 2 and after metal reduction for N/Pt = 1/1 molar ratio. The spectra of the microgel particles in water at pH 2 and 10 and of H_2PtCl_6 in pure water are also shown for comparison. The microgel concentration in all samples was kept constant at 0.005 wt%. In consistency with the results obtained above for the metallated polymer micelles, in the presence of H_2PtCl_6 in the microgel solution a peak at 266 nm is observed in the spectrum. This peak which does not appear neither in the spectrum of the pure microgel nor in that of H_2PtCl_6 in pure water is characteristic of the electrostatic interactions between the $PtCl_6^{2-}$ anions and the protonated amine groups of the microgel as discussed above [6]. Furthermore, after reduction, the total disappearance of the peak at 266 nm confirms the complete metal reduction, resulting in the formation of the metal nanoparticles within the microgel particles as observed above by TEM.

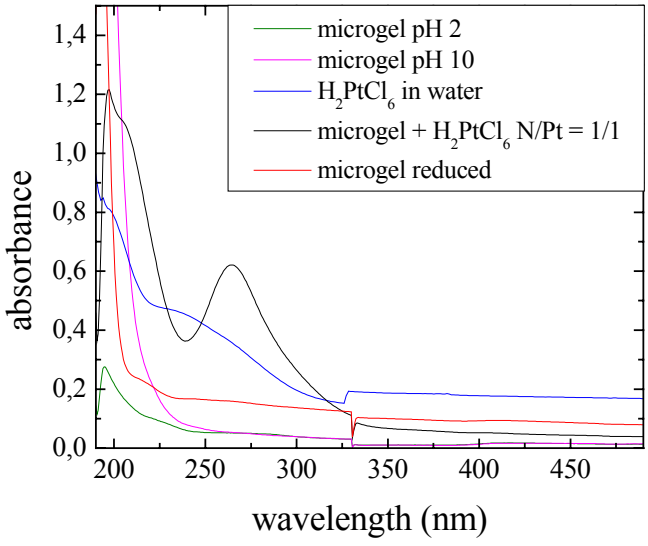

Figure 3.62 UV/Vis spectra of a microgel solution at pH 2 (—) and 10 (—), a solution of H_2PtCl_6 in pure water (—), a microgel solution in the presence of H_2PtCl_6 at a N/Pt = 1/1 molar ratio at pH 2 (—) and the reduced sample at pH 10 (—).

3.4.5 XRD studies of metallation

X-Ray diffraction measurements have been used to investigate the metal nanoparticle characteristics after metal reduction. **Figure 3.63** shows the XRD spectra for the pure microgel and the microgel in the presence of H_2PtCl_6 followed by metal reduction for a N/Pt = 1/1 molar ratio.

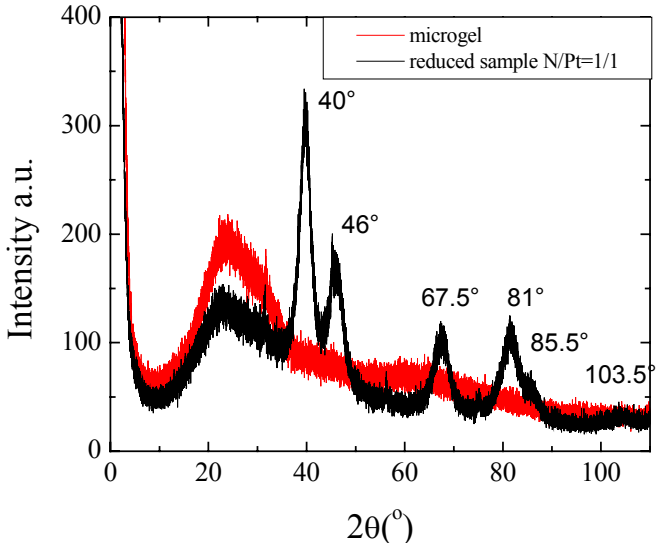

Figure 3.63 XRD spectra of the pure microgel (—) and the microgel in the presence of H_2PtCl_6 followed by metal reduction for a N/Pt = 1/1 (—).

The broad peak at ~25º is due to the polymeric material since it also appears in the pure microgel. The appearance of peaks in the reduced sample at 40º, 46º, 67.5º, 81º, 85.5º, 103.5º scattering angles are characteristic of the crystal structure of platinum, which confirms the crystallinity of the nanoparticles and the formation of metal nanocrystals within the microgel particles. From the FWHM of the peaks the size of the nanocrystals was calculated around 4.5 nm, which is in good agreement with the size estimated above for the same system by TEM and only slightly higher than that found within the cores of the block copolymer micelles (section 3.2.7). However, the metal nanoparticles containing microgel particles are expected to have improved catalytic properties as compared to their block copolymer micelle analogues due to the higher metal loading achieved in the former material. Thermogravimetric analysis (TGA) revealed at least 10% higher metal residue inside the microgel particles (38.8%) than that found within the polymer micelle structures (27.7%). Besides, the microgel matrices retain their colloidal stability over the whole pH range,

as verified above by DLS (sections 3.3.1, 3.4.2) in contrast with the block copolymer micelles which are formed in water only above pH 7, while they break apart for lower pH values after metal reduction, as found earlier by PCS (sections 3.2.2.1 and 3.2.2.3). The latter is particularly important for catalysis at low pH media, since it will influence both the particle surface modification and stability, and thus the catalytic performance of the materials.

3.5 References

[1] A. S. Lee, A. P. Gast, V. Bütün, S. P. Armes *Macromolecules*, 1999, **32**, 4302-4310.

[2] M. Vamvakaki, L. Papoutsakis, V. Katsamanis, T. Afchoudia, P. G. Fragouli, H. Iatrou, N. Hadjichristidis, S. P. Armes, S. Sidorov, D. Zhirov, V. Zhirov, M. Kostylev, L. Bronstein and S. H. Anastasiadis *Faraday Discuss.*, 2004, **128**.

[3] V. H. Katsamanis, *Master Thesis*, 2003.

[4] G. D. Poe, W. L. Jarrett, C. W. Scales, and C. L. McCormick *Macromolecules*, 2004, **37**, 2603-2612.

[5] B. D. Ermi, and E. J. Amis *Macromolecules*, 1996, **29**, 2701-2703.

[6] B. D. Ermi, and E. J. Amis *Macromolecules*, 1997, **30**, 6937-6942.

[7] B. D. Ermi, and E. J. Amis *Macromolecules*, 1998, **31**, 7378-7384.

[8] L. Bronstein, M. Vamvakaki, M. Kostylev, V. Katsamanis, B. Stein and S. H. Anastasiadis *Langmuir*, 2005, **21**, 9747-9755.

[9] L. M. Bronstein, S. N. Sidorov, A. Y. Gourkova, P. M. Valetsky, J. Hartmann, M. Breulmann, H. Cölfen, M. Antonietti *Inorg. Chim. Acta*, 1998, **280**, 348-354.

Chapter 4

Conclusions

The aqueous solution behavior of $PHEGMA_{50}$-*b*-$PDEAEMA_{50}$ diblock copolymer as a function of the degree of protonation (α) of the PDEAEMA block was investigated by DLS and ^1H NMR spectroscopy. It was found by DLS that the polymer is fully soluble and exists as unimers for degrees of protonation down to 30% while only for 20% protonated amines an increase in the number of aggregates is observed signifying the association of the polymer chains, prior to micelle formation. Micelles are first observed for degrees of protonation as low as 10% which reach their equilibrium size when the PDEAEMA units become fully deprotonated. These results are also in good agreement with the ^1H NMR data where a non-monotonous decrease in the fraction of soluble DEAEMA units is obtained for $\alpha = 0.2$ followed by a complete disappearance of the peaks corresponding to the protons of the PDEAEMA block for $\alpha = 0.0$ consistence with the formation of micelles with fully dehydrated cores. These results suggest clearly that the micellization process is not a gradual transformation that takes place over the whole deprotonation range but a rather sharp transition that occurs for lower than 20% protonated monomer units. This sharp unimer to micelle transition could be advantageous for certain applications such as the development of sensing elements of high selectivity.

Platinum nanoparticles were grown next within the cores of the micelles by incorporation of metal compounds (H_2PtCl_6, K_2PtCl_6) followed by metal reduction. Different synthetic procedures for the preparation of Pt nanoparticles inside the micellar cores were investigated.

Addition of the metal precursor in a molecular copolymer solution at low pH results in polymer-metal complexation and a metal-induced micellization process leading to the formation of stable equilibrium structures, as revealed by DLS. ^1H NMR studies also confirmed the metal-induced micellization process and further

verified the formation of compact non-hydrated cores resulting from the charge neutralization process. Metal reduction at low pH, carried out next, lead to the formation of metal nanoparticles and the partial decomposition of the metal-induced micelles, while the formation of only a few loose structures arising from possible weak interactions between the reduced metal and the polymer as observed. NMR studies also revealed the hydration of both polymer blocks indicating the decomposition of the micelles. Finally, DLS showed that upon increasing the solution pH, micelles containing the metal nanoparticles, are formed again due to the hydrophobicity of the DEAEMA units. On the other hand, increase of the pH with NaOH before metal reduction showed large fluctuations in the scattered intensity suggesting that metal-PHEGMA interactions take place in the solution outside the micelles and thus lead to the formation of nanoparticles in the exterior of the micellar core after metal reduction.

In the second method, addition of H_2PtCl_6 in a micellar copolymer solution at high pH leads to the partial decomposition of the micellar structures due to the protonation of the PDEAEMA block. However, the presence of the metal precursor in solution does not lead to a metal-induced micellization process similar to that described above at low pH, despite the protonation of the amine groups. Moreover, ^1H NMR studies showed that the PDEAEMA blocks remain non-hydrated upon addition of H_2PtCl_6 at high pH. It was shown that the presence of NaCl salt in the initial micellar solution is not responsible for this unexpected behavior. To elucidate these findings work is in progress to investigate the effect of the degree of protonation of the PDEAEMA block on the formation of the metal-induced micelles. Using the same Method, the incorporation of K_2PtCl_6 in a micellar copolymer solution was proven unsuccessful, suggesting that metal complexation via coordination of the amine groups to the metal precursor is not possible.

The metal-amine complexation and the metal-induced micellization for the first Method when the metal compound was added at low pH were also verified by UV/Vis by the appearance of a peak at 266 nm for the H_2PtCl_6 or K_2PtCl_6 containing polymer solutions. Additionally, UV/Vis studies showed that for N/Pt molar ratio greater than 2/1 very little further complexation occurs suggesting the saturation of the polymer with metal at this ratio. Finally, the total disappearance of the peak in the reduced sample suggests that metal reduction is quantitative. For the second method of metal incorporation in a micellar copolymer solution, the peak at 266 nm was not

observed indicating the absence of interactions between the polymer and the metal at high pH in consistency with our DLS studies.

The crystalline structure of the metal nanoparticles was confirmed by XRD studies which also allowed to estimate the size of the nanoparticles around 3.5 nm for two different loading ratios N/Pt = 3/1 and N/Pt =1/1. This size is in good agreement with that estimated from the TEM images of the reduced samples.

The aqueous solution properties of pH-responsive PDEAEMA-based microgel particles were investigated next. DLS measurements verified the reversible swelling-deswelling process upon adjustment of the solution pH from 180 nm at low pH to 110 nm for the hydrophobic latex particles at high pH.

Metal nanoparticles were formed within the microgel particles upon addition of H_2PtCl_6 followed by metal reduction with $NaBH_4$. Two methods were also used for the microgel metallation. In the first method, the metal precursor (H_2PtCl_6) was added in a solution of the latex microgel particles at high pH, while in the second method the platinic acid was added in a solution of the swollen microgel particles, at low pH. In both methods, DLS measurements revealed the electrostatic complexation between the polymeric material and the metal precursor observed as a slight increase of the size of the latex particles due to electrostatic repulsions, and a reduction of the size of the acid swollen microgels due to the formation of ionic cross-links. It is interesting to note that the sizes of the metallated microgels, using both methods of metal incorporation, were similar suggesting the formation of equilibrium metal-containing structures.

Similar to the results obtained for the metallated polymer micelles, a peak at 266 nm was observed in the UV/Vis spectrum of the microgel in the presence of H_2PtCl_6 at low pH, verifying the electrostatic interactions between the metal anions and the protonated amine groups of the microgel. Furthermore, the total disappearance of the peak after metal reduction confirms the complete metal reduction.

XRD studies confirmed the crystalline structure of the metal nanoparticles formed after metal reduction and allowed an estimation of their size around 4.5 nm, which is in good agreement with the size estimated for the same system by TEM. This size is only slightly higher than that found within the cores of the block copolymer micelles. On the other hand, higher metal loading was achieved for the microgel particles (solid residue = 28.8% by TGA) as compared to that of the polymer micellar

structures (solid residue = 27.7% by TGA). Besides, the microgel matrices retain their colloidal stability over the whole pH range in contrast with the block copolymer micelles which are only stable above pH 7. From the above discussion the microgel-based catalysts are expected to exhibit certain advantages in terms of their catalytic behavior as compared to the polymer micelle system, and work is underway to investigate this prospect.